



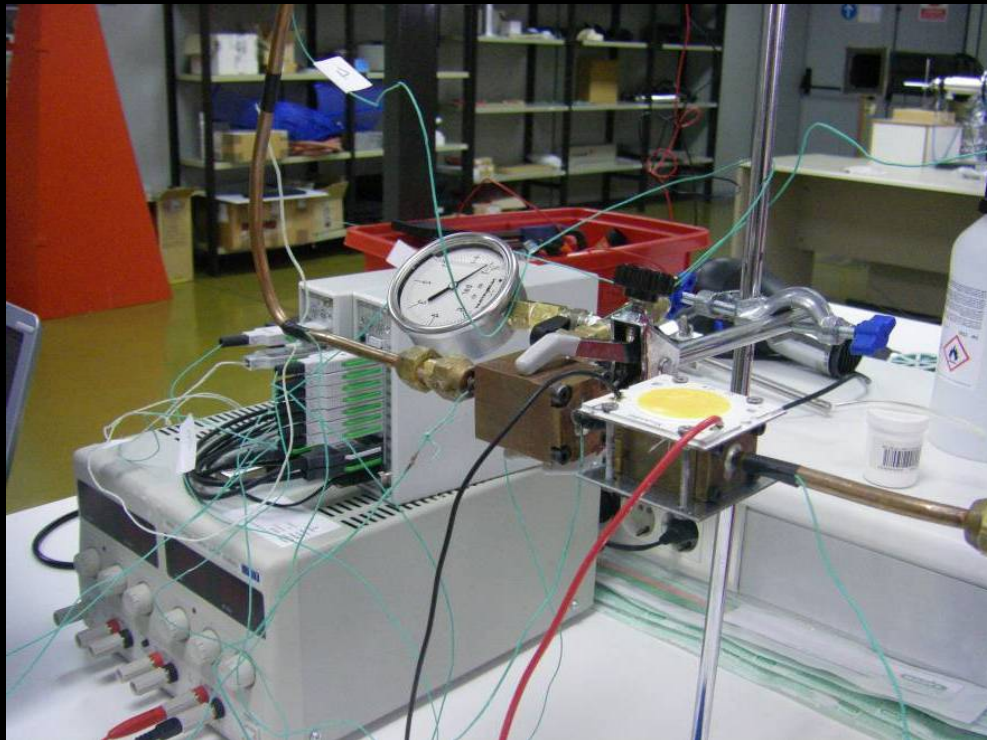
Universidad
del País Vasco

Euskal Herriko
Unibertsitatea



Ingeniaritza Goi Eskola Teknikoa
Escuela Técnica Superior de Ingeniería
Bilbao

DEVELOPMENT OF A LOOP HEAT PIPE "LHP" THERMAL SUPERCONDUCTOR DEVICE WITH MULTICONDENSORS



Author

Jesús Esarte San Martín

Supervisors

Jesús María Blanco Ilzarbe

José Tomás San José Lombera

July 2017, Bilbao

Thesis: Development of a Loop Heat Pipe "LHP"
thermal superconductor device with
multicondensers

UNIVERSIDAD PAIS VASCO
Dpto. INGENIERÍA MINERA Y METALÚRGICA
Y CIENCIA DE LOS MATERIALES



Universidad
del País Vasco

Euskal Herriko
Unibertsitatea



Ingeniaritza Goi Eskola Teknikoa
Escuela Técnica Superior de Ingeniería
Bilbao

DEVELOPMENT OF A LOOP HEAT PIPE "LHP" THERMAL SUPERCONDUCTOR DEVICE WITH MULTICONDENSORS

Author

Jesús Esarte San Martín

Supervisors

Jesús María Blanco Ilzarbe

José Tomás San José Lombera

July 2017, Bilbao



AREA CIENCIA DE MATERIALES
AREA MECANICA DE FLUIDOS
AREA CONSTRUCCION

ACKNOWLEDGEMENTS

Completing a PhD is truly a marathon event, and it would not have been accomplished without the aid and support of countless people over the last years. I must first express my gratitude towards my supervisor and director, Assistant professor Jesús María Blanco Ilzarbe for his patience and constant encouragement. It has not been an easy road and there have been many moments of difficulty that with the help of Jesus María have been overcome, so, many thanks. Thanks also to his constant technical guidance, without it this thesis had not been possible and concluded. After so long you have become a great friend and in the light that has guided me in this process. I would like also to thank to my co-director, Assistant professor José Tomás San José Lombera, for helping me with the same matters and also in all that arduous, ungrateful but necessary administrative work any thesis requires. You once told me that the day of the thesis defence is an enjoyment day and that the nerves of the occasion should be left out, the hard work was already done (execution of thesis). I thank you for such gratifying words, indeed this day should be a joy. Special gratitude to the Research group IT781-13 for assistance and co-funding some of the activities directly related to this work.

I'd also like to thank the members of the tribunal who have valued my work and attend to my defence.

My internship at NEDO Laboratory in Cardiff University during part of my PhD has been an invaluable experience, and I appreciate the help, support, and the enjoyable working environment my colleagues at NEDO have provided. I especially thank to the deceased Professor Mikel Rowe for making my stay there easier. I am also specially grateful to Professor Gao Min for introducing me into the Thermoelectrics field and sharing all his knowledge on thermoelectric materials characterization, fabrication and assembly. After all, it has been the trigger for this thesis.

I would like also to thank all my lab mates and friends at CEMITEC for their friendship and moral support in such stressful times. I want to give a special mention to my colleague Angela Bernardini for her contributions to my research during my PhD years. Her ability to probe physics beneath the math is a true talent drives me through the complexity of the fluid mechanics in porous media.

Finally, I want to thank my family for their continued understanding and support during these years of stress and absence from home. Especial grateful is given to my wife, Neli Waltl, for his love and companionship, and for her patience and for giving me two marvellous sons, Alejandro and David. To my parents and brothers, for all the effort they have done so that I have been able to do my university career, always grateful.

AGRADECIMIENTOS

La realización de una tesis es un ejercicio realmente maratónico y no habría sido posible sin la ayuda y el apoyo de una infinidad de personas durante estos últimos años. Quiero expresar primeramente mi gratitud a mi asesor y director, el profesor Jesús María Blanco Ilzarbe, por su paciencia y constante ánimo durante todo este proceso. No ha sido un camino fácil y ha habido muchos momentos difíciles, de altibajos los cuales han sido superados gracias al apoyo y aliento de Jesús María, así pues muchas gracias. Igualmente, agradecer su constante apoyo y orientación técnica sin ella la cual esta tesis no habría sido posible. Después de todo este tiempo te has convertido en un gran amigo y en la luz que me ha guiado durante todo el proceso de ejecución-redacción de la tesis. Así mismo doy las gracias a mi codirector, el profesor José Tomás San José Lombera, por ayudarme en los mismos términos y en todo ese arduo, ingrato pero necesario trabajo administrativo que cualquier tesis requiere. Una vez me dijiste que el día de la defensa de la tesis es un día para disfrute y que los nervios de la ocasión deben ser dejados de lado, lo difícil ya estaba hecho (ejecución de tesis). Te doy las gracias por tan gratificantes palabras, en verdad este día debe ser de júbilo. Especial agradecimiento al grupo de investigación IT781-13 por su ayuda y co-financiación de algunas de las actividades directamente relacionadas con este trabajo.

También quisiera dar las gracias a los miembros del tribunal que han valorado mi trabajo y han asistido a mi defensa.

Mi estancia en el Laboratorio NEDO de la Universidad de Cardiff durante una parte de mi doctorado ha sido una experiencia inestimable y agradezco la ayuda, el apoyo y el agradable ambiente de trabajo que mis colegas de NEDO me han proporcionado. Agradezco especialmente al fallecido profesor Mikel Rowe por hacer que mi estancia

fuera más fácil. También estoy especialmente agradecido al profesor Gao Min por haberme introducido en el campo de la termoeléctricidad y por compartir todo su conocimiento en el campo de la caracterización, fabricación y montaje de los materiales termoeléctricos. Después de todo, ha sido el desencadenante de esta tesis.

También quiero agradecer a todos mis compañeros y amigos de CEMITEC por su amistad y apoyo moral en tiempos tan agobiantes. Quiero hacer mención especial a mi compañera Angela Bernardini por sus contribuciones a mi investigación durante mis años de doctorado. Su visión de la física a través de la matemática es un talento que me ha guiado a través de la complejidad de la mecánica de fluidos en medios porosos.

Finalmente, quiero dar las gracias a mi familia por su comprensión y apoyo continuo durante estos años de estrés y ausencia. Doy las gracias especialmente a mi esposa, Neli Walth, por su amor y compañerismo, por su paciencia y por darme dos hijos maravillosos, Alejandro y David. A mis padres y hermanos, por todo el esfuerzo que han hecho para que yo haya podido realizar mi carrera universitaria, siempre agradecida.

Thesis: Development of a Loop Heat Pipe “LHP”
thermal superconductor device with
multicondensers

UNIVERSIDAD PAIS VASCO
Dpto. INGENIERÍA MINERA Y METALÚRGICA
Y CIENCIA DE LOS MATERIALES

Summary

Overheating is a critical factor in the functionality of many high power density electronic devices (microprocessors, telecommunications, solar cells, wind power, photovoltaic, electric traction systems, thermoelectric devices, etc.). The reliability, lifetime and efficiency of these devices are severely limited by the speed at which the heat generated during their operation is dissipated.

The electronic world nowadays evolves towards smaller devices and components with greater operating capacity and consequently with greater generation of heat (density of heat flow). This increase in heat flow together with the component miniaturization result in a cooling needs increase and therefore the power consumption associated therewith. As an illustrative example of the weight of refrigeration's power consumption on total power consumption, the study by EMERSON network power is shown, figure 1.

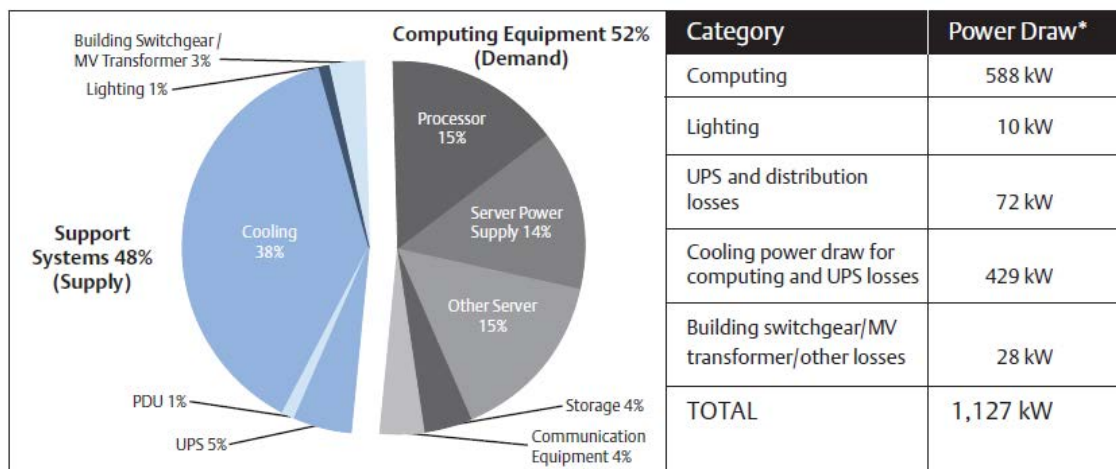


Figure 1. Analysis of a typical 5,000-square-foot data center shows that demand-side computing equipment accounts for 52 percent of energy usage and supply-side systems account for 48 percent.

* This represents the average power draw (kW). Daily energy consumption (kWh) can be captured by multiplying the power draw by 24.

The study shows that 38% of the total power consumption of a 450 m² data centre is due to the cooling system. It seems obvious the need to improve cooling systems efficiency and / or reduce data centre power consumption, cascade effect. Effect due to which, a 1W power consumption reduction of a server leads to a 2.84W reduction of the data centre, figure 2.

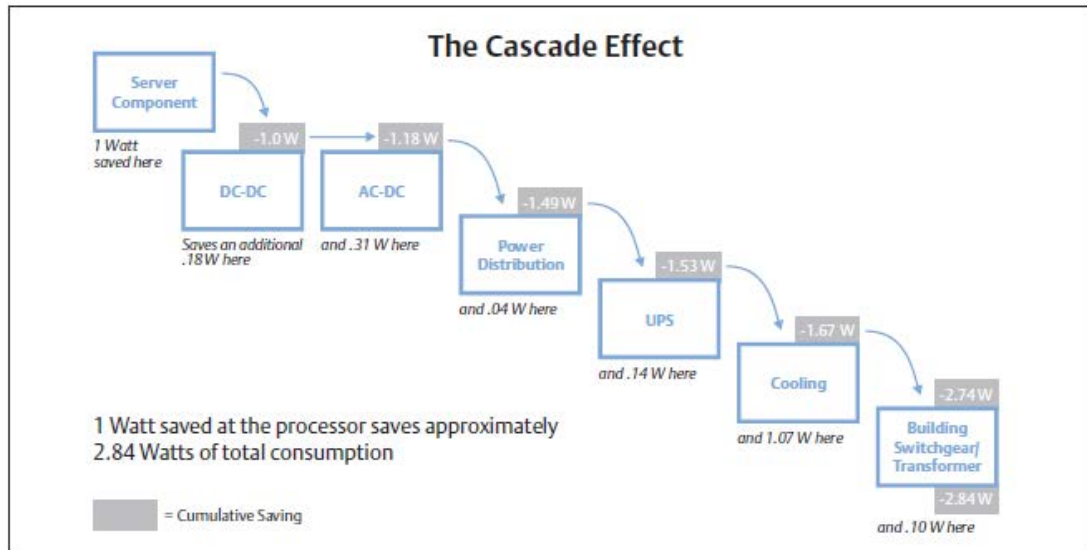


Figure 2. With the Cascade Effect, a 1-Watt savings at the server-component level creates a reduction in facility energy consumption of approximately 2.84 Watts.

However, reducing the component's consumption by 1W means reducing its operating temperature, ie increasing its refrigeration.

As for the Peltier thermoelectric devices, the fact of having an efficient heat extraction from both hot and cold sides directly influences the efficiency of the Peltier (cooling capacity or energy conversion capacity), figure 3.

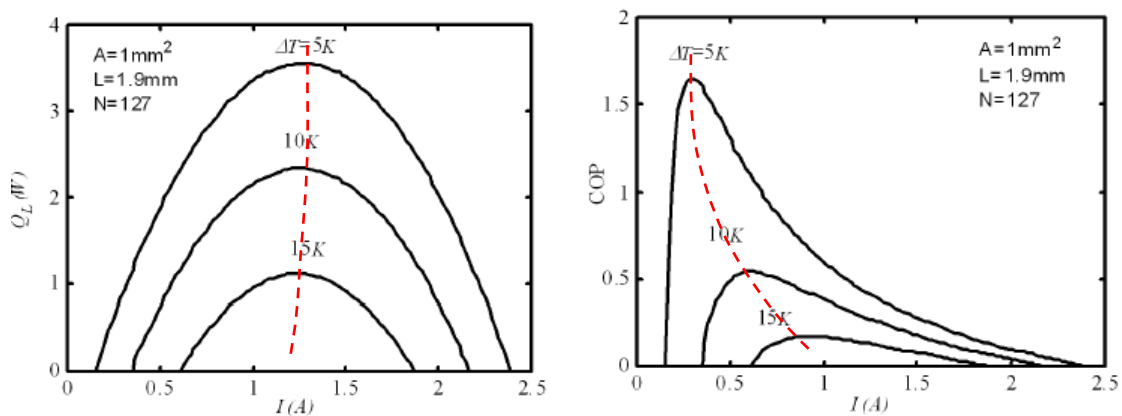


Figure 3: Evolution of the cooling capacity and efficiency as a function of the temperature rise

As the temperature difference between the hot and cold side of the Peltier increases, " ΔT ", the maximum cooling capacity " $Q_{L_{\max}}$ " decreases and so does its COP (Coefficient of operation) " COP_{\max} ". This temperature rise " ΔT " is greater as greater the thermal resistance or efficiency of the heat extraction device placed on both sides of the Peltier (discussed in this thesis) is. It is therefore essential to improve the efficiency

of these cooling systems (heatsinks) in order to obtain the maximum of Peltier systems (either as a refrigerator or as a converter).

The above examples and many others in industrial refrigeration highlight the importance of efficient refrigeration technologies. However, as far as the world of electronics is concerned, there is a fundamental aspect when looking for efficiency in refrigeration and it is the high heat densities that occur in it. These high heat densities mean that traditional cooling systems (fin radiators) are not efficient. In this work, a rapid analysis of the influence of the radiator parameters on its thermal resistance is made.

The increase in the efficiency of refrigeration happens to extract more heat under the same temperature jump without that implies devices of great volume (not admitted in the electronic world). High heat extraction technologies with similar or slightly higher sizes than those of heat sources (electronic component, Peltier) are sought. In addition, they must ensure the minimum temperature difference between the hot spot (heat extraction) and the cold point (heat expulsion), devices such as the heat pipe "LHP". This work focuses on this type of device: performance, key parts and their improvement.

For this, a numerical model able to predict the LHP operation as a function of constructive parameters and dissipation needs has been developed. Likewise, the construction and testing of such a device have been carried out for the cooling of a 4cmx4cm surface device generating about 50W heat power.

Also, an analysis of the primary and secondary wick's behaviour and the importance of obtaining a very high capillary pumping is made. There are different technologies for the manufacture of these wicks, although the 3D Printing "SLM" technology has been used. This technology allows to create wicks with a customized internal structure and adapted to the thermal requirements, innovative part of the work.

Resumen.

El sobrecalentamiento es un factor crítico en la funcionalidad de muchos dispositivos electrónicos de alta densidad de potencia (microprocesadores, telecomunicaciones, celdas solares, inversores eólicos, fotovoltaica, sistemas de tracción eléctrica, dispositivos termoeléctricos, etc...). La fiabilidad, vida útil y eficiencia de estos dispositivos están fuertemente limitadas por la velocidad a la que es disipado el calor que generan durante su funcionamiento.

El mundo electrónico hoy día evoluciona hacia dispositivos, componentes, más pequeños con mayor capacidad de operación y en consecuencia con mayor generación de calor (densidad de flujo de calor). Este incremento de flujo de calor unido a lo reducido del tamaño de los focos generadores hace que se incrementen las necesidades de refrigeración y por tanto los consumos ligados a ello. A modo de ejemplo ilustrativo del peso que la refrigeración tiene sobre el consumo total de operación, se muestra el estudio realizado por la empresa EMERSON network power, **figura 1**.

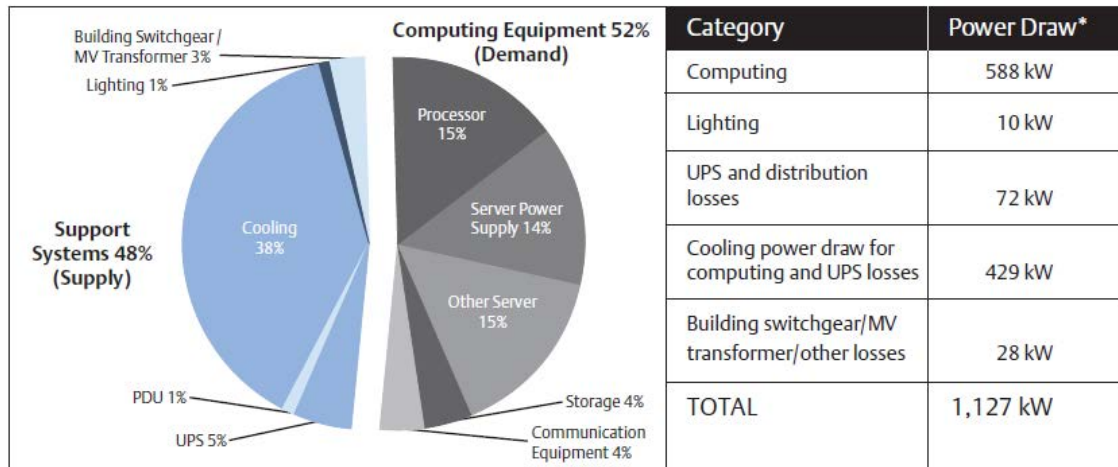


Figure 1. Analysis of a typical 5,000-square-foot data center shows that demand-side computing equipment accounts for 52 percent of energy usage and supply-side systems account for 48 percent.

* This represents the average power draw (kW). Daily energy consumption (kWh) can be captured by multiplying the power draw by 24.

Del estudio realizado se comprueba que el 38% del consumo total de un centro de cálculo de 450 m², es debido al sistema de refrigeración. Parece evidente la necesidad de mejorar la eficiencia en los sistemas de refrigeración y/o reducir los consumos del data center, **efecto cascada**. Efecto debido al cual, la reducción en 1W del consumo de un componente del servidor conduce a una reducción 2.84W en el consumo del centro de cálculo, figura 2.

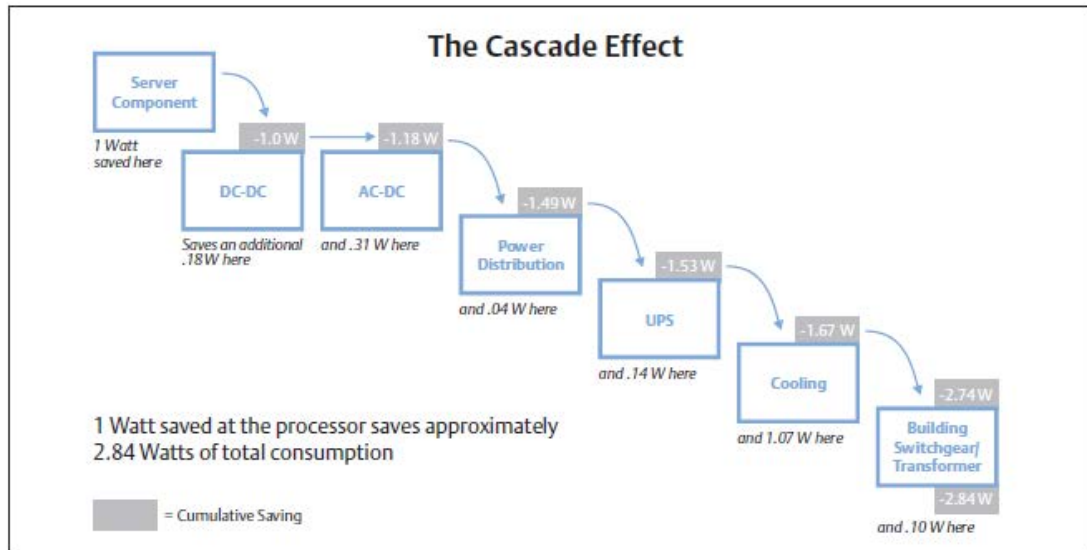


Figure 2. With the Cascade Effect, a 1-Watt savings at the server-component level creates a reduction in facility energy consumption of approximately 2.84 Watts.

Ahora bien, reducir 1W el consumo de un componente pasa por reducir su temperatura de operación, es decir, incrementar su refrigeración.

En cuanto a los dispositivos termoelectricos-Peltier el hecho de contar con una extracción de calor eficiente de sus focos tanto caliente como frío influye directamente en la eficiencia del Peltier (capacidad de refrigeración o de conversión de energía), **figura3**

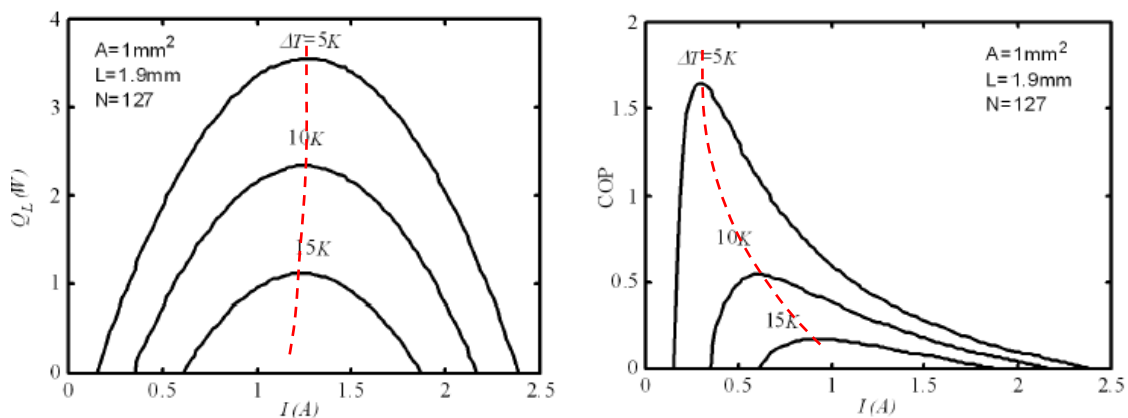


Figura 3: evolución de la capacidad frigorífica y eficiencia en función del salto de temperatura

A medida que la diferencia de temperatura entre lado caliente y frío del Peltier, “ ΔT ” aumenta, la capacidad máxima de refrigeración “ Q_{Lmax} ” disminuye y lo mismo ocurre con su COP (coeficiente de operación) “ COP_{max} ”. Este salto de temperatura “ ΔT ”, es mayor cuanto mayor la resistencia térmica o eficiencia del dispositivo de extracción de

calor colocado en ambas caras del Peltier (se analiza en esa tesis). Por consiguiente, es fundamental el mejorar la eficiencia de estos sistemas de refrigeración (disipadores) a fin de obtener el máximo de los sistemas Peltier (bien como refrigerador bien como conversor).

Los ejemplos anteriores y otros muchos dentro de la refrigeración industrial resaltan la importancia de contar con tecnologías de refrigeración eficientes. Sin embargo, en lo que al mundo de la electrónica, Pelteir se refiere, existe un aspecto fundamental a la hora de buscar la eficiencia en la refrigeración y es las elevadas densidades de calor que en él se producen. Estas altas densidades de calor obligan a que los sistemas tradicionales de refrigeración (radiadores de aletas) no sean lo todo eficientes que pueden ser. En este trabajo se hace un rápido análisis de la influencia de la configuración-diseño de un radiador sobre su resistencia térmica.

El incremento en la eficiencia de refrigeración pasa por extraer de forma eficiente las elevadas densidades de calor sin que ello implique dispositivos de gran volumen (no admitido en el mundo electrónico). Se buscan tecnologías de alta capacidad de extracción de calor con tamaños similares o ligeramente superiores a los de las fuentes de calor (componente electrónico, Peltier) y que supongan una mínima diferencia de temperatura entre el punto de extracción de calor y el punto expulsión del mismo. Dispositivos como los loop heat pipe “LHP”. Este trabajo se centra en este tipo de dispositivo: performance, partes clave y su mejora.

Para ello se ha desarrollado un modelo numérico capaz de reproducir el funcionamiento del dispositivo en función de parámetros constructivos y de necesidades de disipación. Así mismo se ha llevado a cabo la construcción y ensayo de tal dispositivo para la refrigeración de un dispositivo de 4x4cm y unos 50W de potencia térmica.

Así mismo se hace un análisis del comportamiento de los “wick” tanto primario como secundario de estos dispositivos y la importancia de la obtención de obtener una muy alta capilaridad. Existen diferentes tecnologías para la fabricación de estos wicks, si bien en este dispositivo se ha empleado el láser printing technology que permite crear los wicks con la estructura interna personalizada y adaptada a los requerimientos térmicos, parte innovadora del trabajo.

DEVELOPMENT OF A LOOP HEAT PIPE “LHP” THERMAL SUPERCONDUCTOR DEVICE WITH MULTICONDENSERS

Acknowledgments	iii
Summary	vii
Table of Contents	xiv
Chapter 1.- Thermal management in electronic component. Thermal challenges in Peltier module and LED	
1.1- Introduction.....	2
1.2- Thermal challenges in Peltier pellets-LED.....	4
1.2.1- Peltier pellet.	4
Operating principle	4
Peltier pellet arrangement	5
Parameters influencing the performance of a Peltier pellet.....	6
1.2.2 Light emitting diode (LED).	10
Operating principle	10
LED Lamp Configuration.....	11
LED performance influent parameters.	11
1.3- Motivation.....	13
Bibliography.....	16
Chapter 2.- Objectives and methodology	
2.1- Objectives.	19
2.2- Thermal management challenges.....	19

2.2.1- Effect of the heat flow direction	20
2.2.2- Heatsink efficiency	22
2.3- Methodology and Contributions	33
Bibliography	33
Chapter 3.- Capillarity in porous media	
3.1 Introduction	37
3.2 Fluid-dynamic in a porous medium	39
3.2.1- Macroscopic mathematical approach.	40
3.2.2- Wick loading curve.....	44
3.2.3-Permeability	47
3.3. Experimental characterization.....	51
3.3.1- Loading curve	51
3.3.2- Permeability	59
Bibliography	65
Chapter 4.- Development of a theoretical model of two-phase heatsink Loop Heat Pipe	
4.1 Introduction	69
4.2 Model's Development.....	70
4.2.1- Brief description of the components:.....	72
4.2.2- Mathematical formulation	72
4.3 Results	84
4.3.1- Validation.....	84

4.3.2- Effect of vapour line length and radius.	88
4.3.3- Effect of condensing temperature.....	89
4.4 Conclusions	93
Bibliography.....	95
 Chapter 5.- Manufacturing and experimental testing of the LHP	
5.1 Introduction	99
5.2 Primary Wick	99
5.2.1-Permeability, “K”	101
5.2.2- Wettability- Capillary Pumping, “ φ ”	102
5.2.3-Thermal conductivity “K”	105
5.3. Secondary Wick	106
5.3.1-Transport capacity “TC”	107
5.4. LHP-Results	110
5.4.1- Starting up.....	112
5.4.2- Charge of refrigerant.....	114
5.4.3- Condensation/ambient temperature.	116
5.5. Conclusions	119
Bibliography.....	121
 Chapter 6.- Conclusion and Future works	
6.1-Conclusions.....	124
6.2-Future works	127

ANNEXES

1-Nomenclature	129
2-List of figures	132
3-List of tables	142
4-Refrigerant properties	144
5-Previous works	151
Porous media	152
HP prototypes	157
6-Brief CV of the author	162

Thesis: Development of a Loop Heat Pipe “LHP”
thermal superconductor device with
multicondensers

UNIVERSIDAD PAIS VASCO
Dpto. INGENIERÍA MINERA Y METALÚRGICA
Y CIENCIA DE LOS MATERIALES

Chapter 1 Thermal management in electronic component. Thermal challenges in Peltier module and LED.

1.1- Introduction.....	2
1.2- Thermal challenges in Peltier pllets-LED.....	4
1.2.1- Peltier pellet.....	4
Operating principle	4
Peltier pellet arrangement	5
Parameters influencing the performance of a Peltier pellet.....	6
1.2.2 Light emitting diode (LED).....	10
Operating principle	10
LED Lamp Configuration.....	11
LED performance influent parameters.	11
1.3- Motivation.....	13
Bibliography.....	16

1.1- Introduction

Since the 1970s the semiconductor industry (electronics) has been driven by the so-called Moore's Law. Law, established in 1965 by George Moore, in which it was affirmed that the number of components that could be integrated in a printed circuit would grow exponentially in the time, which implied a manufacturing cost reduction (cost per unit) and allowed the manufacture of more complex circuits in a single semiconductor. Since 1970 the number of components per chip has been doubling every two years, Moore's law. For decades, this law has been the driving force of the semiconductor industry in particular and electronics in general thanks to the so-called virtuous cycle, **figure 1.1**. A cycle in which advances in integration (cost reduction, greater functionality) boost the semiconductor market and investments in new technologies that in turn increase integration and reduce costs [1].

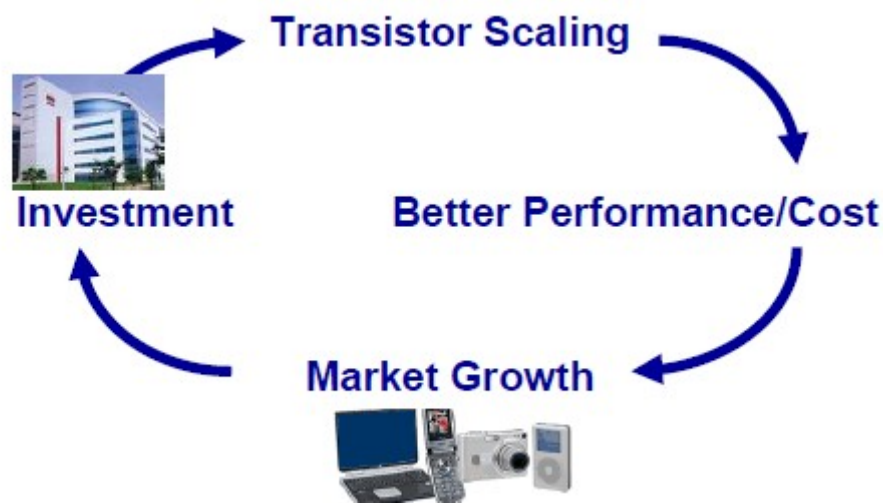


Figure 1.1 Moore law

However, this continuous advancement has led to the so-called "*More than Moore*" technology which targets not only the transistor integration density increase (miniaturization-digital) but also the diversification of functions (non-digital) in the component.

This heterogeneous integration of digital and non-digital functions into electronic components is the current engine in many electronic applications. This new trend establishes a new virtuous cycle, **figure 1.2**.



Figure 1.2: "More than Moore" law.

These "More tan Moore" and / or "More Moore" technologies have been boosted by the development of the semiconductor world. Although the trend in electronics is to increase: integration level, operating temperature, reliability, functionality and reduce size, weight and manufacturing cost, the barrier in its evolution is its **thermal management** [2]. In order for the predictions of "More Moore" or "More than Moore" to be met, it is essential to address the issue of efficient extraction of this high heat density in new packages. In this regard, technologies such as liquid and two-phase cooling (boiling flow) have been considered. Nevertheless, although they have got high cooling capacity, both require of refrigerant pumping systems that makes them more complex and risky. On the other hand, there is the air cooling technology, with advantages such as zero risk and simplicity but with the disadvantage of its low cooling capacity compared to the previous two, which leads to large volume equipment. In order to improve this limitation of air cooling, passive refrigeration systems with phase change, "heat pipes". Back in 1839, Angier March patented a sealed tube where a fluid boiled. Subsequently, Jacob Perkins patented the so-called Perkins tube in 1936 in which water experienced an evaporating-condensing process being the condensate returned back to the evaporator by gravity. As early as 1960 heat pipe technology evolved into different shapes and sizes being applied in many sectors from PCs to telecommunications.

Peltier modules and LEDs are also subjected to all the barriers and trends discussed above.

1.2- Thermal challenges in Peltier pellets-LED

In these two components, as in all other electronic components, the efficient management of the heat generated by them is the main barrier that limits their functionality and probably prevents their cost reduction.

1.2.1- Peltier pellet.

The basic concepts of thermoelectricity have already been described in a multitude of books and articles [3-7], so here is a brief description as a reminder to those who know the subject and as an introduction to a better understanding for those who are initiated in the matter.

Operating principle

It is based on a physical phenomenon whereby the union of two different conductors generates an electromotive force as a consequence of the external application of a thermal flow "**Seebeck effect**" or vice versa, when circulating an electric current through the union, a temperature decrease or increase (depending on the current direction) is obtained in the junction, "**Peltier effect**".

This is more clearly understood by the following example:

- 1)-be a circuit constituted by two separate conductors "a and b" connected by one of its ends and open by the other, **figure 1.3**.

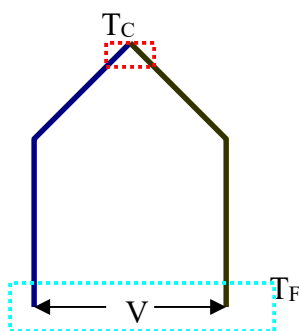


Figure 1.3: Seebeck effect

If the junctions of these two conductors, electrically connected in series and thermally in parallel, are maintained at different temperatures " T_C , T_F ", where $T_C > T_F$, a voltage " $V = \alpha_{ab}(T_C - T_F)$ " appears at the open end "**Seebeck effect**", where " α_{ab} " is the Seebeck coefficient.

2)- be a closed circuit constituted by two separate conductors "a and b" through which an electric current, "I", is flowing, **figure 1.4**.

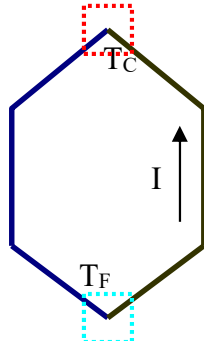


Figure 1.4: Peltier effect

When passing an electric current through the closed circuit, a heat rejection "T_C" and a heat absorption ("T_F < T_C") occurs in the junctions, "**Peltier effect**" ($Q_p = \pi_{ab} I$). Being " π_{ab} " the Peltier coefficient.

As mentioned previously, these phenomena are due to the matter behaviour when subjected to external excitations (thermal field, electric field) and they have to do with the **bands theory** by which materials are classified into: *conductors, insulators and semiconductors*

Peltier pellet arrangement

So far thermoelectric phenomena have been briefly discussed, and how these occur in conductor unions. However, these terms have no practical application to the exception of temperature measurement. In case you want to use them as a thermoelectric cooling system it is necessary to use a multitude of these thermocouples to achieve a reasonable cooling power " \dot{Q} " ($\dot{Q} = \sum_1^n \dot{Q}_p$), where

" \dot{Q}_p " heat generated in a joint (very small value) and "n" the number of joints thermally in series. At this point, one can already intuit that the refrigerating power of these systems is in the range of low powers and therefore their applications are quite restricted..

According to the foregoing, a thermoelectric pellet (minimum unit capable of providing a considerable effect) is merely a series of thermocouples electrically connected in series and thermally in parallel. This results in a heat

absorption/rejection from/to the environment equivalent to the sum of the heat generated by each thermocouple when an electric current "I" flows through them.

Figure 1.5 shows the arrangement of the thermocouples in a pellet.

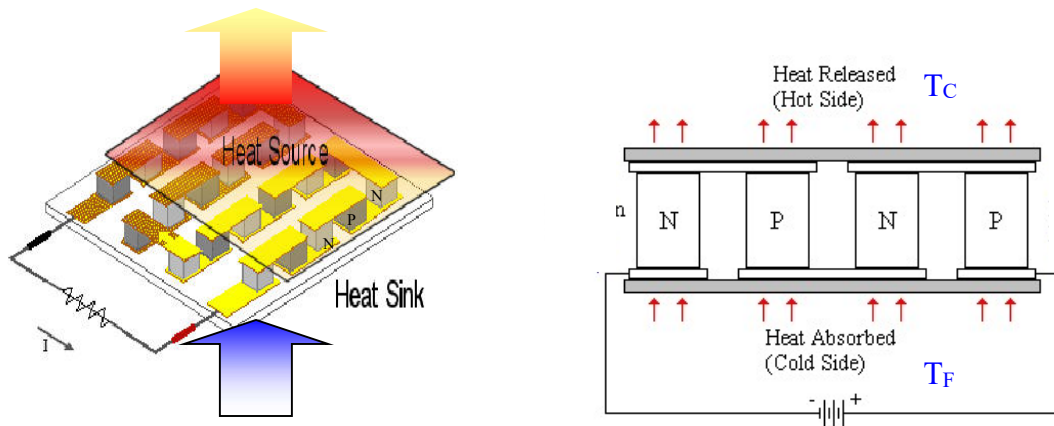


Figure 1.5: Arrangement of semiconductors junctions type "p-n".

As shown in figure 1.5, all "np" type joints are in the upper part (**cold side**) and the "pn" type joints are in the lower part (**hot side**), ie they are arranged thermally in parallel. In addition, ceramic plates are placed at the top and bottom to electrically but no thermally isolate the pellet from the surroundings.

Parameters influencing the performance of a Peltier pellet.

Currently, due to environmental pollution and global warming, there is a tremendous concern about: energy efficiency, energy recovery and progressive reduction of CFCs (FGas regulations set deadlines for the use of these CFCs refrigerants by to sector) among others. According to this, thermoelectricity presents a great environmental advantage, what is of great interest in both refrigeration and energy conversion (thermal to electrical). However, its efficiency and COP [8] are not the best, depending on:

- Thermoelectric properties of semiconductors (materials science)
- Design, configuration of thermoelectric module "TE" (length and cross section of thermoelement, contacts and materials).
- Hot and cold temperature (very much influenced by the heat sink design).

$$COP = \frac{l}{l + 2rl_c} \left(\frac{T_F}{T_C - T_F} \frac{\beta - \frac{T_C}{T_F}}{1 + \beta} - \frac{rl_c}{l} \right) \quad (1.1)$$

where

$$\beta = \sqrt{1 + \frac{lz\bar{T}}{n+l}}, \quad \text{“}l\text{” thermoelement length.}$$

$$r = \frac{\lambda}{\lambda_c}, \quad \text{ratio between the thermoelement thermal conductivity “}\lambda\text{”}$$

and that of the contact “}\lambda_c\text{”.

$$n = 2 \frac{\rho_c}{\rho}, \quad \text{ratio between the electrical resistivity of the contact “}\rho_c\text{”}$$

and that of the thermoelement “}\rho\text{”.

l_c is the thickness of metal contact plus the ceramic layer..

$$\text{“}Z = \frac{\alpha_{AB}^2}{\rho\lambda}\text{” thermoelectric pellet **figure of merit**, } \alpha_{AB}, \text{ is the Seebeck}$$

coefficient and “}\bar{T} = \frac{T_C + T_F}{2}\text{” being “}T_C\text{” y “}T_F\text{” the hot and cold

temperatures of the Peltier pellet.

As a refrigerator, the effect of Peltier pellet faces' temperature “}\Delta T = T_C - T_F\text{” on both the COP and cooling capacity “}Q_F\text{” is shown in **figure 1.6**.

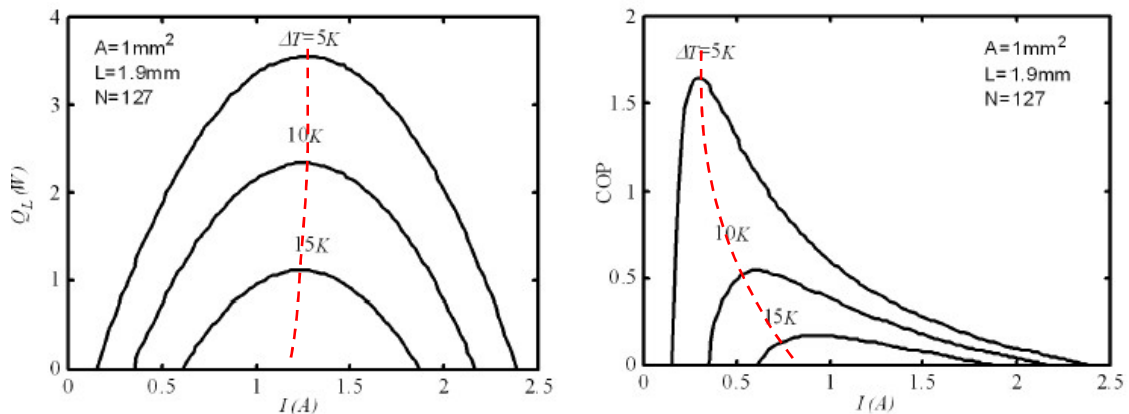


Figure 1.6: Effect of ΔT on both COP and cooling capacity of a thermoelectric pellet

In case of working as a converter, conversion power given by (1.2), the effect of ΔT on the converted power is shown in **figure 1.7**.

$$P_{opt} = (\alpha_{AB} \Delta T)^2 \frac{\sqrt{1 + ZT}}{(1 + \sqrt{1 + ZT})^2 R} \quad (1.2)$$

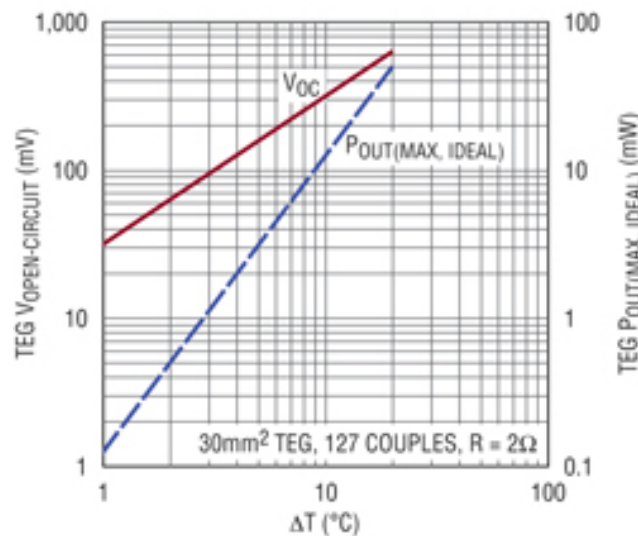


Figure 1.7: Open circuit voltage and maximum power for a typical TEG

In view of Figures 6 and 7, it is observed that it is interesting to reduce the ΔT when working as refrigerator and to increase as converter, that is to say, temperature on the faces should be closest to the sinks' temperature with which the pellet exchanges heat. For this, it is necessary that the **heat sinks** have the least possible **thermal resistance** (efficient heat exchanger). Considering this heat sink, equation 1.1 becomes 1.3.

$$COP = \frac{l}{l + 2rl_C} \left(\frac{T_{int} - \Delta T_{int}}{\Delta T_{amb} + \Delta T_{int} + T_{amb} - T_{int}} \frac{\beta^* - \frac{\Delta T_{amb} + T_{amb}}{T_{int} - \Delta T_{int}}}{1 + \beta^*} - \frac{rl_C}{l} \right) \quad (1.3)$$

where $\beta^* = \sqrt{1 + \frac{lz\bar{T}}{n+l}}$ y $\bar{T} = \frac{\Delta T_{amb} + T_{amb} + T_{int} - \Delta T_{int}}{2}$

Expression that for the particular case of table 1.1 and different design temperatures, assuming the same temperature drop on both dissipaters, results, **figure 1.8**:

Table 1.1: Physical properties of a commercial Peltier pellet

l (mm)	lc (mm)	n	z (K ⁻¹)	r
1	0.7	0.1	2.8e-3	0.05

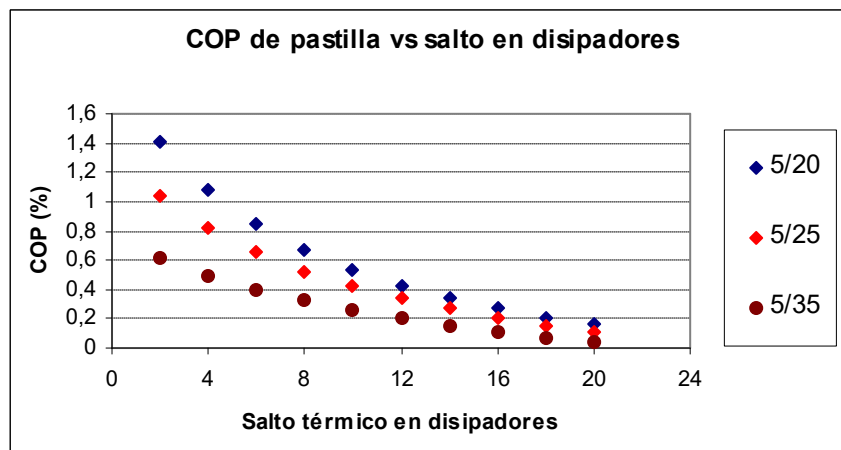


Figure 1.8: Peltier pellet COP as a function of temperature difference between hot and cold heat dissipaters.

A lot of work has been done about the thermal behavior of a Peltier pellet in order to better understand the heat flux within the device and to be able to establish with greater precision the influence of the temperature drop in both the COP and conversion capacity. One of these works exclusively studies the pellet [9] using conventional tools, while others carry out a study of the complete thermoelectric pellet [10-12], developing a specific tool tested in different applications [13-16]. There

are also works that show the importance of heat sink design of on the Peltier pellet performance [17-19].

1.2.2 Light emitting diode (LED).

Thermal management in the LED devices is a key issue since light quality and quantity and LED device's reliability and life depend on it. LED devices require, on one hand, a high electric current to obtain the maximum of lumens and on the other hand, an electric current as low as possible to reduce the generation of heat. In every LED lighting device, the most expensive part is the LED itself, so reducing the number of LEDs, providing the same amount of light, would reduce costs. The latter involves increasing the electric current, but, as discussed above, this generates more heat flow and therefore an increase in temperature (there is a maximum value depending on the materials used). Thus, increasing the electric current should come accompanied with an efficient refrigeration system to keep LED temperature lower than its maximum value.

Operating principle

Like thermoelectric element, a light-emitting diode is a union of two types of semiconductors "p and n type" which produces a circulation of electron through the union when a "V" voltage is applied. This electron flow generates an energy in the form of photons (band gap). This energy determines the color of the light, **figure 1.9.**

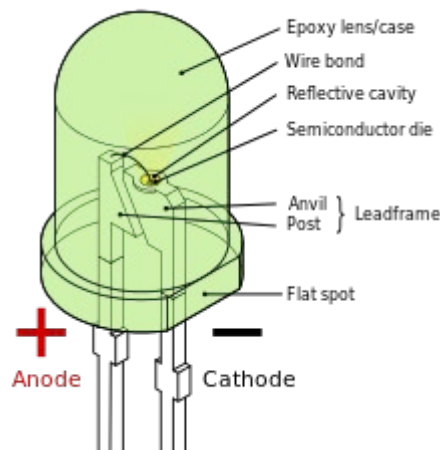


Figure 1.9: LED sketch

LED Lamp Configuration

In order to increase the amount of light, LEDs are arranged in matrix and / or multichannel mode on an electronic board, **figure 1.10**.

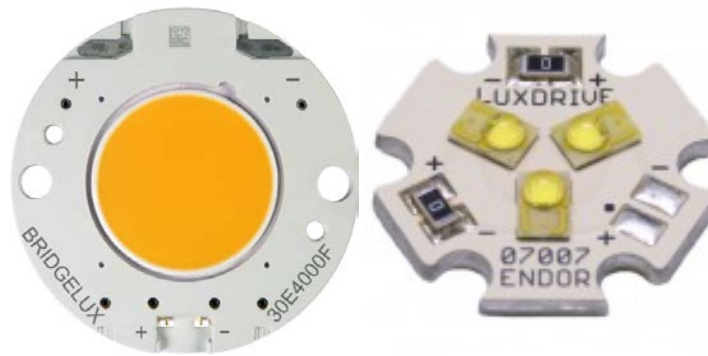


Figure 1.10: Example of LED integration

LED performance influent parameters.

LED temperature directly affects to light quantity, quality and colour as well as LED device's efficiency [20].

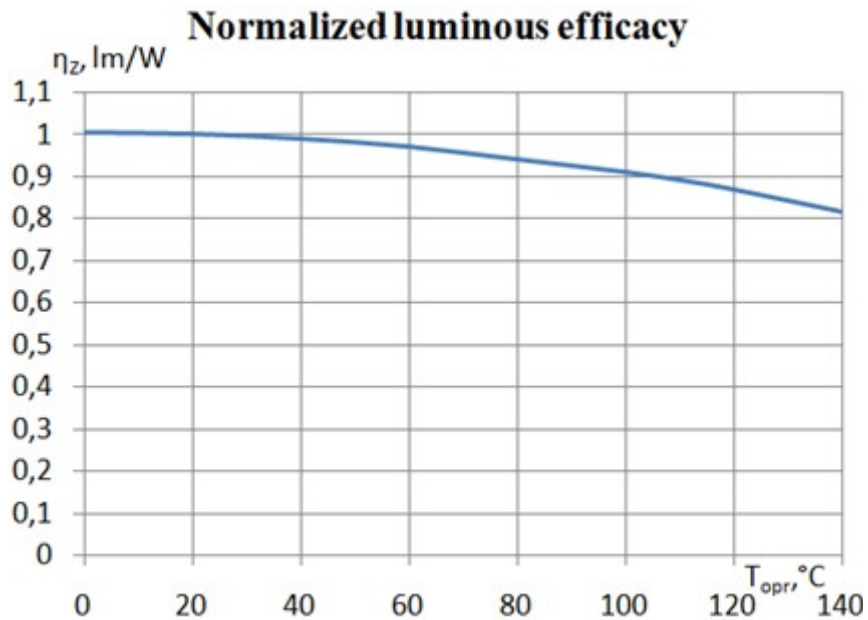


Figure 1.11: LED's luminosity-optics decrease with temperature

As shown in **figure 1.11**, the LED's brightness is lowered when it is continuously operated at elevated temperatures. The reason for this is the rapid degradation of the semiconductor structure causing its early deterioration.

Figure 1.12 shows the estimated life for a LED (Luxeon K2-Philips) depending on the junction temperature and the circulating electric current.

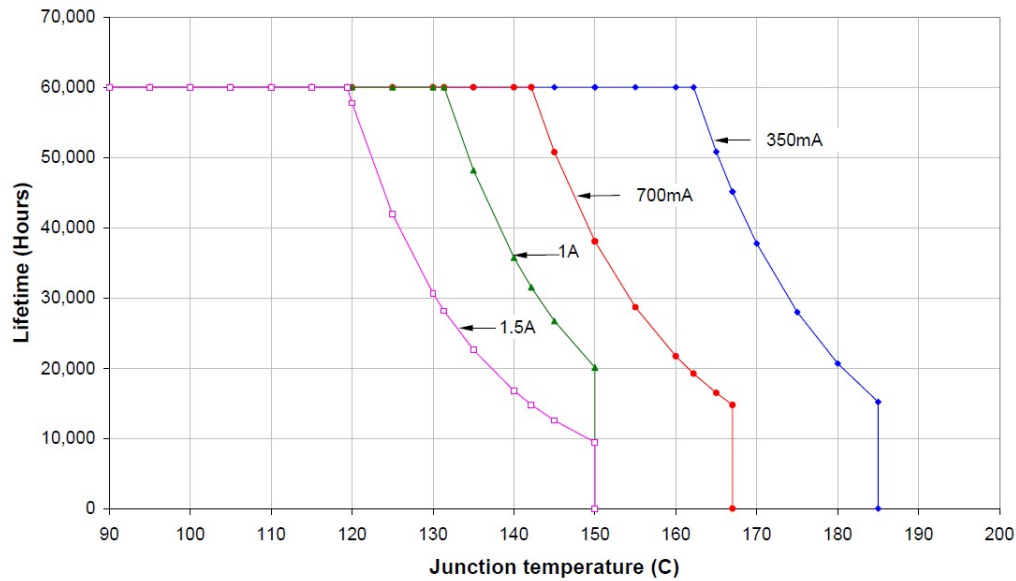


Figure 1.12: Estimated life for a Philips Luxeon K2 LED as a function of the temperature and for different power currents. courtesy of Philips

It is obvious that minimizing diode's temperature results in a LED life and brightness increase (higher current). Taking a look at the standard configuration of a SMD LED (surface mount diode), **figure 1.13**, a heat sink is assembled to directly transfer heat out from the diode to the PCB on which it is mounted.

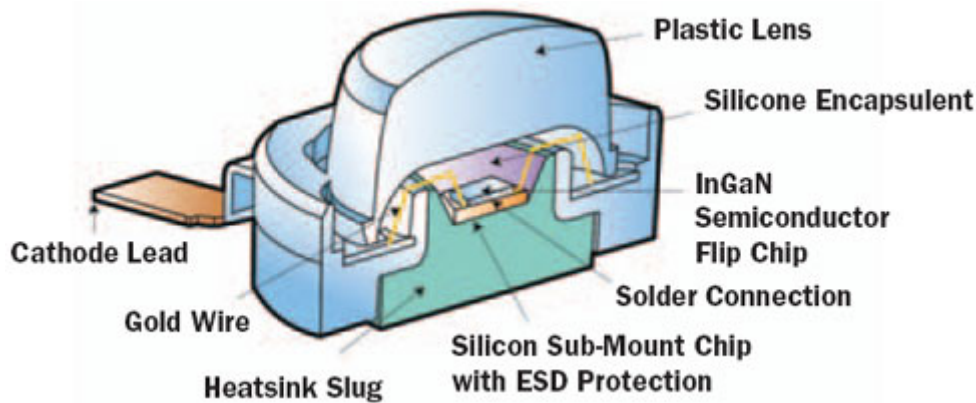


Figure 1.13: Sketch of a LED assembly.

Now, the challenge in refrigeration is, among others, how well the heat from the dissipater is evacuated to the surroundings. To this end, there are techniques and technologies that ensure an efficient heat dissipation to the surroundings [21, 22].

Taking into account the current challenge for getting lighting devices with longer duration light intensity when operating under severe conditions (high temperatures), LEDs manufacturers must deepen into the component's heat management.

1.3- Motivation

Overheating is a critical factor in the functionality of many high-power electronic devices (microprocessors, telecommunications, solar cells, wind power inverters, photovoltaics, electric traction systems, thermoelectric devices, LEDs, etc.). The reliability, lifetime and efficiency of these devices are severely limited by the speed at which the heat generated during their operation is dissipated.

Nowadays, electronics evolves towards smaller devices and components with greater operation capacity and so with greater heat generation (heat density). This heat increase together with components miniaturization make cooling needs increase and therefore their power consumption. As an illustrative example of the weight of cooling system's power consumption over total operating power consumption, the EMERSON's study is shown [23], **figure 1.14**.

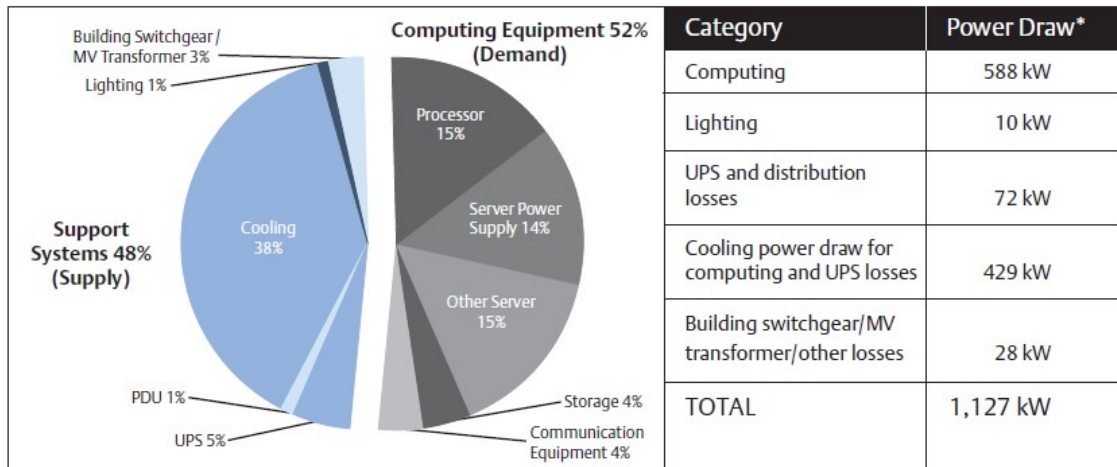


Figure 1.14: Thermal analysis of a 450m² data centre

The study shows that 38% of the total power consumption of a 450m² data centre is due to the cooling system. Therefore, it seems obvious the need to improve the cooling systems efficiency and / or reduce data centre power consumption, cascade effect. Effect due to which, a 1W power consumption reduction of a server component leads to 2.84W power consumption reduction of the whole data centre, **figure 1.15**.

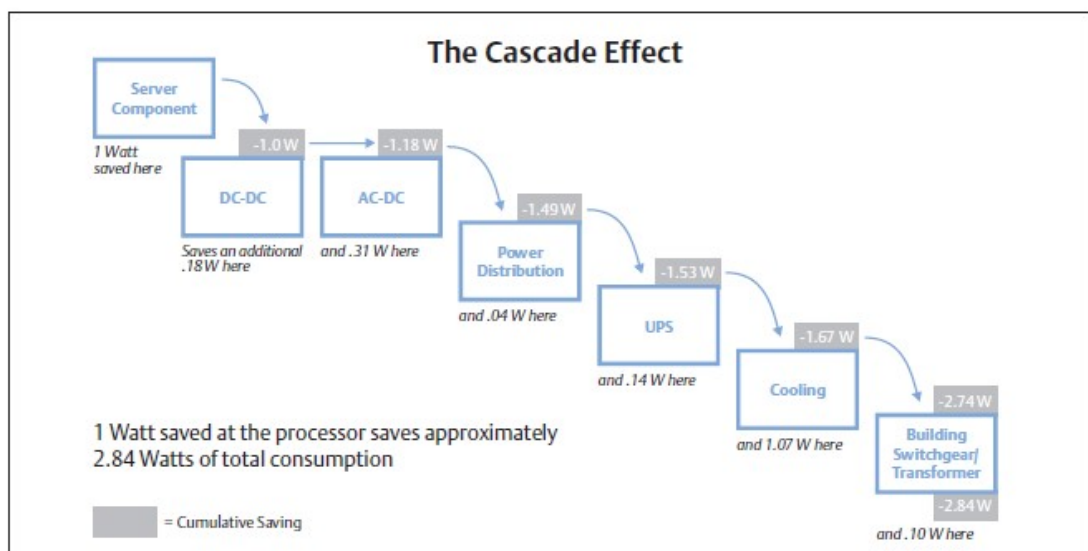


Figure 1.15: Cascade effect of the component’s consumption reduction on the global consumption

However, 1W reduction requires, among other things, that heat extraction be as much efficient as to keep component temperature below its maximum value..

For the particular case of thermoelectric systems, as discussed in the previous section, a heat exchanger thermal resistance reduction means a cooling capacity increase when operating as a cooler, or a power conversion increase as converter. As far as LEDs are concern, the lowering of the temperature at the junction allows to increase light quality and luminaire life.

All above has motivated the realization of this thesis which has focused on the development of a high efficient, passive, two-phase cooling device (specific LHP) for its application in a Bridgelux V15 LED..

Bibliography

- [1] Semiconductor Industry Association, The International Technology Roadmap for Semiconductors, 2009 Edition
- [2] Lee, F.C, Van Wyk, J.D, Boroyevich, D., Jhans, T., Chow, T.P., and Baboisa, P. “Modularization and integration as a future approach to power electronic systems”. Proceedings of 2nd International Conference on Integrated Power Systems (CIPS), 2002.
- [3] D.M Rowe, “Thermoelectric power generation”. Proceedings of Institution of Electrical Engineers, 125 (11R), 1113-36.
- [4] C.M Bhandary and D.M.Rowe , “Si-Ge as high temperature thermoelectric materials”. Contemporary Physics, 21(3) (1980), 219-42.
- [5] H.J. Goldsmind, “Aplications of thermoelectricity”. Methuen Monograph, London, 1960.
- [6] A.F.Ioeffe, “Semiconductor thermoelements and thermoelectric cooling”, Infosearch, London 1957.
- [7] D.M Rowe, C.M. Bhandary “Modern Thermoelectrics”. Holt, Rinehart and Winston Ltd. Eastbourne U.K.
- [8] Gao Min, D.M.Rowe “Improved model for calculating the coefficient of performance of a Peltier module”. Energy conversion & Management.41 (2000) 163-171.
- [9] Gavela D. Pérez Aparicio J.L. “Peltier pellet analysis with a coupled, non-linear, 3D FEM”. Proceedings of the 4th European Workshop on Thermoelectrics. Septiembre 17-18, 1998 Madrid Spain.
- [10] J.Esarte, M.Domínguez, J.Gonzalez, D.Astrain. “Simulation by electric analogy of a thermoelectric cheese dryer”. 5th European Workshop on thermoelectrics, Pardubice, Czech Republic, 1999.
- [11] M. Dominguez, J.M. Pinillos, P. Gutierrez. “Comprobación de un sistema de cálculo térmico por analogía con ordenador en una instalación con efecto Peltier”. Reunión bienal de la Real Sociedad de Física, Valladolid, Septiembre 1991.
- [12] M.Dominguez, D. García, J.Esarte,D.Astrain, J.Gonzalez “Possibilities of efficiency improvement in thermoelectric systems” Journal of Thermoelectricity, nº 2, 1999.
- [13] J.Esarte, J.Aguas, D.Astrain, JGonzalez. “Aplicación de la termoelectricidad en el diseño de un probetero y un expositor de vinos con control de temperatura”. 4th European Workshop on thermoelectrics”. Universidad de Comillas, Madrid. 1998.
- [14] M. Domínguez, J.Esarte, D. Astrain, J. González, J.Aguas. “Equipo de deshumidificación mediante tecnología termoelectrica”. Montajes e Instalaciones – Nº 338; Abril 2000
- [15] M.Domínguez, J.Esarte, J. Gonzalez, D.Astrain. “Equipo de deshumidificación mediante tecnología termoelectrica”. Montajes e instalaciones, nº 338 Abril 2000.

- [16]: M. Domínguez J. Esarte, D. Astrain, J. González. “Design and optimisation of a Thermoelectric Dehumidifier”. *Journal of Thermoelectricity* – N° 2; 2000.
- [17] J. Esarte, Gao Min, D.M. Rowe. “Modelling heat exchangers for thermoelectric generators”. *Journal of Power Sources* –Vol. 93/1-2; pages 72-76. Enero 2001
- [18] J. Esarte, Manuel Dominguez. “Capillary Mechanism for the Heat Dissipation through a Thermoelectric Pellet”. *Applied Thermal Engineering (Elsevier Science)* – Vol. 23, Issue 13. September 2003.
- [19] J. Esarte; J.M Blanco, C.Wolluschek, D.Prieto. Chapter 20 - “Heat dissipaters”. Book: “Modules, Systems, and Applications in Thermoelectrics and/or the Materials, Preparation, and Characterization in Thermoelectrics”, Volume 1-2 – 2012.
- [20] Piotr Swietoniowski, Tomasz Binkowski. “The influence of temperature on optical and electrical parameters of medium and high power LEDs”. *PRZEGLĄD ELEKTROTECHNICZNY*, ISSN 0033-2097, R. 90 NR 11/2014.
- [21] J.Esarte. “Técnicas de disipación térmica pasiva y activa en luminarias LED”. *PHOTONICS’10 Conferene. (Spain) May 2010.*
- [22] J.Esarte, J.M. Blanco, A. Bernrdini. “Loop Heat Pipe model for a 100W LED street Lights”. *CMN Conference. Bilbao (Spain) June 2013.*
- [23] <http://www.emersonnetworkpower.com/documentation/en-us/latest-thinking/edc/documents/white%20paper/energylogicreducingdatacenterenergyconsumption.pdf>

Chapter 2. Objectives and methodology

2.1- Objectives.	19
2.2- Thermal management challenges	19
2.2.1- Effect of the heat flow direction	20
2.2.2- Heatsink efficiency	22
2.3- Methodology and Contributions	33
Bibliography	33

2.1- Objectives.

Nowadays there is a tremendous concern about energy efficiency, respectful use of resources and the environment. More efficient equipment, better performance and longer life are aspects desired and sought. In LED lighting and thermoelectric devices "TEG" these aspects are conditioned by the die temperature [1,2,3,4,5]. The difficulty in economically and efficiently cooling these devices has led to the development of new architectures and materials [6,7] as well as to the development of new refrigeration technologies [8, 9, 10] more appropriate for the requirements demanded: miniaturization and high cooling capacity (heat pipes, vapour chambers, loop heat pipes, variable loop heat pipes, ...).

This thesis aim is to develop a heat pipe loop composed of a **structured primary wick** unlike the traditionally used porous wicks. A mathematical model predicting loop heat, LHP, pipe performance has also been developed. Model that allows to adjust the LHP design as well as to establish the influence of the different components and operating conditions on its cooling capacity.

This section gives an overview of the problem of heat conduction in electronics and highlights the contribution of this thesis.

2.2- Thermal management challenges

Given the importance of temperature over the efficiency, quality and lifespan of electronic devices (LEDs, TEG) the question is how to efficiently increase the heat extraction. Obviously, one of the first focuses of attention is the development of less electric resistive semiconductors (Joule effect), which leads to a lower heat generation. The other focus is on improving the mechanisms of heat transfer [11]. To improve these mechanisms, we must first know the mechanisms that limit dissipation [12]. Among these are:

- Material thermal properties, “**Bulk thermal resistance**”

- Thermal contacts between different materials, “**Thermal interface resistance**”.
- Components miniaturization, high heat densities. “**Thermal constriction/spreading resistance**”.
- Heat sink efficiency “**Dissipater thermal resistance**”

The first two points are closely linked to the materials science, better electric-thermal performance. As far as the last two are concerned, a description of them is made in the following sections.

2.2.1- Effect of the heat flow direction

Due to its simplicity, robustness and cost, air cooling is the most widely used technology in electronics, LEDs, and thermoelectricity. However, unlike other applications, electronics has the particularity of miniaturization, which means a **high heat flux density**. It is this high heat flux density the real bottleneck for the advance of more robust, longer life and higher capacity electronic components.

When defining a heat sink to cool down a component, it is no longer enough to know its standard heat resistance (calculated assuming a homogeneous heat flow across the entire base plate). If so, the component will certainly fail ahead of time since the actual temperature at which it is subjected is greater than that obtained analytically in view of that standard thermal resistance. This is due to the negative effect of the heat flow concentration or opening, which means an additional thermal resistance called constriction resistance [13,14], annex 5.

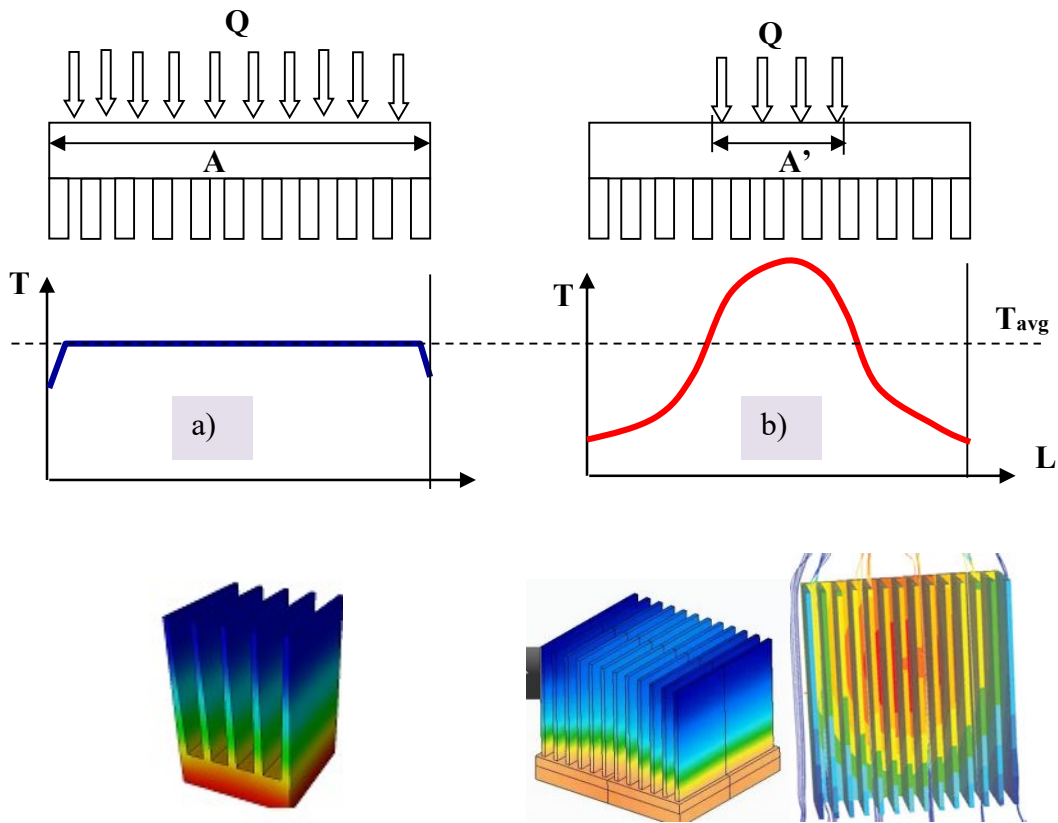


Figure 2.1: Temperature distribution on a "L" width heat sink base surface

Figure 2.1 shows, for the same "Q" heat flux, the component temperature as a function of how heat is distributed: figure 2.1 (a), evenly distributed over the entire surface of the heat sink base "A" and concentrated in a smaller surface "A'", figure 2.1 (b). It is observed that temperature reaches its maximum for case (b). This is due to the so-called constriction thermal resistance resulting from the " A'/A " aspect ratio. The lower this aspect ratio, the higher the maximum temperature reached and vice versa.

Apart from the aspect ratio, there is another factor that modifies the heat sink overall thermal resistance, it is component location at the base of the radiator, ie its eccentricity "e" with respect to the position centred at the base. The more eccentric, the higher the temperature at the source-radiator contact, figure 2.2.

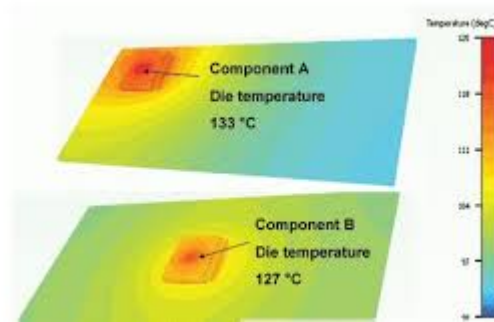


Figure 2.2: Effect of eccentricity on the heat source temperature.

From the above it is concluded that a good thermal characterization of the radiator is given by the thermal resistance that considers the aspect ratio and the eccentricity.

2.2.2- Heatsink efficiency

The last step in the heat evacuation is the convective heat transfer (natural convection or force) through extended surfaces (surface with fins) to the environment. The efficiency of convective heat transfer depends on several factors:

- Fin type
- Pitch or spacing between fins
- Fin dimensions

It is well known the effect of the heat exchanger's surface on the heat transfer efficiency. The larger, the more efficient the heat exchanger. The way to increase this surface is by mean of fins which can be of several types and configurations. Among the most widespread are the **smooth** and **straight** fins, although there are other types.

As far as the smooth-straight fins are concerned, their size and arrangement are key aspects to get a highly efficient dissipater, **low thermal resistance**. After a brief introduction of what is meant by thermal resistance, it is described the influence of several design parameters (number of fins, fin thickness, spacing between fins, fin height) on the smooth and straight fin dissipater thermal resistance.

Heat resistance is the resistance that any body or system offer to the flow of heat flowing through it and is defined as the ratio between the body's temperature increase to the heat flowing through it. This thermal resistance comprises two: the conduction and convection resistances.

$$R = R_{cond} + R_{conv} = \frac{T_{sup\ erf} - T_{base}}{\dot{Q}_{frig}} + \frac{T_{amb} - T_{sup\ erf}}{\dot{Q}_{frig}}$$

That's to say,

$$\boxed{R = \frac{T_{amb} - T_{base}}{\dot{Q}_{frig}}} \quad (^\circ C/W) \quad (2.1)$$

Being $\Delta T = T_{amb} - T_{base}$ the thermal drop between the temperature of the heatsink base and the surrounding temperature.

T_{amb} : surrounding temperature .

T_{base} : temperature of the heatsink base.

T_{superf} : Temperature of the heatsink finned surface.

\dot{Q}_{frig} : heat power to dissipate.

$R_{conv} = \frac{1}{h A_{sup\ erf}}$ where “h” is the convective heat transfer coefficient [15,16] and “ A_{superf} ”

the heat exchange surface.

According to equation 2.1, radiator's thermal resistance requires the determination of the temperature at its base once the cooling power and ambient temperature are known. However, this temperature is not something immediate but something very complex and laborious due to the complexity of the equations to solve [17,18]. Equations that derive from the approach of energy conservation in the heatsink and those for the mass, momentum and energy of the cooling air.

$$\nabla \cdot \rho \vec{V} + \frac{\partial \rho}{\partial t} = 0$$

$$\rho \frac{D\vec{V}}{Dt} = \rho \vec{g} - \nabla P + \mu \nabla^2 \vec{V}$$

$$\rho c \frac{DT}{Dt} = \nabla \cdot K \Delta T + \mu \Phi$$

$$\rho c \frac{\partial T}{\partial t} = \nabla \cdot K \Delta T \quad (2.2)$$

Equations for the fluid

Equation for the radiator

These equations determine the temperature reached in the heat sink as a function of the established limit conditions. These partial differential equations, due to their complexity and impossibility to obtain closed solutions, require numerical tools that allow their discretization and scalar transformation and thus their solution, in short, the calculus of the heatsink temperature at the base “ T_{base} ”.

2.2.2.1- Influence of design parameters on a straight fin dissipator: height, thickness, spacing.

As an example, considering forced convection (air velocity 2m / s and 50 ° C) and constant thermal power (Q), the following figures show the effect of fins size and arrangement on the heatsink thermal resistance..

Given a fixed dimensions radiator: a heat sink base of 100mm wide x 50mm long x 5mm high and fins of 25mm high and 2mm thick.

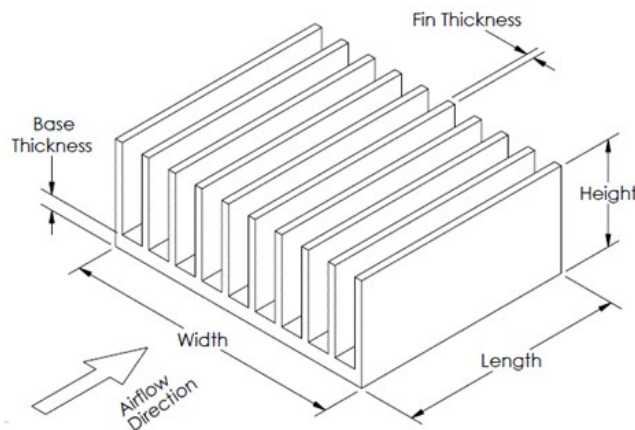


Figure 2.3: Straight fins radiator drawing.

In Figure 2.4, the effect of fin spacing is shown. As the spacing is decreased, the lower the thermal resistance. However, the spacing reduction has in counterpart an increase in the pressure loss, so the optimal solution is a compromise between the thermal resistance reduction and the pressure loss increase, in this case $1.5 < e_{opt} < 3\text{mm}$.

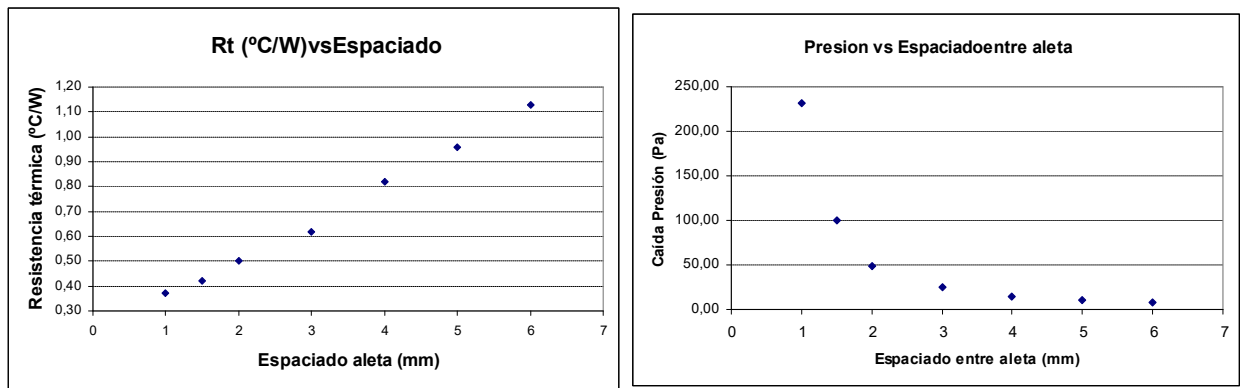


Figure 2.4: Effect of fin spacing on thermal resistance and pressure loss.

As far as the fin thickness effect on the heat sink thermal resistance is concern, it is shown in figure 2.5. (for a 2mm fin spacing).

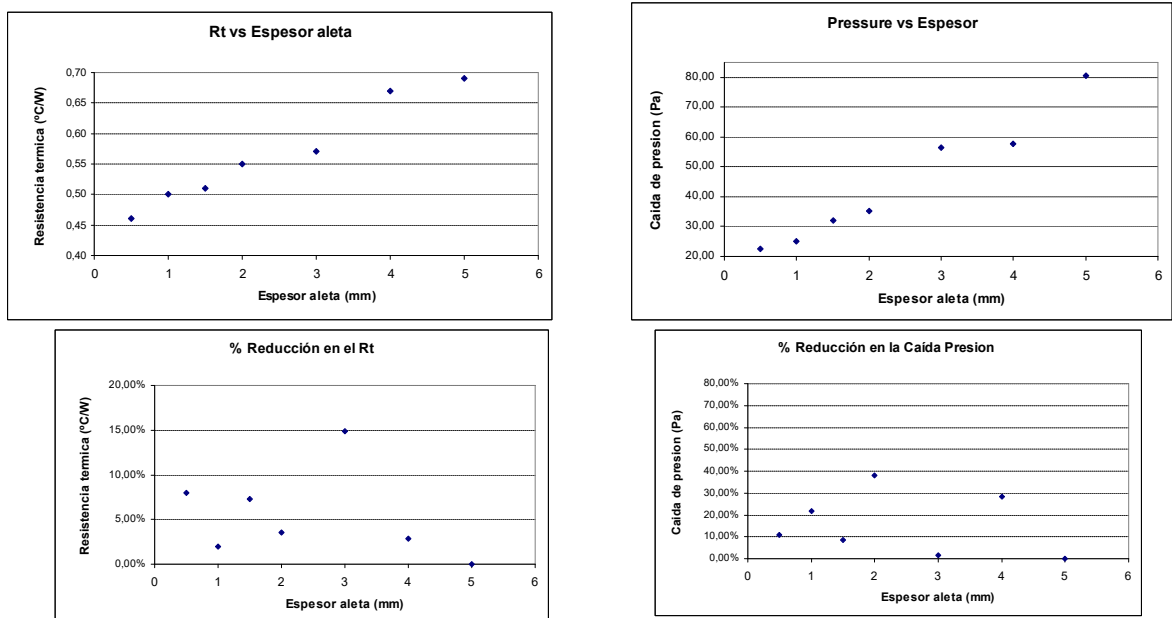


Figure 2.5: Effect of fin thickness on thermal resistance and pressure loss.

As the thickness increases, the higher the thermal resistance and the pressure loss. However, it is observed that at fin thickness lower than 2mm the percentage reduction of both thermal resistance and pressure loss are relatively high (5-10% and 10-40% respectively).

Fin height effect is shown in Figure 2.6. As fin height increases, both thermal resistance and pressure loss decrease. However, there is a fin height (50mm) from which thermal resistance percentage remains constant, 6-7%. At the same time, thermal resistance for fin heights larger than 50mm are low and almost constant. So, thermal resistance improvement does not compensate the material increase.

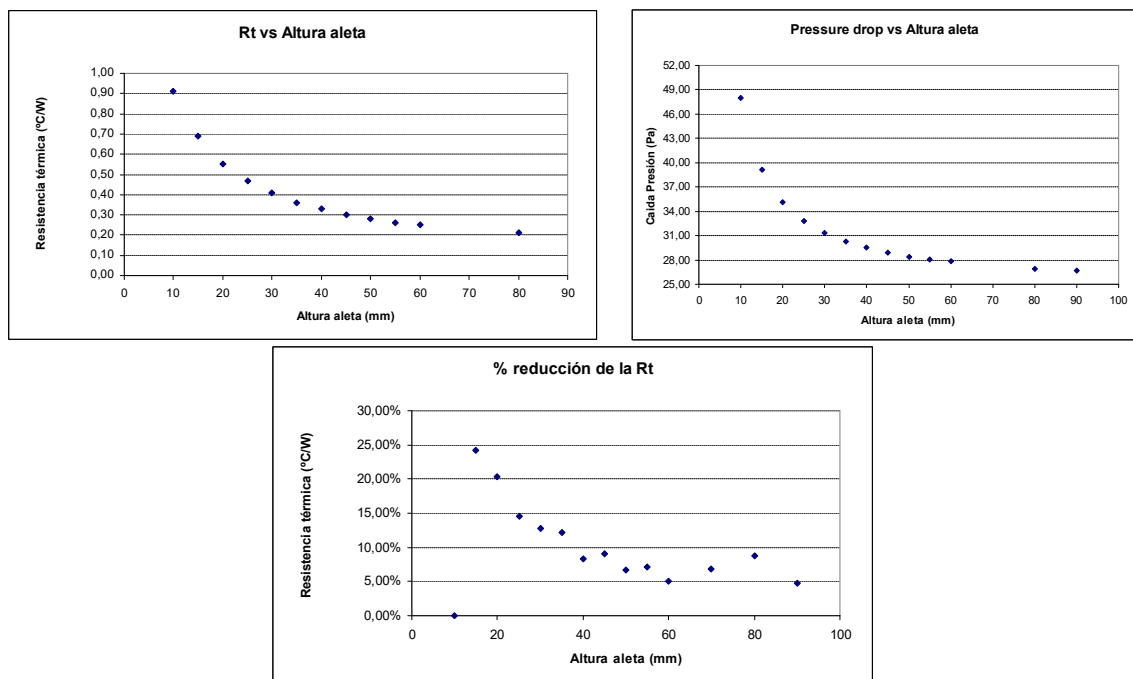


Figure 2.6: Effect of fin height on thermal resistance and pressure loss.

Conclusions about fin effect.

1. For a fixed air flow rate and a fixed radiator base, it turns out that the larger the number of fins (smaller the spacing between fins) the **lower the heatsink thermal resistance**.

2. A smaller spacing between the fins supposes a **greater resistance to the air flow**, larger pressure loss, what means a bigger fan to keep the same air flow rate.
3. For a constant flow rate, the thermal resistance and the pressure drop are inversely proportional to the fin height, if it increases then thermal resistance and pressure loss decrease.

2.2.2.2- Effect of fin type; Comparison between rectangular and triangular fins.

Extended surfaces are used to increase the convective heat transfer coefficient between heatsink and the surrounding [19]. Thus, low convective coefficient is compensated in some way with the increase of area in contact with the fluid, expression (1):

$$\dot{Q} = h \cdot S \cdot (T_{\text{superf}} - T_{\text{amb}}) \quad (1)$$

Fin configurations found nowadays in the market vary very much in geometry and sophistication-complexity. These configurations are designed for very specific applications requiring of high performance working under maximal constraints such as space [20]. In spite of the multitude of variants in the fin geometries, this section analyces the influence of fin geometry on its thermal resistance [21], to finish by making a comparison between a triangular longitudinal fin and a rectangular one.

For the analysis of triangular fin thermal, a Matlab analytical model predicting fin cooling capacity has been developed.

The developed tool can predict temperature, cooling power and efficiency of a longitudinal rectangular and triangular fin. The basic defining parameters of a triangular fin are shown in figure 2.7.

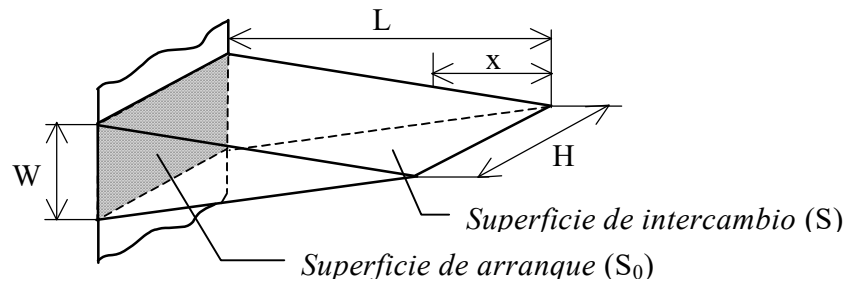


Figure 2.7. Triangular fin's dimensions used for analysis

For the study of a longitudinal, triangular or rectangular fin, the following considerations are made:

- Forced convection all around fin, including the end.
- Fin of aluminium.
- Temperature at the fin's base is **fixed**.
- Fin length is **constant**.
- The fin is thin enough to account for **unidirectional** flow.
- Heat loss through the fin's ends are **neglected**.

Temperatures

Temperatura of a triangular fin is given by:

$$\frac{d^2\beta}{dX^2} + \frac{1}{X} \cdot \frac{d\beta}{dX} - \frac{\phi^2}{4} \cdot \frac{\beta}{X} = 0 \quad (2)$$

Where:

$$\beta = \frac{T - T_{amb}}{T_0 - T_{amb}} \quad (3)$$

$$\phi = \sqrt{\frac{2 \cdot h \cdot f \cdot L}{K \cdot W}}, \quad \text{being } f = \sqrt{1 + \left(\frac{W}{2L}\right)^2} \quad (4)$$

$$X = \frac{x}{L} \quad (5)$$

Solving the differential equation of the second order, and applying the corresponding boundary conditions, gives the following expression for the temperature:

$$\beta = \frac{I_0(\phi \cdot \sqrt{X})}{I_0(\phi)} \quad (6)$$

Where “ I_0 ” is the modified Bessel’s function of first specie and order zero.

Cooling power

Cooling power for a triangular fin is given:

$$\dot{Q} = -K \cdot S_0 \cdot \left(\frac{d\beta}{dX} \right)_{X=L} = \dots = -\frac{2 \cdot f \cdot h \cdot L \cdot K}{\phi} \cdot 2 \cdot \frac{I_1(\phi)}{I_0(\phi)} \cdot (T_0 - T_{amb}) \quad (7)$$

Where “ I_1 ” is the modified Bessel’s function of first specie and first order.

Efficiency

Finally, the efficiency of a triangular fin is given by:

$$\eta = \frac{2}{\phi} \cdot \frac{I_1(\phi)}{I_0(\phi)} \quad (8)$$

With the above formulation a Matlab model is created, "FinStudy". It allows to quickly determine fin performance depending on its geometry, triangular or rectangular. Previous to use it to evaluate the influence of geometric parameters, its validation is done by comparing its predictions with those coming from a CFD model, figure 2.8.

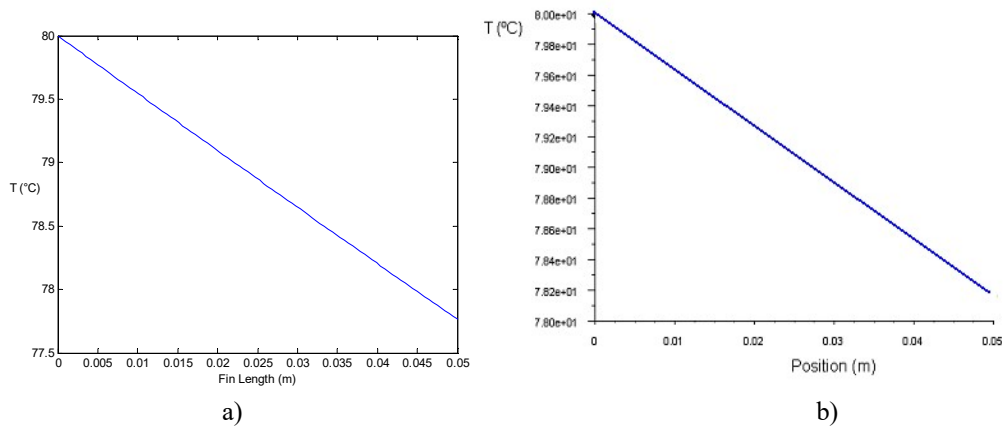


Figure 2.8. Distribution of the temperature along the fin, from the base to the tip being $W = 10\text{mm}$. A) CFD case; B) Finstudy case

As can be seen in figure 2.8, both CFD and Finstudy establish the same temperature profile along the fin length. Nevertheless, Finstudy predicts a temperature at the fin tip a little bit higher (0.4% higher, $78.1\text{ }^{\circ}\text{C}$) than that predicted by CFD ($77.8\text{ }^{\circ}\text{C}$).

a) Effect of base width "W" on triangular fin.

For this analysis, both the fin height and length ($L = 50\text{ mm}$, $H = 450\text{ mm}$ respectively) are fixed while width "W" is variable..

Figure 2.9 shows the fin efficiency for the following conditions: 80°C temperature in the fin base and 25°C ambient temperature.

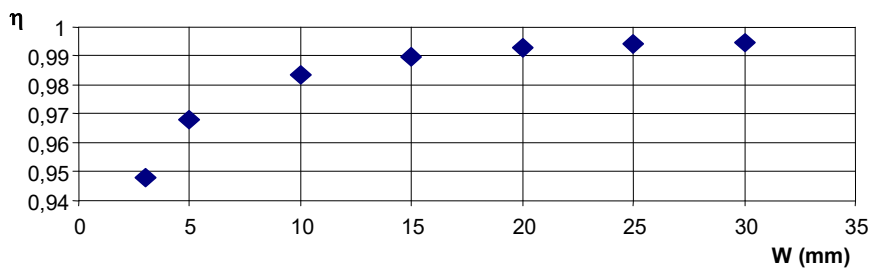


Figure 2.9. Effect of fin width on efficiency.

It is observed that as the fin width increases, the fin effectiveness also does [22,23]. However, from a given width (15 mm in this case) the efficiency increase is hardly appreciated. Therefore, 15mm can be considered the maximum value for this case.

b) Effect of the height "L" of the triangular fin.

In this case, three fin heights are analyzed: 50, 70 and 100 mm, for a fin width of $W = 5$ mm and a length $H = 450$ mm. The result is shown in Figure 2.10, where we can see the surface temperature for the three mentioned lengths.

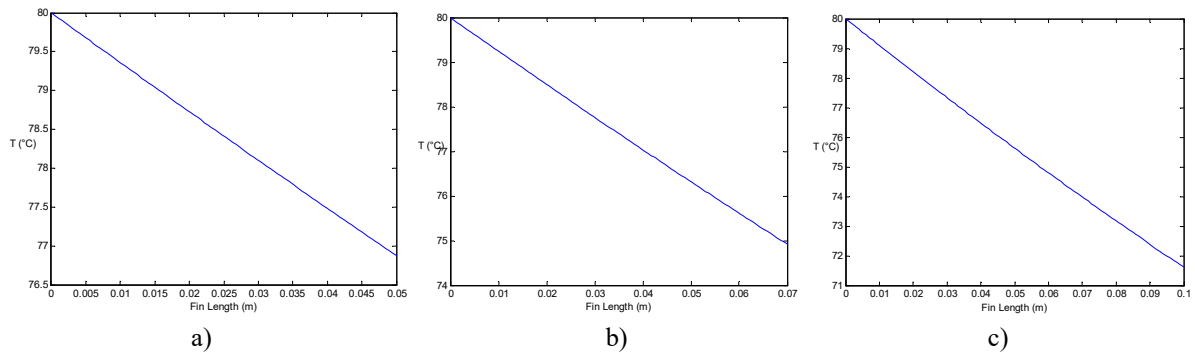


Figure 2.10. Fin's surface temperature; A) $L = 50$ mm; B) $L = 70$ mm; C) $L = 100$ mm.

As the fin height increases, the fin tip temperature decreases as well as the cooling power, resulting in a fin effectiveness reduction [24], table 2.1. Apart from that, the fin weight increases.

Tabla 2.1. Fin height effect on the heat dissipation

L (mm)	\dot{Q} (W)
50	95,13
70	95,05
100	95

c) *Comparative between rectangular-triangular fin.*

One of the issues that always appear when designing a heatsink is to decide between a rectangular or triangular fin. In this section we compare the efficiency of both configurations for a fin of $L = 50\text{mm}$ and the same outer surface "S".

Figure 2.11 shows that temperature at the rectangular fin tip is lower than in a triangular one. It gives an idea how large the rectangular fin's thermal resistance is compared to that of the triangular one for the same outer surface.

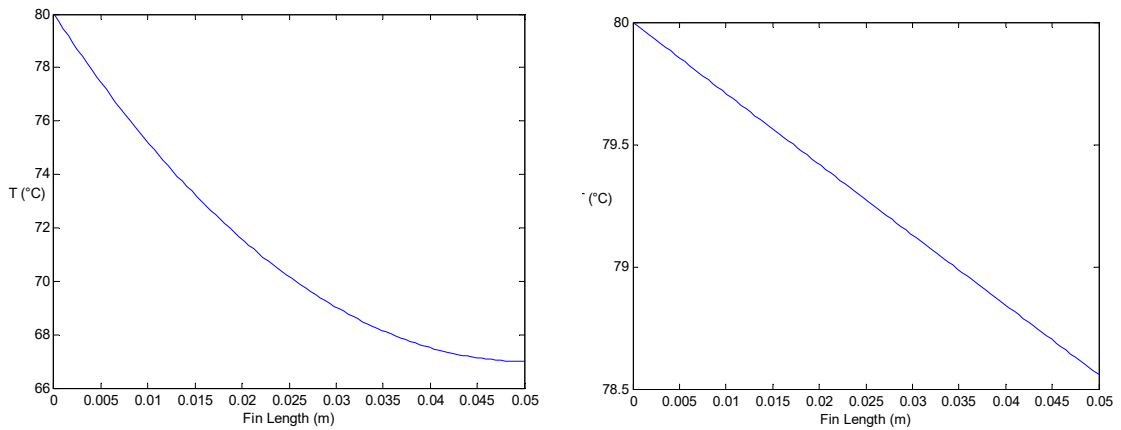


Figure 2.11. Surface temperature distribution; a) rectangular fin, b) triangular fin.

The efficiency ratio between the two fins is:

$$\frac{\eta_T}{\eta_R} = 1.04 \quad (13)$$

That is to say, the triangular fin's efficiency is 1.04 times greater than that of the rectangular one.

2.3- Methodology and Contributions

In electronics, thermal management is today the great challenge to overcome in order to advance in the development of ever smaller components, with a higher level of operation and functionality. The main topic of this thesis is the cooling capacity improvement of two-phase passive cooling devices, LHPs. To do this, a thermal model of such device is generated, the effect of the porous media is theoretically and experimentally analyzed and finally a two-phase passive device is constructed and characterized in order to experimentally measure its performance.

Chapter 1 and 2 highlight the motivation as well as the technical challenges that have led to the development of this thesis. Chapter 3 studies the fluid-mechanics in porous media, capillary ascent, as a key element in the operation of these two-phase, passive devices. In Chapter 4 it has been developed a mathematical model that predicts the fluid-thermal behavior of this LHP, while providing a more in-depth information on the influence of several variables (porous media type, among others) on its cooling capacity. Chapter 5 describes the manufacturing and experimental tests carried out on the LHP, as well as LHP's model validation as tool to assist in the LHP's design. Finally, the conclusions section contains the conclusions and future lines of improvement.

BIBLIOGRAPHY

- [1] B. Ya. Moizhes. “The influence of the temperature dependence of physical parameters on the efficiency of thermoelectric generators and refrigerators”. *Fizika Tverdogo Tela*, Vol 2, No. 4. 1960
- [2] Jeffrey W. Fergus. Oxide materials for high temperature thermoelectric energy conversion. *Journal of the European Ceramic Society*. Volume 32, Issue 3, Pages 525–540. 2012
- [3] Dr. Faruk Yildiz, Mr. Keith L. Coogler Dr. “Low Power Energy Harvesting with a Thermoelectric Generator through an Air Conditioning Condenser”. 121st ASEE Annual Conference&Exposition. 2014.
- [4] Chao Ma ; Hongming Zhang ; Kaiyun Cui ; Minyu Yao. “Effects of LED lighting degradation and junction temperature variation on the performance of visible light communication”. *International Conference on Systems and Informatics (ICSAI)*, IEEE 2012.

- [5] P. Dalapati, N. B. Manik., and A. N. Basu. “Effect of temperature on the intensity and carrier lifetime of an AlGaAs based red light emitting diode”. *Journal of Semiconductors*, Vol.34, No9. 2013.
- [6] Julian Carey; New LED architectures and phosphor technologies lower costs and boost quality. *LED’s Magazine*, September 2014.
- [7] P. Kongetira, K. Aingaran, and K. Olukotun. Niagara: A 32-way multithreaded SPARC processor. *IEEE Micro*, 25(2):21–29, 2005.
- [8] M. Domínguez, D. García, J. Esarte, D. Astrain, J. González. “Possibilities of efficiency improvement in the thermoelectric systems”. *Journal of Thermoelectricity* – N° 2; 31-40. 1999
- [9] Maite Aresti, Cecilia Wolluschek. “Experimental Study on Chemical Stabilization of Nanofluids Suspension”. *Congreso Imagenenano-Bilbao*. 2011.
- [10] Amir Faghri, “Heat Pipes: Review, Opportunities and Challenges”. *Frontiers in Heat Pipes (FHP)*, 5, 1. 2014.
- [11] Ram Ranjan, Abhijeet Patel, Suresh V. Garimella *, Jayathi Y. Murthy. “Wicking and thermal characteristics of micropillared structures for use in passive heat spreaders”. *International Journal of Heat and Mass Transfer*. 2012
- [12] J. Esarte; J.M Blanco, C.Wolluschek, D.Prieto. “Modules, Systems, and Applications in Thermoelectrics and/or the Materials, Preparation, and Characterization in Thermoelectrics”; Chapter 20-Heat Dissipaters. Volume 1-2 – 2012.
- [13] Seaho Song, Van Au, Seri Lee, Kebin P. Moran. “Constriction/Spreading resistance model for electronics packaging”. *ASME/JSME Thermal Engineering Conference: Volume 4 ASME 1995*
- [14] Nadia Aderghal, Tahar Loulou, Ali Bouchoucha, Philippe Rogeon. “Analytical and numerical calculation of surface temperature and thermal constriction resistance in transient dynamic strip contact”. *Applied Thermal Engineering*, Volume 31, Issues 8–9, Pages 1527–1535. 2011.
- [15] Todd M. Ritzer and Paul G. Lau, “Economic Optimization of Heat Sink Design”, 13th International Conference on Thermoelectrics, Kansas City, Missouri, August 30 - September 1, 1994.
- [16] Lau P.G., Ritzer T.M. and Buist, R.J., “Thermodynamic Optimization of Heat/Cold Sink Extenders in Thermoelectric Cooling Assemblies”, 13th International Conference on Thermoelectrics, Kansas City, Missouri, , 1994.
- [17] R.W. Fox y A.T. McDonald, “Introducción a la mecánica de fluidos”. Editorial McGraw-Hill, 2ª edición.
- [18] J. Esarte, Gao Min, D.M. Rowe. “Modelling heat exchangers for thermoelectric generators”. *Journal of Power Sources* –Vol. 93/1-2; pages 72-76. 2001.
- [19] Y.A. Çengel, *Heat Transfer: A Practical Approach*, 2nd Edition, McGraw-Hill, Boston, (2003).

- [20] D.K. Tafti, G. Wang and W. Lin., “Flow transition in a multilouvered fin array”, *Int. J. Heat Mass Transfer*, 43, pp. 901-919, (2000).
- [21] J.M.Blanco, J.Esarte; E. Armendariz “Optimization of fin sinks through a parametric study of heat transfer”. *Journal of Advanced Thermal Science Research* 2014, 1, 3-8
- [22] M.S. Söylemez, “On the optimum heat exchanger sizing for heat recovery”, *Energy Conversion & Management*, 41, pp. 1419-1427, (2000).
- [23] J.R. Culham and Y.S. Muzychka, “Optimization of plate fin heat sinks using entropy generation minimization”. *IEE Transactions on Components and Packaging Technologies*, 24, 2, (2001).
- [24] S. Lee, “Optimum design and selection of heat sinks”. *Eleven IEE SEMI-THERM Symposium*, (1995).

Chapter 3. Capillarity in porous media

3.1 Introduction	37
3.2 Fluid-dynamic in a porous medium	39
3.2.1- Macroscopic mathematical approach.	40
3.2.2- Wick loading curve	44
3.2.3-Permeability	47
3.3. Experimental characterization	51
3.3.1- Loading curve	51
3.3.2- Permeability	59
Bibliography	65

3.1 Introduction

One of the main operating elements of a thermal superconductor is the porous medium, figure 3.1.

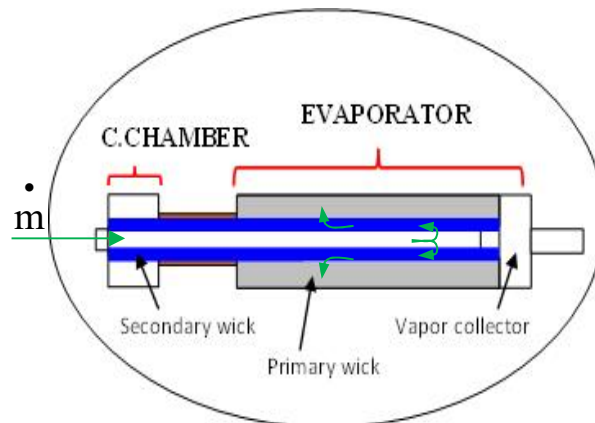


Figure 3.1: LHP scheme with detail of the location of the wicks or porous media.

The type of material, porosity, internal structure, geometry and wettability are, among others, determinants of the porous medium performance, wick.

The wick fundamental role is:

- To pump the fluid through the entire system and wick in particular, overcoming the system's head losses. This pumping capacity is called "*capillary action*".
- To secure the liquid-vapor interface where the evaporation takes place.

This element establishes one of the operating limits of these two-phase heat transfer devices, the so-called "**capillary limit**".

As for capillary or capillary action, as discussed above, it is defined as the ability of a porous medium to pump a liquid through it without the action of external forces (eg gravity). This is observed: when a paper is placed on a wet surface and it starts getting wet or when a capillary tube is introduced into a glass of water and it is observed how water ascends by its interior, figure 3.2; **Annex 5**



Figure 3.2: Wick performance.

The capillary action is a consequence of the intermolecular forces that appear in the three interfaces that appear among the liquid, solid and gas that result in a net force "F" on the liquid that causes it to move, figure 3.3.

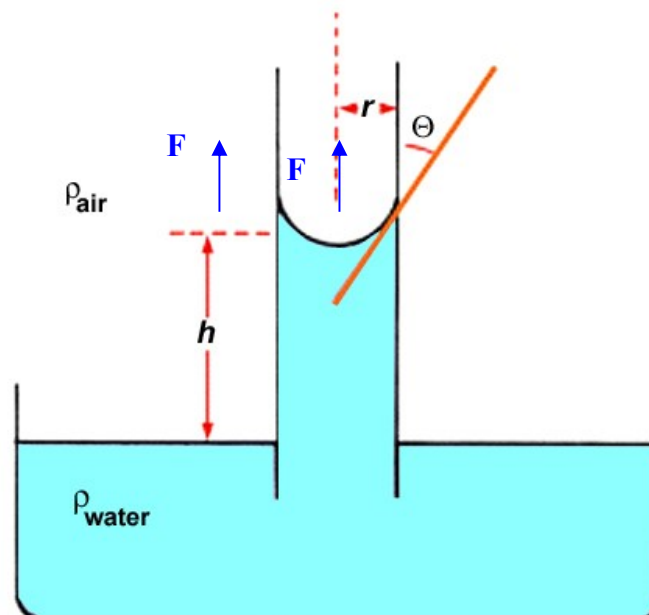


Figure 3.3: Intermolecular forces.

The most widespread porous medium in thermal superconductors is powder sintering (different materials and sintering parameters) [1-3], meshes and grooves. However, there are other techniques to obtain a porous medium.:

- • *Metal foams*, one of the most commonly used techniques is the replica of a polyurethane preform. Preform that determines pore size and distribution. These media have fairly spherical pores, as well as a fairly homogeneous metal connection, Figure 3.4.

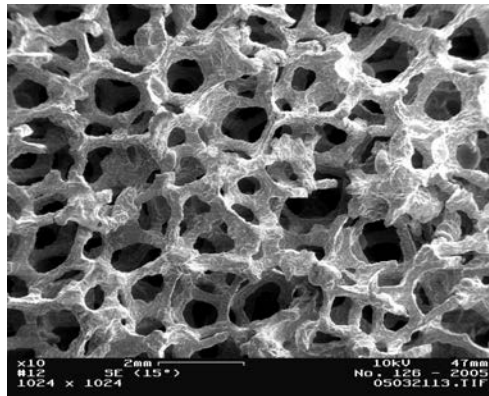


Figure 3.4: SEM image of an aluminium metallic foam

- • *3D Printing - Selective laser melting (SLM)*. This technology allows the rapid fabrication of complex geometries that otherwise would not be possible. It also allows to create the pore's size, distribution and connection in a specific and controlled way, figure 3.5. This technology is based on the contribution of metal powder while being fused by the application of a laser.

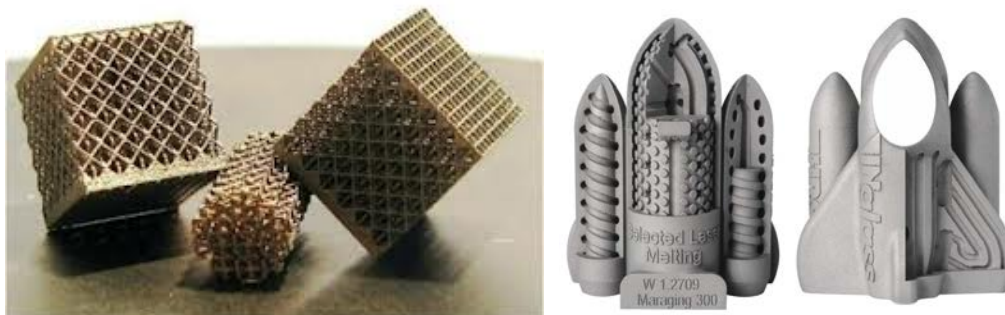


Figure 3.5: Image of stainless steel structures manufactures by SLM.

It is crucial to know how parameters such as porosity, pore size, pore distribution, material and internal structure affect this porous medium's capillary action of when designing a two-phase thermal device.

In the following section the fluid mechanics in porous media is analyzed in order to evaluate the influence of the mentioned parameters.

3.2 Fluid-dynamic in a porous medium

As discussed above, the heat transfer capacity of two-phase devices (LHP) is subject to several restrictions. One of these is the so-called "*capillary limit*", which represents the maximum heat power the device is capable of transport before dry spots appear on the

evaporator's wick. If this occurs, it is because the wick's capillary pumping capacity or flow velocity of the liquid through the wick is less than the liquid evaporation rate at the liquid-vapor interface.

It is therefore fundamental to know this advance velocity of the fluid through the porous medium in order to be able to estimate if a porous medium, together with its characterizing parameters, is able to ensure the required heat power transport.

3.2.1- Macroscopic mathematical approach.

This is a discipline within the fluid mechanics particularized to the flow through porous medium whose flow restriction depends on parameters such as: porosity, pore size, internal configuration, materials "wettability θ ".

In the theoretical scope the fluid dynamics in these media can be realized at both microscopic and macroscopic level.

- *Microscopic approach.* It implies that the well-known Navier-Stokes equations apply as such to the domain of the medium at pore-scale. In this approach, the field of velocities and pressures refer to the pore-scale velocities and pressures “ \vec{u}_p ” y “P” within the medium. However, the solution of these equations requires a significant effort for complex geometries since they require a precise definition of the media internal structure, something that is very complex to define and / or measure given the three-dimensional, random and isotropic character of these structures. Only in very simple cases (meshes, dust deposited freely, ...) can be defined precisely this structure and therefore be able to solve.
- *Macroscopic approach.* In this approach, the Navier-Stokes equations apply to a domain in which the porous medium has no internal structure, it is considered open to the fluid. In such case, the effect of the internal structure is taken into account by means of three macroscopic parameters: the so-called permeability "K", inertial coefficient "CE" and porosity " ε ". These in turn, represent the porous structure internal forces: viscous and inertial forces. Under this approach, the fluid velocity is a macroscopic value “ \vec{u} ” which is related to the real microscopic velocity (pore level) through the porosity parameter “ ε ”, $\vec{u} = \vec{u}_p \varepsilon$.

According to the macroscopic approach, the N-S equation is written as follows:

1- *Momentum conservation:*

$$\underbrace{\frac{1}{\varepsilon} \left[\frac{\partial}{\partial t} (\rho \bar{u}) + (\bar{u} \cdot \nabla) (\rho \bar{u}) \right]}_{\text{A}} = \underbrace{-\nabla p \mathbf{I}}_{\text{B}} + \underbrace{\rho \mathbf{g}}_{\text{C}} + \underbrace{\frac{\mu}{\varepsilon} \nabla^2 \bar{u}}_{\text{D}} - \underbrace{\frac{\mu}{\mathcal{K}} \bar{u}}_{\text{E}} - \underbrace{\frac{C_E}{\mathcal{K}^{1/2}} \rho |\bar{u}| \bar{u}}_{\text{F}} \quad (1)$$

- A: Macroscopic inertial force
- B: Pressure gradient
- C: Gravity force
- D: macroscopic viscous force, Brinkman term
- E: microscopic viscous force, term Darcy
- F: inertial microscopic force.

2- *Mass conservation:*

$$\boxed{\frac{\partial(\varepsilon \rho)}{\partial t} + \nabla \cdot (\rho \bar{u}) = 0} \quad (2)$$

Being

- “ ρ ” fluid density,
- “ ε ” medium porosity = V_h/V , “ V_h ” is the volume of voids y “ V ” the total volume.
- “ \bar{u} ” Darcy velocity or macroscopic velocity
- “ \mathcal{K} ” permeability,
- “ μ ” dynamic viscosity of the fluid,
- “ C_E ” macroscopic inertial coefficient.

Permeability “ \mathcal{K} ” and the macroscopic inertial coefficient “ C_E ” represent the resistance that the medium offers to the fluid flow. Such resistance depends on the porosity and tortuosity of the medium or the inter-connection among pores and on the type of fluid for the case of the permeability.

In general, it is necessary to determine them experimentally.

Equation (1), (2) represents the general form of the averaged NS equations; however, for the case of advanced two-phase devices, these are simplified because the following requirements are satisfied in capillary pumped flows:

- The flow is laminar, incompressible
- Newtonian fluid
- The movement of the fluid is by capillarity, whereby inertial forces are zero, “ C_E ” =0

Hence equation (1) is:

$$\boxed{\frac{1}{\varepsilon} \left[\frac{\partial}{\partial t} (\rho \bar{u}) + (\bar{u} \cdot \nabla) (\rho \bar{u}) \right] = -\nabla p \mathbf{I} + \rho \mathbf{g} + \frac{\mu}{\varepsilon} \nabla^2 \bar{u} - \frac{\mu}{\mathcal{K}} \bar{u}} \quad (3)$$

The obtaining of the macroscopic advance speed implies to solve the system of equations (2 and 3) which are difficult due to the complex nature of the porous structures., “ \mathcal{K} , ε ”.

However, for porous media used in two-phase heat transfer devices, two further requirements are satisfied:

- • stationary flow and
- • unidirectional flow

Which simplifies the system of equations (2 and 3) as follows:

Mass conservation

$$\frac{\delta U}{\delta z} = 0 \quad (4)$$

Momentum conservation

$$\frac{\rho}{\varepsilon} \left(U \frac{\delta U}{\delta z} \right) = -\frac{\mu}{\mathcal{K}} U - \nabla P + \rho g \quad (5)$$

Combining (4) and (5) provides the *macroscopic flow rate* or liquid front velocity, **Darcy's equation**.

$$U = \frac{-\mathcal{K}}{\mu} \cdot \left(\frac{dP_l}{dz} - \rho g \right) \quad (6)$$

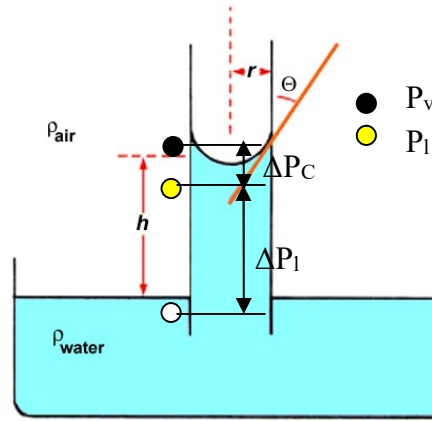


Figure 3.6: Pressure variation with height.

The pressure variation in the liquid phase with the height " dP_l/dz ", figure 3.6, is in turn related to the capillary pressure of the porous medium, which is defined:

$$\Delta P_c = \frac{2\sigma \cos \theta}{r_{eff}} \quad (\text{has to do with the curvature of the liquid-gas interface}) \quad (7)$$

Like wise $\Delta P_c = P_v - P_l$, what results in

$$P_l = P_v - \Delta P_c = P_v - \frac{2\sigma \cos \theta}{r_{eff}} \quad (8)$$

By incorporating (8) into (6), the *forward velocity or pumping capacity* is given as a function of the porous media geometric characteristics, material compatibility and fluid properties, expression (9):

$$U = \frac{-K}{\mu} \cdot \left(\frac{d \left(P_v - \frac{2 \cdot \sigma \cdot \cos \theta}{r_{eff}} \right)}{dz} - \rho g \right) \quad (9)$$

Expression that determines the liquid velocity through the porous medium as a function of the wick height, wick physical characteristics and the capillarity. There are a lot of technical work done regarding the obtention of a closed solution to equation (9) [4]. A simple solution is the Washburn equation, which determines the capacity of capillary pumping or pumping height as a function of time.

$$h^2 = \frac{r_{eff} \sigma \cos \phi}{2\mu} t \quad (10)$$

Considering the mass absorbed results:

$$m_c = (\rho A \varepsilon) \sqrt{\frac{r_{eff} \sigma \cos \phi}{2\mu} t} \quad (11)$$

However, this expression applicability is subject to conditions: porous medium with uniform pore distribution and constant pore size and when gravitational forces are negligible compared with the capillaries. But these conditions rarely occur in real cases, therefore the values predicted by Washburn equation differ from those obtained experimentally [5,6]. In spite of everything, due to its simplicity, it is an expression very often used to obtain some guiding values.

Other researchers have developed a solution of the exponential type [7], which best fits the experimental curve of porous medium pumping capacity, **load curve**.

Maximum reachable height

From this expression (9) there is an interesting feature of the porous media that can easily be obtained, this is the **maximum height** that the wick is capable of pumping liquid. The maximum height is the one at which the velocity becomes zero $U=0$, lo que resulta:

$$\frac{2\sigma \cos \theta}{r_{eff} \rho g} = h_{max} \quad (12)$$

3.2.2- Wick loading curve

The knowledge of the advance speed "U" through the wick is fundamental when defining the most appropriate wick for the two-phase device. This wick must satisfy that the advance speed is equal to or greater than the liquid evaporation rate in order to ensure its optimum operation..

$$\dot{m} \leq \dot{m}_C \quad (13)$$

Being: “ \dot{m}_C ” mass Flow rate; “ \dot{m} ” evaporation rate.

As discussed above, the equation (9) solution is complex and experimentation is presented as the alternative to establish the relationship between pumping capacity and wick properties. This

relationship is called **wick loading curve** [7, 8]. This can be given as a function of liquid height or mass absorbed.

Description of measurement method

The experimental measurement requires a simple device such as the one shown in Figure 3.7.

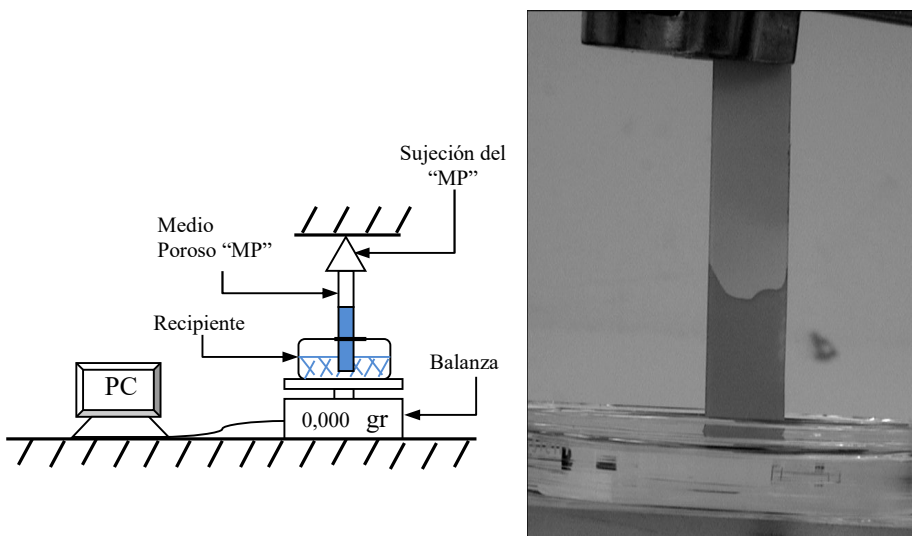


Figure 3.7: Capillary pumping measurement equipment

Device that has the following elements:

- a container in which to place the liquid
- a wick sample clamping arm
- a stopwatch
- a balance or video camera
- measurement scale

Measurement procedure. Firstly, the equipment is prepared: the vessel is filled with liquid, the wick sample is grasped at one end by the clamping arm and then the weight or chamber is switched on. Subsequently, if the mode of measurement is mass, the vessel is placed in the weight "Sartorius MA45" and the initial mass of liquid in the vessel is measured. Then, the holding arm with the wick sample is placed vertically next to the weight submerging the other end of the wick's sample into the vessel. Immediately afterwards the register of weight (mass variation) and time begins. Weights recorded are subtracted from the initial value to obtain the mass absorbed by the wick as a function of time, **loading curve**. This curve has the shape shown in figure 3.8 (sintered powder Nickel and water).

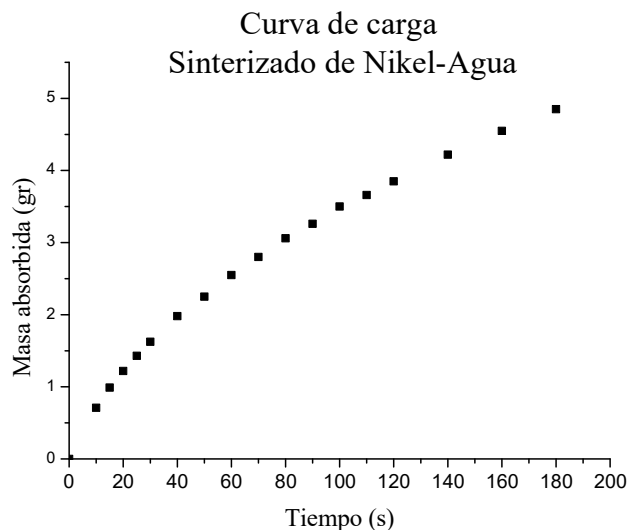


Figure 3.8: Pumping curve for nickel powder sintering, 2.5µm diameter particles, 59% porosity, distilled water

If the height is used as the measuring parameter, a "Sony DCR-SR55E" video camera and the measurement scale (height reading) will be used; Annex 5.

From the experimental data of figure 3.7 an adjustment of the exponential type is made to obtain the curve in analytical form (13).

$$y = A_1 \left(1 - e^{\left(\frac{-t}{t_1} \right)} \right) + A_2 \left(1 - e^{\left(\frac{-t}{t_2} \right)} \right) \tag{13}$$

That for the case of Nickel-water is, figure 3.9:

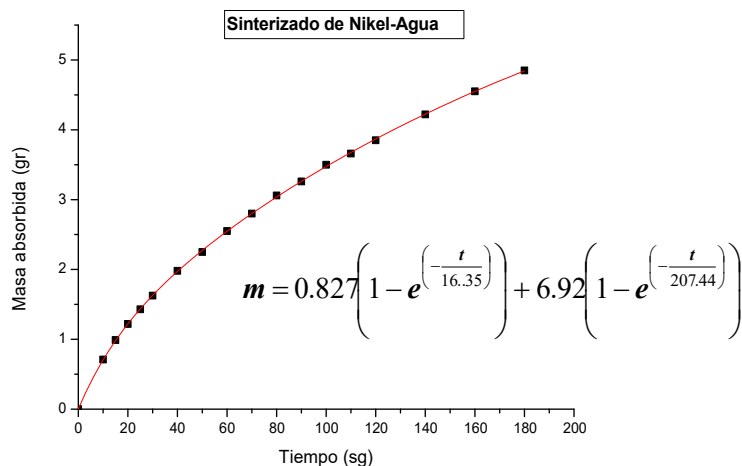


Figure 3.9: Nickel-water adjustment curve

3.2.3-Permeability

It is defined as permeability to the ability of a porous medium to circulate a fluid therethrough. Due to the complexity of the porous media internal configuration, there is no general relation that determines the value of " \mathcal{K} " as a function of the effective porosity (porosity, tortuosity). In spite of this, there are approaches that aim to simplify this internal structure to directly solve the N-S equations at pore level and obtain an expression for permeability. Among these approaches are: the one that resembles the porous medium to a set of micro-ducts [9, 10], or the one that represents it by a hydraulic radius. Thus for the latter approach one can find expressions for permeability as a function of porosity such as the Carman-Kozeny equation for spherical particle beds:

$$\mathcal{K} = \frac{d^2 \varepsilon^3}{180(1 - \varepsilon)^2}. \quad (14)$$

Being its more general form:

$$\mathcal{K} = \frac{\varepsilon^3}{\mathcal{K}_k (1 - \varepsilon)^2 A_0^2} \quad (15)$$

Where

" $A_0=A_{fs}/V_s$ " specific surface,

A_{fs} : solid wetted surface

V_s : volume of solid

" $\mathcal{K}_k=\mathcal{K}_0\tau$ " Kozeny constant

\mathcal{K}_0 : Numerical value according to the cross-sectional shape of the duct (2 for circular and between 2-2.5 for rectangular, elliptical, annular ...)

τ : Tortuosity

and " ε " porosity.

For the case of porous media in which the internal structure can resemble a bundle of straight tubes (longitudinally oriented fibers, structures created by SLM-3D printing) by directly applying NS to tube level (Hagen- Poiseville) the following expression is obtained for the permeability:

$$\mathbf{K} = \frac{d^2 \varepsilon}{32} \quad (16)$$

Where $\varepsilon = \frac{n\pi d^2}{4}$ is porosity, "n" number of tubes per unit area in cross section and "d" tube diameter.

In spite of the existence of these expressions, whose application is restricted to the range under which they were obtained, the experimental method is the most accurate in determining the permeability of a porous medium of complex internal structure. For this purpose, permeability measurement devices are used, such as that of figure 3.9, which allows indirect determination, comparison with Darcy [11, 12], of wick permeability by measuring the head loss " ΔP " and flow rate through the medium.

In the device of Figure 3.10, the fluid flows through the porous media by means of a pump placed in the "simple holder". A "differential pressure" sensor is located on both sides of the sample to measure the head loss when passing through the porous medium. The device has a by-pass that ensures low flow control through the medium. This is because the pump is not able to supply low flow rates. The two flow meters placed in the by-pass allow to determine the low flow rate flowing through the sample. As shown in the figure, it is a closed circuit with a reservoir from which the fluid is aspirated and returned after the stroke. This reservoir also has an air chamber that absorbs any pressure variation.

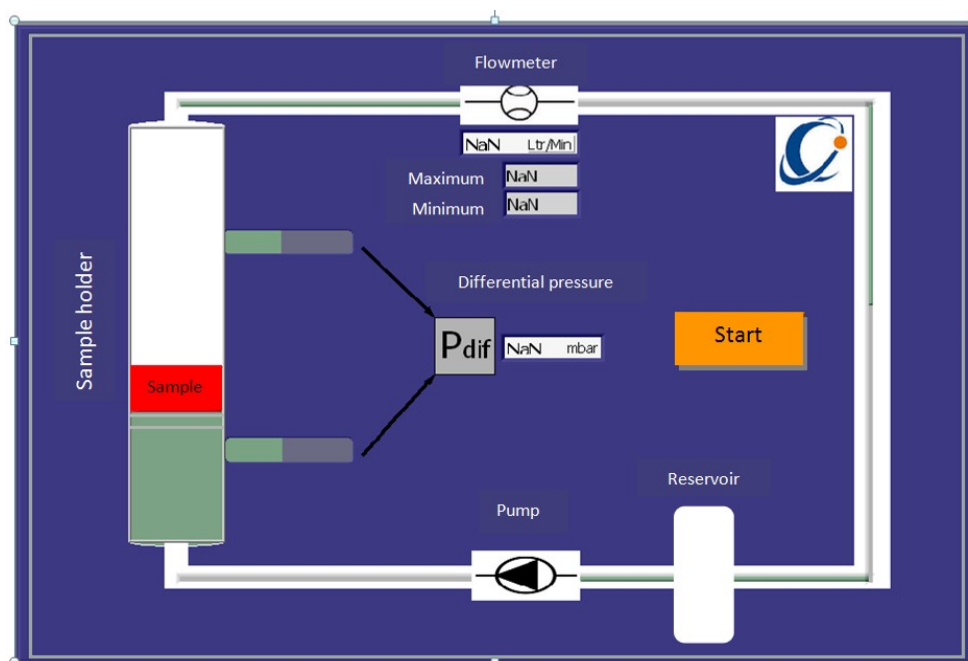
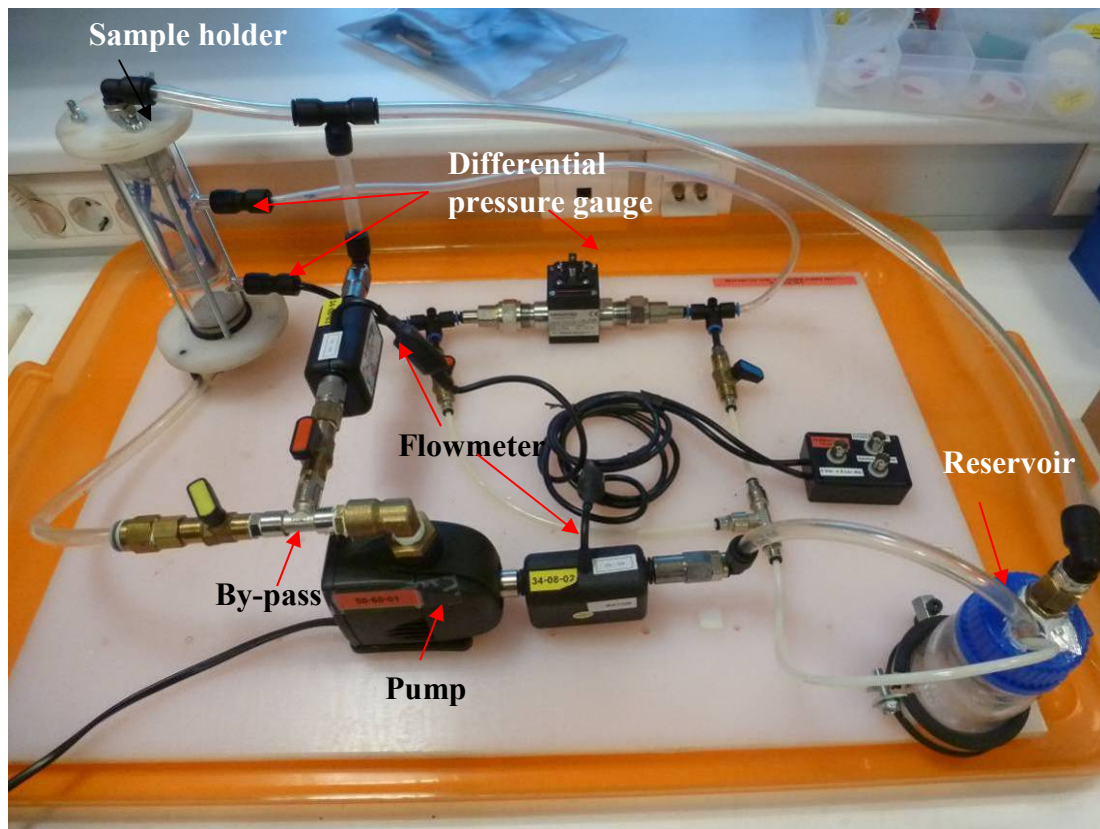


Figure 3.10: Porous media permeability equipment.

At the start of a permeability measurement a pressure-flow measurement is performed for a wide flow sweep. The purpose of this is to determine the flow rate from which the P-Q curve takes a quadratic form, **limit flow rate**. Once this is detected, another battery of P-Q

measurements is performed for a flow range lower than the limit flow rate in which the curve presents a linear behavior that is what is sought to later **determine the permeability** of the porous medium. For example, in the case of a ceramic foam of 30 ppi (pores per inch) and water, a limit value of 0.85 g/s (0.0012 m/s) is obtained below which the pressure loss has a linear behaviour, figure 3.11.

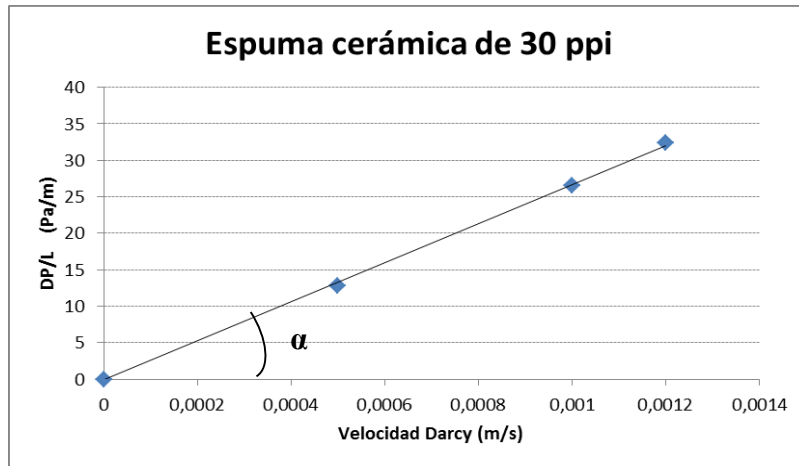


Figure 3.11: Linear relation of pressure loss with temperature (Darcy law)

For this flow rate the value of the Reynolds number at pore level "Rep" is 9.17 which is less than 10, being 10 the limit above which Darcy's law is not applicable [13-15] (Rep <1 Darcy regime; 1 <Rep <10 can be Darcy regime; Rep > 10 is not Darcy). Although this classification of the type of regime is accepted by the scientific community it must be said that it is not always fulfilled, it may happen that in low flow regimes, Rep <1, Darcy's law is not satisfied. This non-compliance is more likely to small than large pore sizes because of higher frictional forces.

The slope of curve 3.11 determines the permeability of the porous medium.

$$\text{tg}(\alpha) = \frac{\Delta P}{L} = \frac{\mu}{K}, \dots, K = \frac{\mu}{\text{tg}(\alpha)} = 5.01 \cdot 10^{-8} \text{ m}^2 \quad (17)$$

3.3. Experimental characterization

3.3.1- Loading curve

Apart from the characterization of the Nickel powder sintering, shown in section 3.2.2, other powder sintering materials are characterized: "Alugram SIL G and Alugram Nano-SIL G" silica gel sheets, copper powder; Stainless steel mesh and 3D printing-SLM stainless steel; **Annex 5**.

- *Sinterized powder "Silica Gel Sheets"*. Two types of commercial silica gel films used for flat chromatography are analyzed, the characteristics of which are shown in Table 3.1.

Table 3.1. Properties of Silica gel sheets

	Material	Powder size
Láminas de Silica Gel	Alugram SIL G	5-17 μm
	Alugram Nano-SIL G	2-10 μm

Following the procedure and equipment described in section 3.2, the silicone sheets loading curves are obtained for two fluids: water and methanol, figure 3.12.

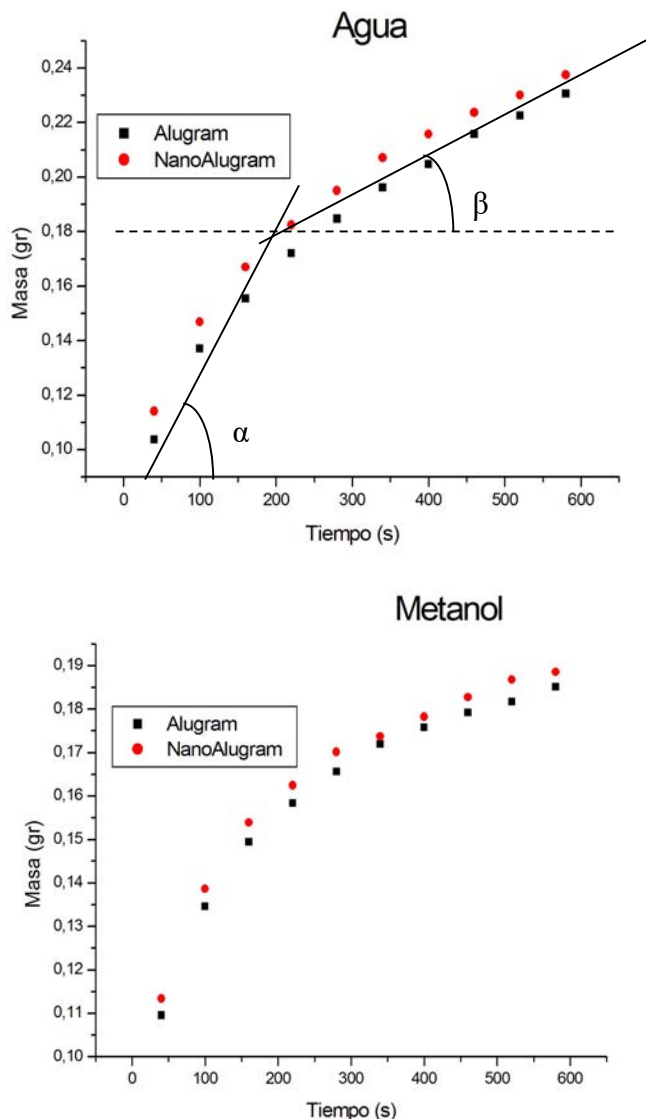
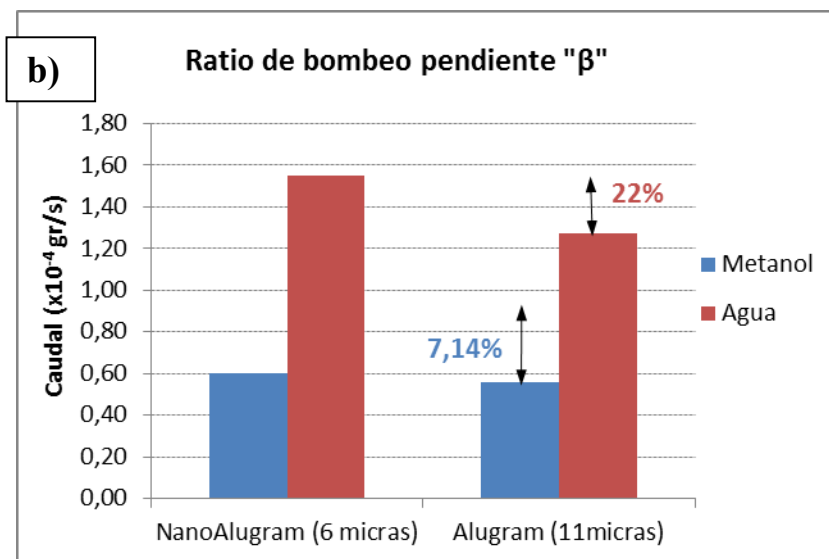
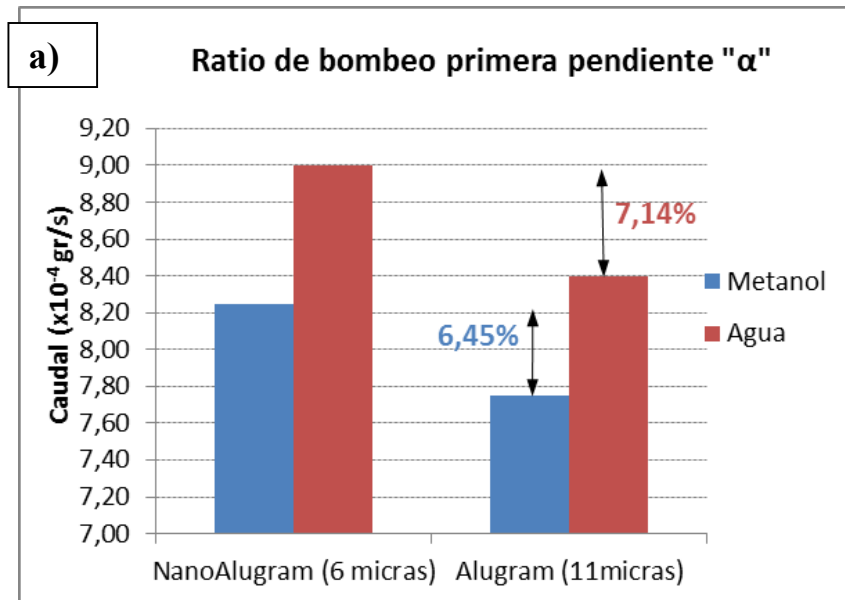


Figure 3.12: Differences between the two types of silica gel using two different liquids: water and methanol

The experimental result shown in Figure 3.12 confirms a bi-exponential behavior for the loading curve of the silica gel sheets. It is also shown that the pumping capacity ($\text{gr} / \text{s} \approx \alpha$) of the smaller powder size film (NanoAlugram $6\mu\text{m}$) is higher than that corresponding to a larger dust size (Alugram $11\mu\text{m}$), 9 versus 8, 40 for Water and 8.25 versus 7.75 for Methanol, figure 3.13 a). The percentage of pumping capacity improvement due to a smaller size of powder (pore) results to be of 7.14% and 6.45% for Water and Methanol respectively.

In the second part of the curve, the " β " slope is also smaller the larger the powder size (pore), Figure 3.13b).

For a powder size of 6 μm , the loading curve slope decrease (α - β) results from 82.78% for the case of Water and 92.73% for Methanol, figure 3.13c).



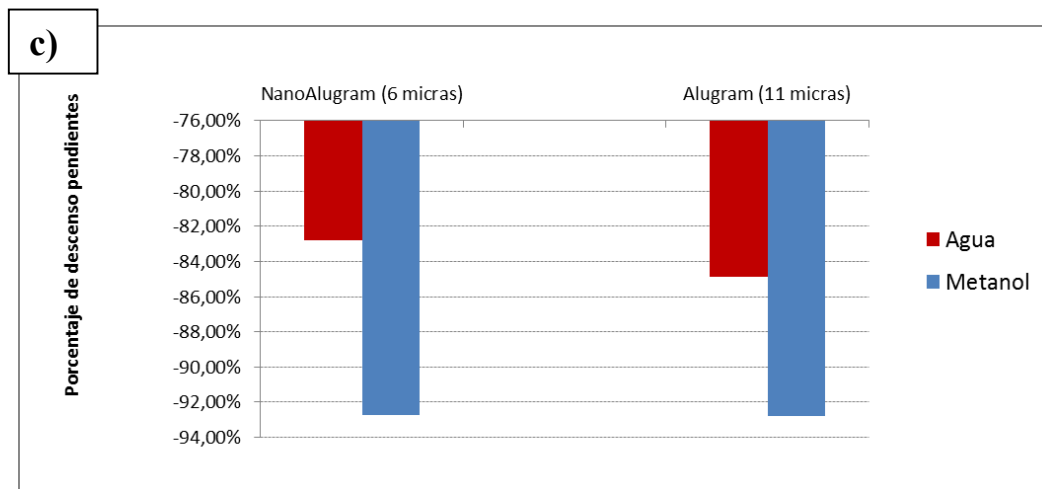


Figure 3.13: a) forward slope " α "; b) forward slope " β "; c) percentage of descent of slope " α " with respect to slope " β ".

➤ *Stainless steel wire mesh.*

Regarding meshes, AISI 304 stainless steel meshes are considered and their characteristics are shown in Table 3.2, figure 3.14.

Table 3.2. Metallic mesh characteristics

Tela	d (diam. alambre) mm	w (espaciado) mm	ϵ (porosidad)
60	0.024-0.027	0.06	0.4756
200	0.072-0.078	0.15-0.16	0.4519
300	0.17	0.3	0.4074

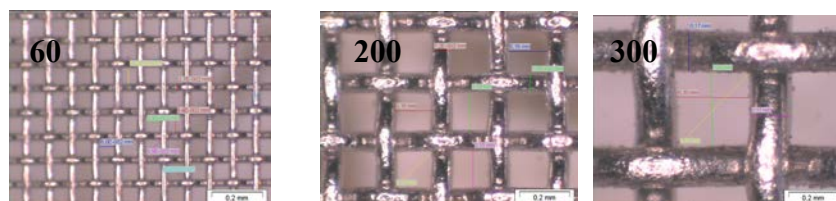


Figure 3.14: Detail of 60µm mesh, 160µm and 300µm pitch

The samples for the mesh-Methanol loading curve measurement were obtained by forming ring cylinders of 10 mm inner diameter and 5 layers of coiled mesh, figure 3.15. A sample for each type of mesh: 60, 200, 300 µm pitch.



Figure 3.15: Mesh Sample

After tests, results look like those plotted in figure 3.16.

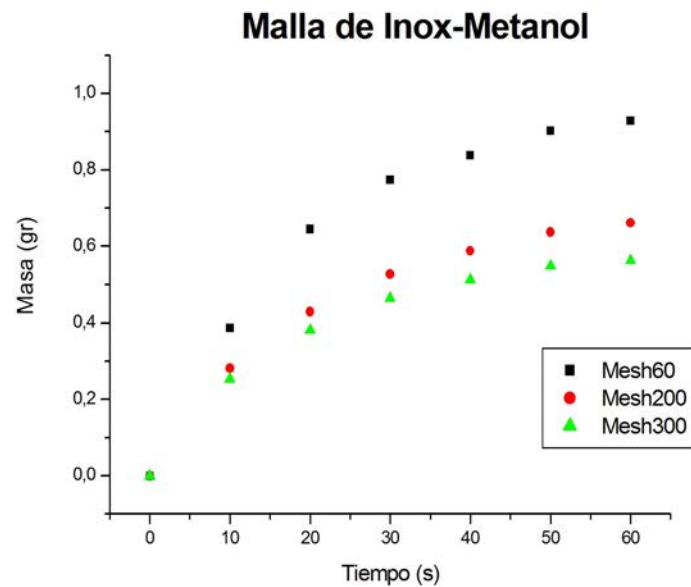


Figure 3.16: Pumping curve for stainless steel mesh of different pitch: 60, 200 and 300

The above figure confirms the bi-exponential shape of the load curves as well as that the finer the mesh (mesh 60) the greater the capillary pumping capacity. At the end of the recording time (60sg) the total mass absorbed by the mesh is greater for small pitch than for larger pitch, fig. 3.17.

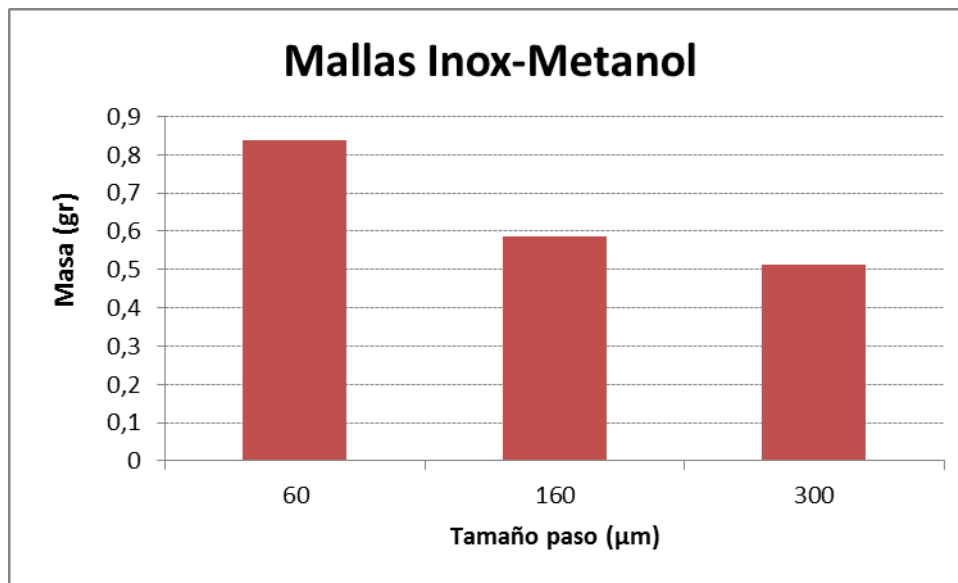


Figure 3.17: Drop the absorbed mass to increase pitch size

➤ *Copper powder sintering.*

In this case tests were carried out for different sintering samples of copper dust as porous material and methanol as liquid. The objective is to determine the effect of pore size on the porous media loading curve as well as confirm its shape.

For this purpose, various samples of copper powder sintering with different pore sizes (powder size) have been created. The denomination of the samples is shown in table 3.3.

Table 3.3. Characteristics of sintered powder copper samples

Muestra	ϵ (porosidad)	D (Tamaño poro medio “ μm ”)
1	0.573	30
2	0.573	60
3	0.573	95
4	0.56	130

The results are shown in figure 3.18 and 3.19.

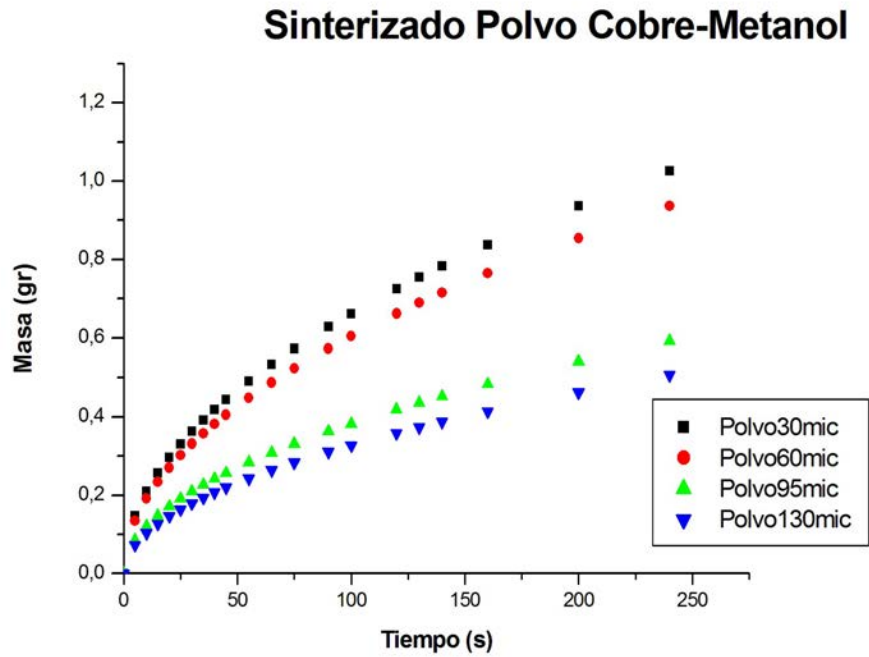


Figure 3.18: Pumping curve for copper powder sintering

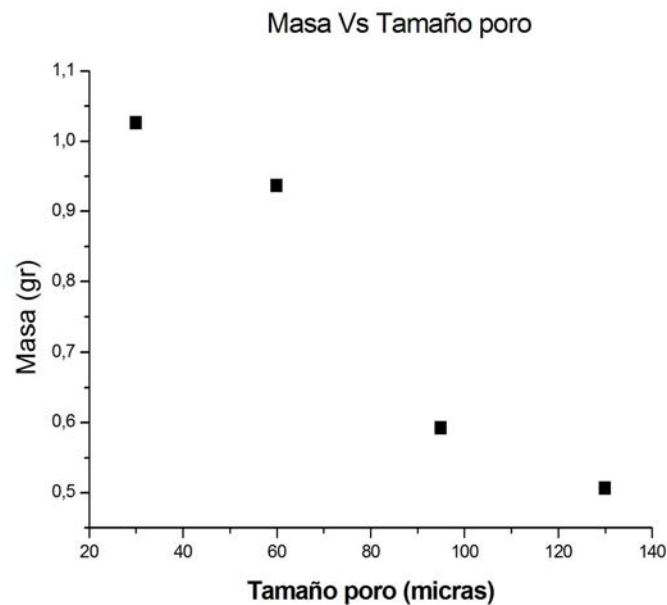


Figure 3.19: Drop the absorbed mass to increase pore size

➤ *Escaffol 3D laser printing SLM.*

By means of the SLM technique two porous samples were developed. Both with a fine control of the pores connections. This technique offers an absolute control over the pore size or capillary radius, as well as the tortuosity of the matrix. In this case the configuration is as if there were

capillary conduits arranged parallel to each other. This arrangement reduces the tortuosity of the medium which a priori would favour the pumping capacity. Two samples are constructed: fine, "90 μm capillary radius", and thick, "180 μm capillary radius", figure 3.20, whose porosity is 30% and 45% respectively.

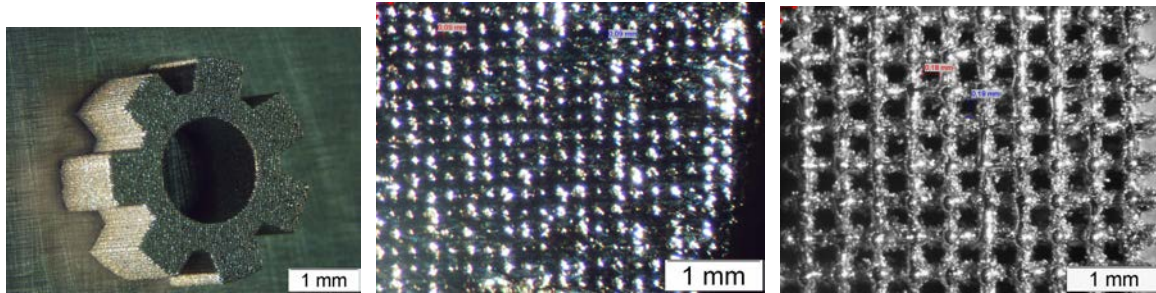


Figure 3.20: a) form of the scaffold; b) fine capillary, 90 μm ; c) thick capillary, 180 μm

The scaffold material is stainless steel and methanol as working fluid. The loading tests are carried out with the following results, figure 3.21.

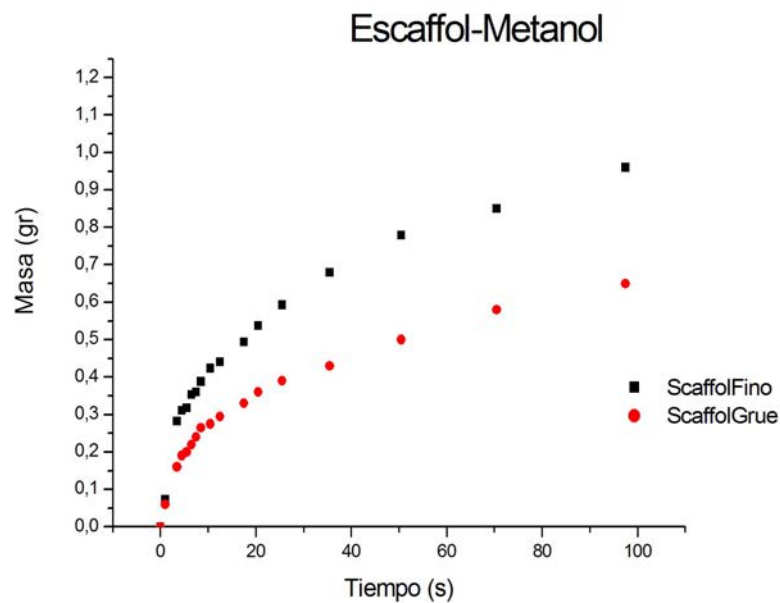


Figure 3.21: Pumping curve for scaffold of stainless steel and methanol for two sizes of capillary

As in previous cases to lower capillary radius, greater pumping capacity. The curve shows the expected bi-exponential behavior. A very high absorption rate is observed for both cases in the first instants of the pump, which is positive for the final application.

Analysis of the results "loading curve".

- A first conclusion of the load curve analysis is that regardless of the method of manufacturing the porous medium or wick the smaller the pore size the greater its pumping capacity.
- The most used technique in wick manufacture for two-phase, capillary pumping devices is the powder sintering. Basically because of its low manufacturing cost and good performance. Considering the slopes of the height vs time loading curves the result is that of figure 3.22.

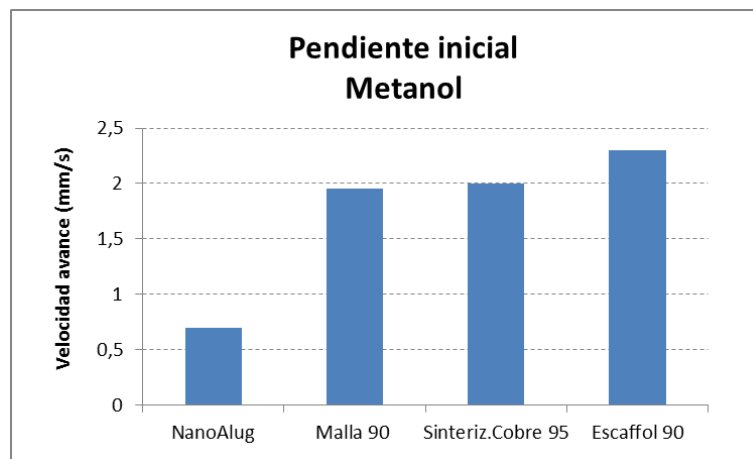


Figure 3.22: SLM compared to sintering for a similar pore size

As can be seen, apart from the influence of the wettability, the scaffold presents a higher advance speed than others techniques, specifically compared with that of copper sintering. This demonstrates the SLM technique goodness to create porous media for two-phase devices. On the other hand, there would be the porous media tortuosity which will be discussed below.

3.3.2- Permeability

In this section we intend to experimentally determine the effect of pore size and porosity on the permeability of the medium, as well as the internal structure or tortuosity. For this, samples of different pore sizes are tested and constructed with different techniques such as sintering, 3D printing "SLM", foam.

A scanning electron microscope "JEOL-JSM5900LV" was used to determine the pore size, while the porosity was determined by measuring the size and weight of the samples.

➤ *Foams*

Four samples of 30, 40, 50 and 80 ppi (pores per inch) ceramic foams were analyzed, each with the pore size and porosity characteristics collected in Table 3.4 and a thickness of 50 mm.

Table 3.4: Pore size and porosity of 30, 40, 50 and 80 ppi foams.

Espuma tipo (ppi)	Tamaño poro (μm)	Porosidad
30	972	0.89
40	705	0.886
50	632	0.863
80	392	0.858

With the equipment shown in Figure 3.9, water flow tests are carried out at low speeds (0-0.0012 m/s) in order to obtain the Darcy curve from which to obtain the foam permeability, figure 3.23.

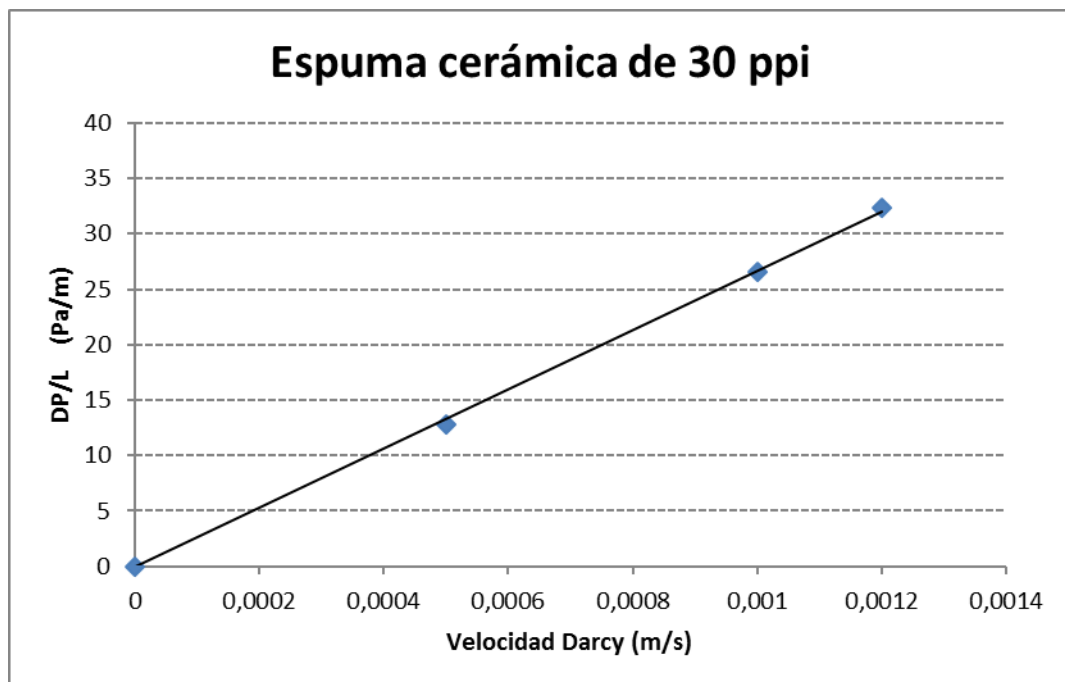


Figure 3.23: Darcy law for a 30ppi ceramic foam structure and water.

As mentioned in section 3.2.3, the permeability is obtained from the loading curve slope. The same procedure is performed for each of the remaining samples whose permeability is plotted in Figure 3.24.

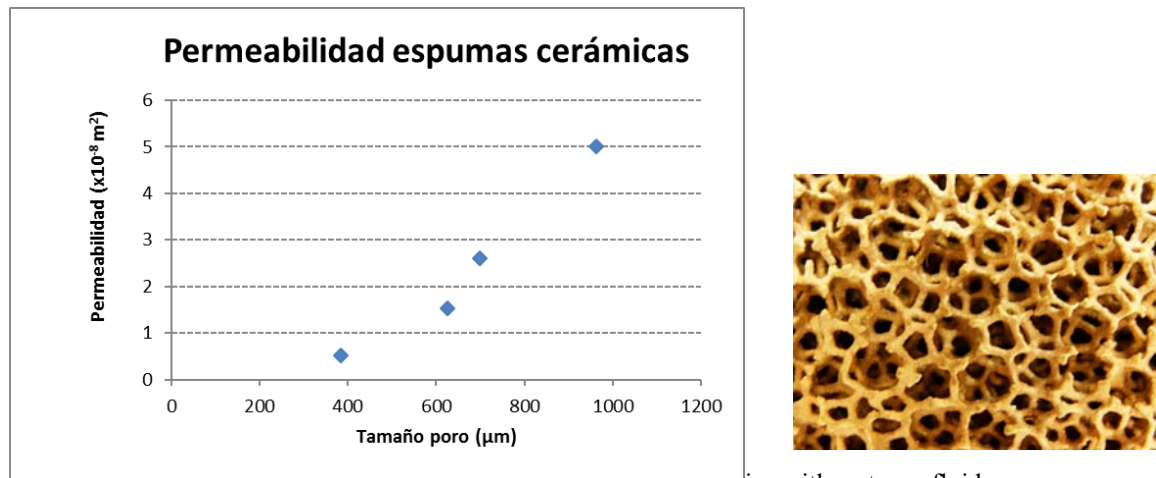


Figure 3.24: Permeability as function of pore size with water as fluid.

As shown, the permeability presents an upward linear behavior with pore size, the larger the pore size the greater the permeability [16-19].

➤ *Sintered*

It is analysed the permeability curve versus pore size for the case of Copper powder sintering. For this purpose, samples of Copper powder sintering with the same characteristics as those used in obtaining the loading curve, section 3.3.1, are considered. First, the Darcy curve for each sample is obtained as a function of the flow rate. Figure 3.25 shows the one corresponding to the pore size of 95µm. The fluid used is water.

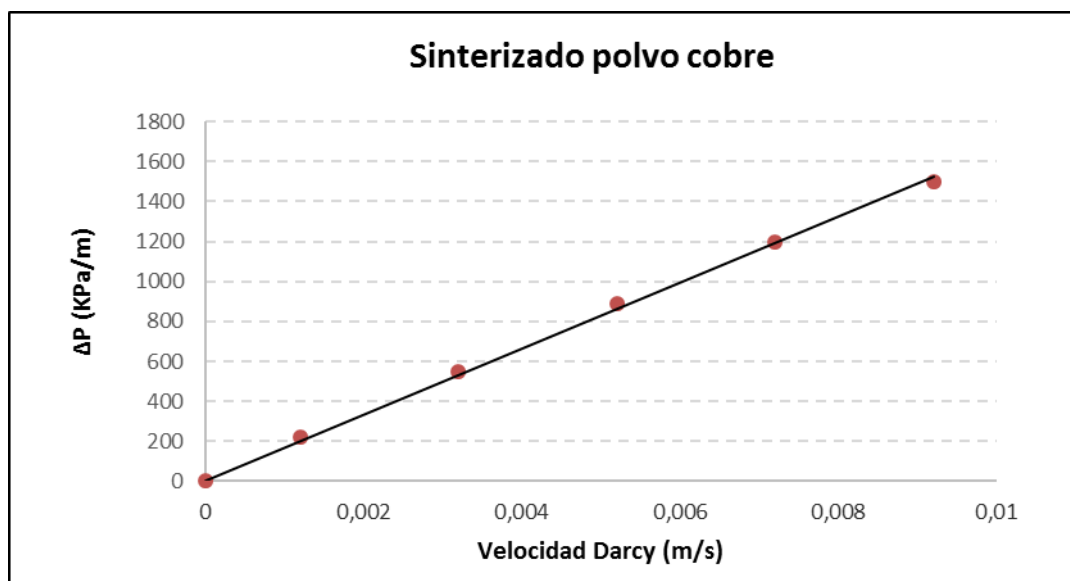


Figure 3.25: Darcy law for a 95µm pore size copper sintering;

From these curves the permeability of each of the samples are obtained, figure 3.26.

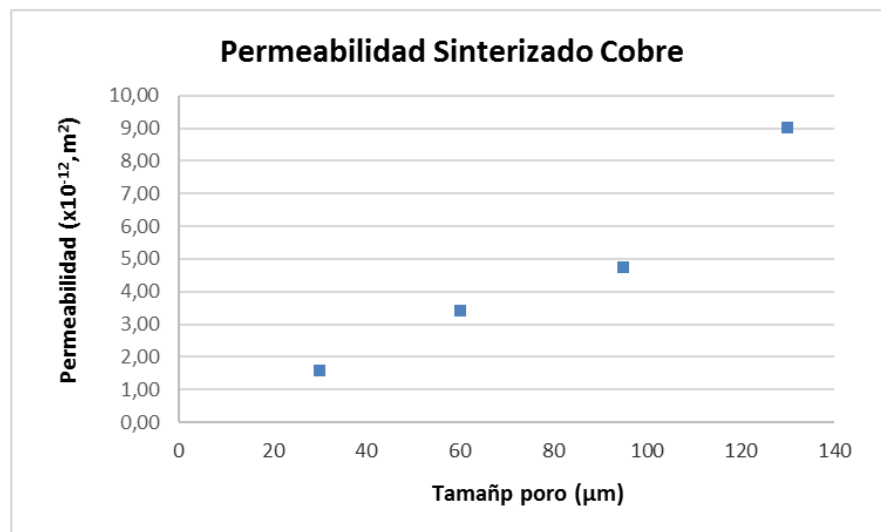


Figure 3.26: Permeability versus pore size in a copper powder sintering, water as fluid

As can be seen from Figure 3.25, the larger the pore size the greater the permeability. Also this growth proves to be linear with the pore size.

➤ *3D Printing, "SLM"*

The same scaffold samples used in the loading curve determination are taken and the same procedure as that for permeability is followed. In this case the flow rate, Darcy regime, employed is (0-0.01 m / s) with water as working fluid, figure 3.27.

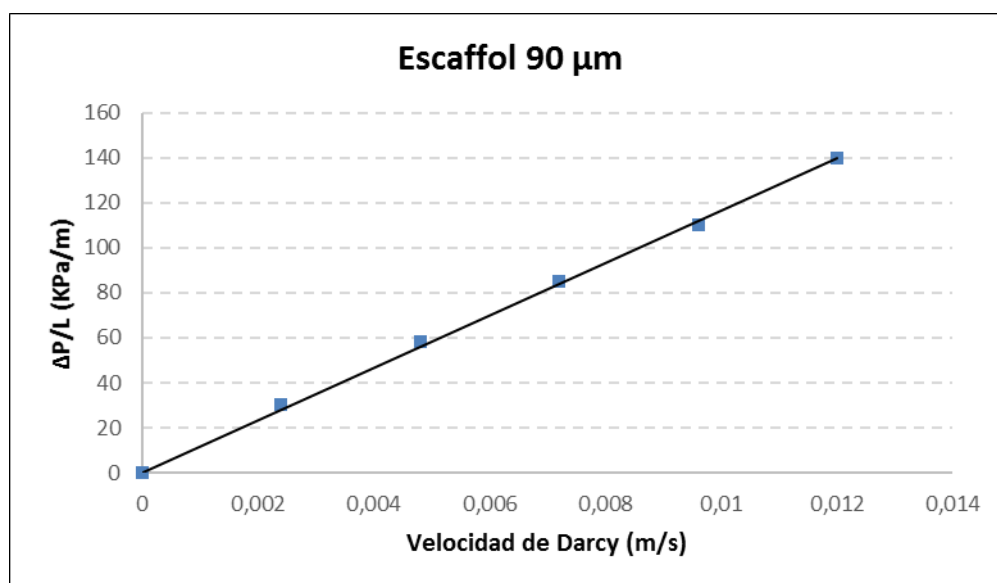


Figure 3.27: Darcy law for a SLM scaffold of 90µm capillary;

Carrying out the same process for three different diameters, Figure 3.28 shows the effect of capillary size on permeability.

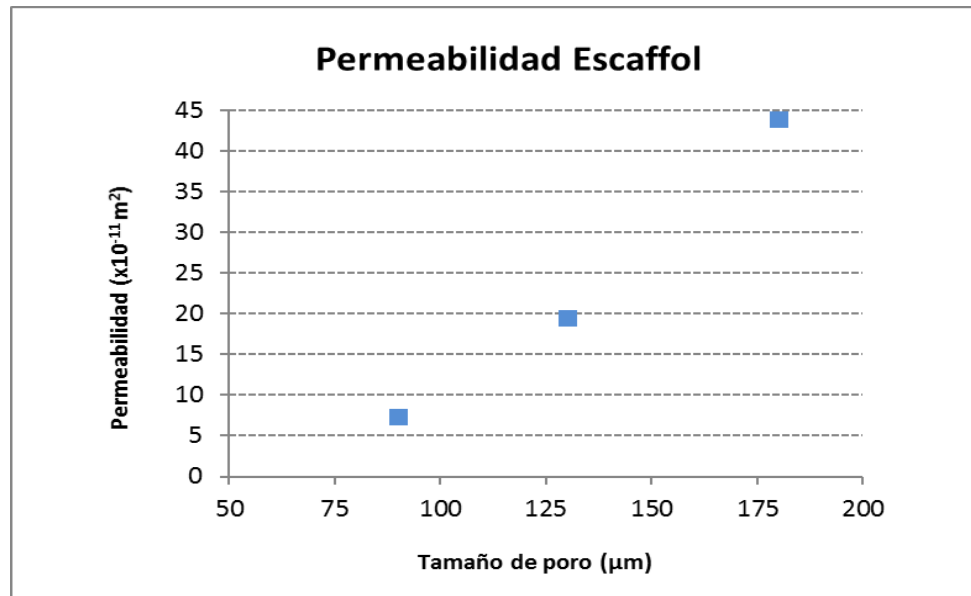


Figure 3.28: Permeability versus capillary size of the Escaffol-SLM, water as fluid

As expected the permeability increases linearly with pore size..

Analysis of the results "permeability"

- The permeability increases with pore size regardless of the technology used to manufacture the porous medium.
- At equal 90 µm pore size, it results that the SLM has a permeability of 1.16×10^{-10} versus 5.62×10^{-10} of the ceramic foam and 4.9×10^{-12} copper sintering, figure 3.29. Although the permeability of the escaffol is lower than that of the foam and two orders of magnitude higher than that of the copper sintering, it must be said that the scaffold porosity (46%) is lower than that of the foam (80%) and the sintering (57%). Another issue revealed in this comparison is the pores arrangement inside the porous media , the so called tortuosity, which is defined as the path the fluid travels through the medium from the entrance to the outlet. Intuitively, the more complex this pathway is, the lower the permeability [20, 21]. This is clearly observed when comparing the permeability of the powder sintering and the escaffol which is two orders of magnitude higher than that of the powder sintering for equal pore size and porosity.

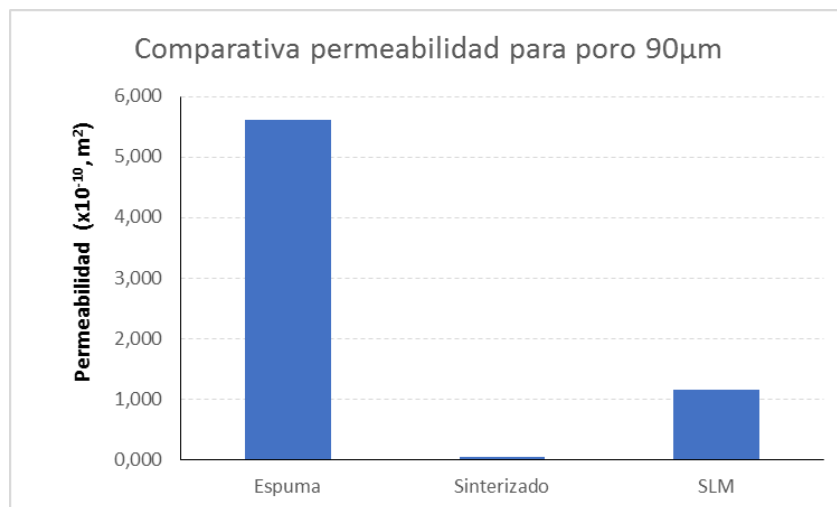


Figure 3.29: Comparison of permeabilities for an identical pore size of approximately 90µm

- At equal porosity, around 60%, the scaffold permeability (9.1×10^{-10}) is slightly superior to the ceramic foam (8.4×10^{-10}) and well above that of the copper powder sintering (4.9×10^{-12}), figure 3.30. In this case both foam and scaffold have a similar pore size, around 200µm, while the sintering is 90µm.

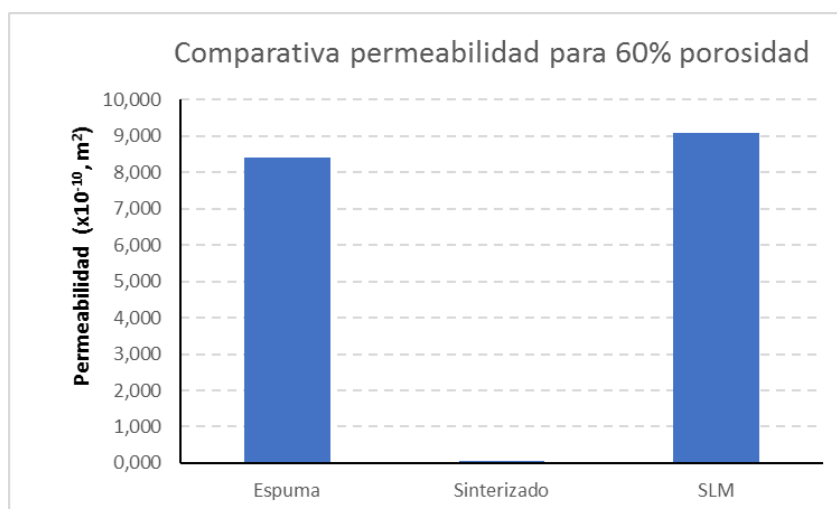


Figure 3.30: Comparison of permeabilities for an identical porosity 60%

Bibliography

- [1] J.B. Zeng, C.P. Wu, P.M. Qiu, Loose powder sintering of porous titanium plate, *Powder Metall. Technol.* 10 (1992) 282–286.
- [2] J.M. Ruan, P.Y. Huang, *Powder Sintering Theory*, China Machine Press, Beijing, 1996. 252–272.
- [3] X. Kang, H. Tang, J. Wang, Effect of pressing pressure on performance of Fe₁₆Al₂Cr porous materials, *Rare Met. (Engl. Ed.)* 40 (2011) 1732–1736.
- [4] Marcelo Lago, Mariela Araujo. “Capillary Rise in Porous Media”. *Journal of Colloid and Interface Science* 234, 35–43 (2001)
- [5] Yong Tang, Daxiang Deng, Guanghan Huang, Zhenping Wan, Longsheng Lu. “Effect of fabrication parameters on capillary performance of composite wicks for two-phase heat transfer devices”. *Energy Conversion and Management*, 66, 2013. Pages 66-76.
- [6] Dezhi Wang, Xiaoving Wang,.... “Influence of packing density of porous media for LHP”. *Powder technology*, Volume 258, May 2014, pg. 6-10
- [7] Jinwang Li, Yong Zou, Lin Cheng. “Experimental study on capillary pumping performance of porous wicks for loop heat pipe”. *Experimental Thermal and Fluid Science* 34, 2010. Pages 1403–1408
- [8] J.W. Li, Y. Zou, L. Cheng. “Effect of fabricating parameters on properties of sintered porous wicks for loop heat pipe”. *Powder Technol.* 204, 2010,. Pages 241–248.
- [9] Ram Ranjana, Jayathi Y. Murthya, Suresh V. Garimellaa, Unnikrishnan Vadakkan. “A numerical model for transport in flat heat pipes considering wick microstructure effects”. *International Journal of Heat and Mass Transfer*, Volume 54, Issues 1–3, 15 January 2011, Pages 153–168.
- [10] M.Kaviany. “Principles of heat transfer in porous media”. Springer, second edition. ISBN 0387945504.

- [11] J. Esarte, J.M. Blanco, A. Bernardini, J.T. San-José. “Optimizing the design of a two-phase cooling system loop heat pipe: Wick manufacturing with the 3D selective laser melting printing technique and prototype testing”. *Applied Thermal Engineering* 111 (2017) 407–419.
- [12] Wojciech Sobieski, Anna Trykozko. “Darcy’s and Forchheimer’s laws in practice. Part 1. The experiment”. *Technical Sciences* 17(4), 2014, 321–335
- [13] Alabi, O. O. “Validity of Darcy’s Law in Laminar Regime”. *EJGE*, Vol. 16, 2011.
- [14] G. S. Beavers and E. M. Sparrow. “Non-Darcy Flow Through Fibrous Porous Media”. *J. Applied Mechanics*, Volume 36, issue 4, 711-714, Diciembre, 1969.
- [15] Fahd Siddiqui, Mohamed Y Soliman, Waylon House and Akif Ibragimov. “Pre-Darcy Flow Revisited under Experimental Investigation”. *Petroleum & Environmental Biotechnology*, Volume 6, Issue 6.
- [16] Fang-Chou Lin, Bing-Han Liu, Chun-Chia Juan, Yau-Ming Chen. “Effect of pore size distribution in bi-dispersed wick on heat transfer in a loop heat pipe”. *Heat and Mass Transfer*. August 2011, 47:933
- [17] Daxiang Deng, Yong Tang, Guanghan Huang, Longsheng Lu, Dong Yuan. “Characterization of capillary performance of composite wicks for two-phase heat transfer devices”. *International Journal of Heat and Mass Transfer* 56 (2013) 283–293
- [18] P.L. Yu, F.X. Yin, Z.F. Wu. “Effect of apparent density of powder and shape of the particle on preparation and properties of sintered stainless steel porous material”. *Powder Metal Technol.* 30, 2012, Pages 177–181
- [19] Tadej Semenic, Ying-Yu Lin, Ivan Catton. “Thermophysical Properties of Bi-porous Heat Pipe Evaporator”. *Journal of Heat Transfer*, 2008, Vol. 130.

- [20] Carl Fredrik Berg. “Permeability Description by Characteristic Length, Tortuosity, Constriction and Porosity”. *Transport in porous media*, Vol. 103, 3, 2014. Páginas: 381-400
- [21] Guo, P. “Dependency of tortuosity and permeability of porous media on directional distribution of pore voids”. *Transport in Porous Media*, Vol. 95(2), 2012, pag. 285–303.

Chapter 4. Development of a theoretical model of two-phase heatsink Loop Heat Pipe

4.1 Introduction	69
4.2 Model's Development.....	70
4.2.1- Brief description of the components:	72
4.2.2- Mathematical formulation	72
4.3 Results	84
4.3.1- Validation.	84
4.3.2- Effect of vapour line length and radius.	88
4.3.3- Effect of condensing temperature.....	89
4.4 Conclusions	93
Bibliography.....	95

4.1 Introduction

The electronic world, LED devices and thermoelectricity among others, technically evolve in a vertiginous way. This allows them to enter markets never before explored, what set new technological challenges. Thus, for example, miniaturization in electronics, light quality of LEDs [1-3], the thermoelectric efficiency, durability, etc., present a challenge in terms of heat management, that's to say, in terms of temperature control at components level. Traditional technologies, liquid cooling [4, 5] or air [6-8], in many applications are no longer valid because of their large volume. Nowadays market requires refrigeration technologies with smaller volume and equal or even higher performance than the traditional cooling systems.

Among these technologies are the so-called *Loop Heat Pipes*, "LHP". Two-phase capillary pumping devices similar to heat pipes [9, 10] but with the advantage that they can work equally well for any orientation with respect to gravity.

Over the last decade, LHPs have been intensively researched thanks to the interest they have aroused in the field of electronics cooling [11,12]. All this thanks to:

- they have a greater heat transport capacity for equal dimensions
- they have very low thermal resistance
- by its design, allow a huge variety of designs expanding the range of possible applications
- they perform efficiently for any orientation with respect to gravity.

As a consequence of the above, LHPs have aroused a great commercial interest. Nevertheless, due to their manufacturing complexity and difficult operation, there are very few technical information available in open literature (this remains within the developers know-how).

Developers of this type of devices have progressively evolved from the traditional "test & error" methodology to a simulation-based methodology. Simulation methodology based mainly on a stationary approach of the Navier-Stokes equations

(mass, momentum and energy conservation) [13-16]. These models have mainly worked on flat evaporators [17,18] as they better fulfil the electronics cooling requirements. However, as these devices application to other sectors progress, LED illumination, for example, heat source shapes vary from one application to other what requires other evaporator geometries, such as cylindrical [19, 20].

The stationary approach of this type of devices is an approach that simulates-predicts the LHP steady state operation (representative mode of 90% of the life cycle) but is not able to predict behaviour in situations such as: *transient effects (start-up, operating conditions changes) and effects of the presence of non-condensable gases - progressive condensation*. Effects that in some applications may be of great interest and that require a knowledge and simulation tools capable of addressing the complexity of the thermodynamic and hydraulic phenomenon that take place in the LHPs [21]. These transient models development is complex and requires a great thermodynamic and fluid-dynamic knowledge interesting to define or analyze the components behaviour rather than the LHP system as a whole. At full system level, transient models are very heavy, complex and of doubtful reliability, while the stationary ones are agile and reliable in their steady state operation prediction. As far as transient behaviour is concerned, there are complete models that predict changes in operating conditions and / or start-up [22]. However, steady state models are the most widespread for the LHP design since steady state behaviour represents 90% or more of such devices' operating time and therefore their design must be focused on optimizing such mode of operation. In this chapter we present a steady state model for the design of LHPs with flat evaporator in which the heat transfer towards the compensation chamber is not given by an external input, as current models, but is determined by the model itself.

4.2 Model's Development

This section describes the analytical model developed to predict the LHP's operation. It is a model that simulates the LHP steady state operating and determines the influence of certain parameters on the LHP's heat transfer capacity. Parameters such as:

- radius and length of steam pipe
- condensing temperature

- thickness and typology of the primary wick
- type of working fluid, type of material the wick is made of and container material
- dimensions of the heat source and its maximum permissible temperature

Figure 4.1 shows a LHP scheme, components and operation.

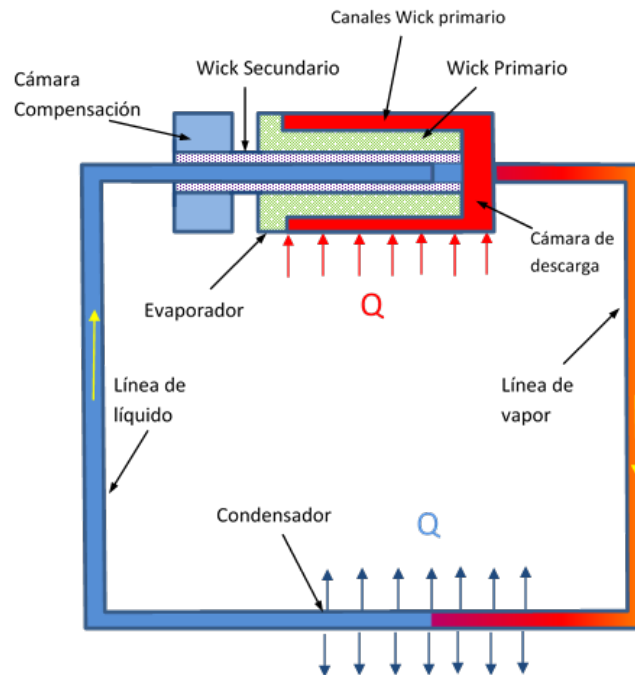


Figure 4.1: LHP diagram showing the constituent elements.

The operation of this type of devices is as follows. The refrigerant, which is inside the evaporator (low pressure and temperature), is pumped by capillarity through the primary wick to the outside of the evaporator. In this outer zone of the evaporator the heat generated by the component to be cooled (heat source) is absorbed. This causes the refrigerant to evaporate (high temperature and pressure) and accumulate in the discharge area of the evaporator before exiting the high temperature (red) vapor line. The steam flows through the vapor line until it reaches the condenser where heat is rejected to the environment causing the working fluid condensation (liquid state). From here, liquid flows through the liquid line until it enters again into the evaporator sine, passing previously through the compensation chamber. Through the secondary wick liquid is pumped from the compensation chamber into the evaporator sine when the return liquid does not satisfy the amount of liquid required for evaporation (changes in

heat loads). Liquid evaporates at the primary wick periphery and flows to the longitudinal channels disposed therein and from there towards the discharge chamber before exiting to vapor line.

4.2.1- Brief description of the components:

Usually, wicks are defined with the following criteria: primary wick with very fine pore sizes in order to increase the LHP pumping capacity and ensure refrigerant circulation; secondary wick with larger pore sizes in order to reduce the pressure losses induced by the passage of the refrigerant therethrough when liquid is supplied from the compensation chamber to the evaporator.

The compensation chamber has two fundamental functions: on one hand, to house the excess of refrigerant that could be produced in the device and on the other hand, to ensure a continuous supply of refrigerant to the evaporator [23].

The evaporator function is to absorb the heat generated by the source / component to be cooled by means of the refrigerant evaporation.

The condenser is responsible for expelling the heat absorbed to the environment by means of the refrigerant condensation.

The fact that the evaporator and the compensation chamber are physically joined through the secondary wick not only prevents hot spots from appearing on the primary wick but also ensures that the steam remains in the evaporator. The compensation chamber keeps at the saturation temperature corresponding to the pressure therein in which the liquid and gaseous phase coexist.

4.2.2- Mathematical formulation

This section presents the **steady state** N-S equations for each of the components constituting a LHP which define the mathematical expressions representing the LHP's operating mode. Given the general geometric characteristics of these devices, LHP, there are a number of assumptions that apply to conservation laws (mass, momentum, energy) without risk of error, these are::

- axial symmetry

- one-dimensional approach
- incompressible, viscous fluid

Despite the developments made on the mathematical models representing this kind of systems, there still exist a lack of understanding, at the analytical level, on how the different physical phenomena occurring in this type of devices take place. Thus for example micro LHPs present additional difficulties as a consequence of the treatment at micro-scale in which continuous media approach is questioned [24-26].

Energy balance:

In Figure 4.2, heat flows along the evaporator and condensation chamber are shown. It shows the heat load coming from the generation source " Q_L " which must be given as an input to the model.

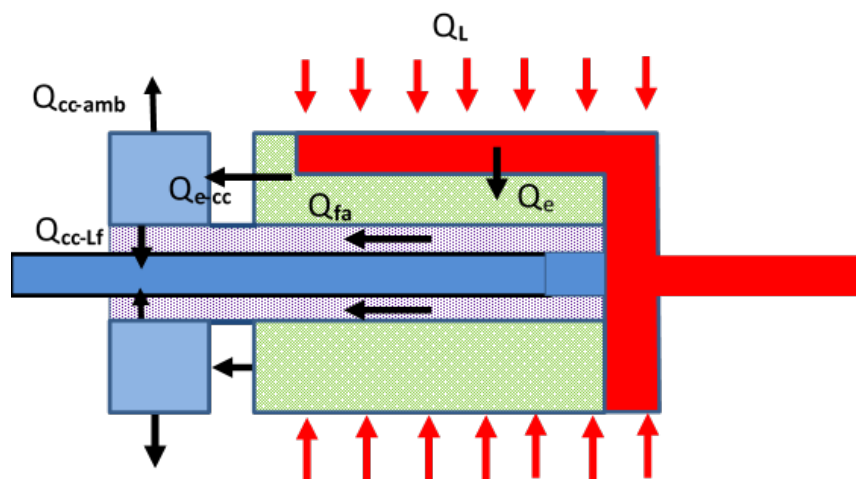


Figure 4.2: General heat flux directions.

Unlike a conventional LHP, there is no specific condensation zone. It occurs at some point along the vapor and liquid line. Therefore, there is not an specific energy balance in the condenser but along the circulation lines (vapor and liquid).

Evaporator-source

Not all heat load " Q_L " is absorbed by the evaporator [27,28], part of it flows through the evaporator housing towards the compensation chamber, " Q_{e-cc} ", another part is transmitted to the interior of the evaporator, " Q_e " and another part leaks to the environment. In our case, we assume that it is perfectly thermally insulated, so that this

thermal leakage to the environment is zero. The energy balance under these conditions is:

$$\dot{Q}_L = \dot{Q}_e + \dot{Q}_{e_cc} \quad (1)$$

Inside the evaporator, the incoming heat, "Q_e", is distributed as shown in figure 4.3.

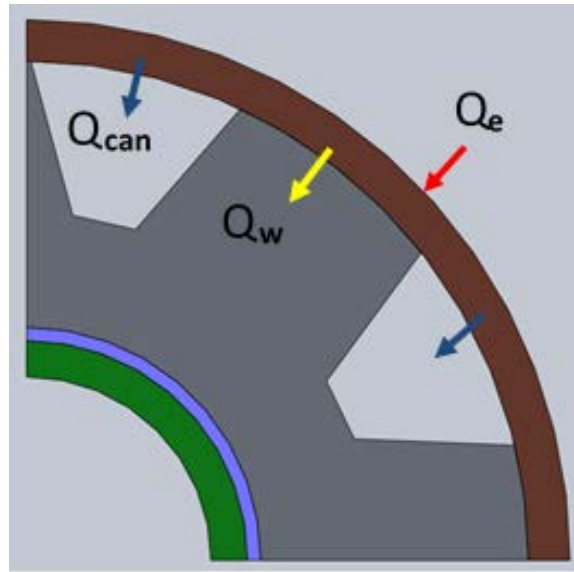


Figure 4.3: Heat flux through the evaporator.

Evaporator-primary wick

One part of the heat that enters the evaporator "Q_e" is transmitted to the steam in the primary wick channels "Q_{can}", and another part goes towards the primary wick "Q_w". Therefore:

$$\dot{Q}_e = \dot{Q}_w + \dot{Q}_{can} \quad (2)$$

Where:

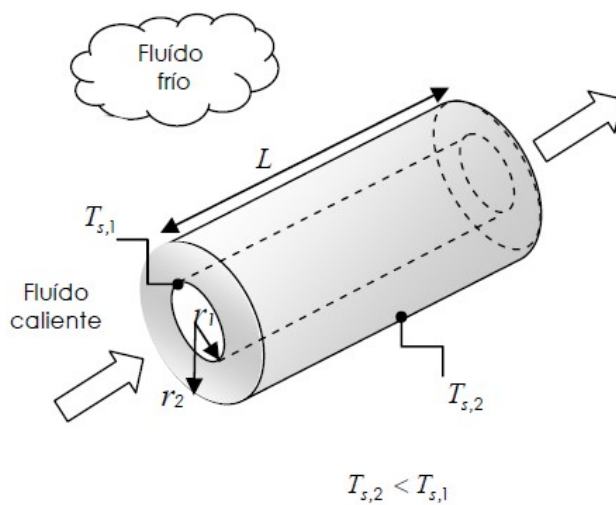
$$\dot{Q}_e = G_e(T_F - T_e); \quad \dot{Q}_{e_cc} = G_{e_cc}(T_e - T_{cc}); \quad \dot{Q}_w = G_w(T_e - T_{w1});$$

$$\dot{Q}_{can} = h_{can}A_{can}(T_e - T_{can})$$

Where "G_e" is the thermal conductance of the evaporator housing plus that of the evaporator-heat source contact, "G_{e_{cc}}" is the sum of the evaporator and compensation-

chamber housing thermal conductances. The coefficient " G_w " is the sum of the thermal conductance of the wick and that of the contact between wick and evaporator housing. Being a porous medium, its thermal conductance will be a weighting of the thermal conductance of the solid matrix and that of the liquid (**assuming a wick totally saturated of liquid**). " h_{can} " is the convective heat transfer coefficient on the channels walls and " A_{can} " is the corresponding heat transfer surface.

As a cylindrical arrangement the thermal conductance is defined as:



$$G_{s1,s2} = \frac{2\pi L\kappa}{Ln(r_2/r_1)}$$

" κ " permeabilidad del wick

Figure 4.4: Thermal conduction scheme.

Primary wick

The heat transferred to the primary wick " Q_w " is divided into three parts, one part is intended to evaporate liquid at the " Q_λ " interface, another part to heat the sub-cooling liquid entering the evaporator core from the line Liquid " Q_{sub} " and a third part flows through the secondary wick in the axial direction " Q_{fa} ". Energy balance at this component is:

$$\dot{Q}_w = \dot{Q}_\lambda + \dot{Q}_{sub} + \dot{Q}_{fa} \quad (3)$$

Where:

$$\begin{aligned}\dot{Q}_\lambda &= \lambda \dot{m}_v; & \dot{Q}_{sub} &= C_P \dot{m}_l (T_{v-l,w1} - T_{l,w1}); \\ \dot{Q}_{fu} &= G_{W2,CC} (T_{v-l,W1} - T_{v-l,CC}) \\ T_{w1} &= \frac{T_{v-l,w1} + T_{l,w1}}{2}\end{aligned}\quad (4)$$

Vapour channels

The steam trapped into the channels and coming from the liquid evaporation at the interface of the primary wick is reheated to the temperature corresponding to the pressure at the vapour line inlet (vapour reservoir). Thus, the energy balance in this element indicates:

$$\dot{Q}_{can} = C_P \dot{m}_v (T_{v,in} - T_{can}) \quad (5)$$

$$T_{can} = T_{v-l,w1} \quad (6)$$

Liquid and vapour lines

Since both lines have the same diameter "D" and the steady state is considered, the energy conservation equation for each of them is:

$$C_{Pv,in} \dot{m}_v T_{v,in} + P_{v,in} \frac{\dot{m}_v}{\rho_{v,in}} = C_{Pv,out} \dot{m}_v T_{v,out} + P_{v,out} \frac{\dot{m}_v}{\rho_{v,out}} + \dot{Q}_{v,perd} \quad (7)$$

$$C_{Pl,in} \dot{m}_l T_{sub} + P_{l,in} \frac{\dot{m}_l}{\rho_{l,in}} = C_{Pl,out} \dot{m}_l T_{Lf} + P_{l,out} \frac{\dot{m}_l}{\rho_{l,out}} + \dot{Q}_{l,perd} \quad (8)$$

Being "Q_{v, perd}" and "Q_{l, perd}" the heat losses along the vapor and liquid line respectively.

Compensation chamber

Saturation conditions are assumed inside the chamber, vapor and liquid coexist throughout the operation of the device. If we look at figure 4.2, the energy balance is as follows:

$$\dot{Q}_{e-cc} + \dot{Q}_{fa} = \dot{Q}_{cc_amb} + \dot{Q}_{cc_Lf}$$

The heat coming into the compensation chamber, " Q_{e_cc} and Q_{fa} " is equal to the heat being lost to the " Q_{cc_amb} " environment plus that which is inverted in preheating the subcooled liquid through the wall of the bayonet entering through the liquid line " Q_{cc_Lf} ". As the system is totally thermally insulated., $\dot{Q}_{cc_amb} = 0$.

$$\dot{Q}_{e-cc} + \dot{Q}_{fa} = \dot{Q}_{cc_Lf} \quad (9)$$

Where

$$\dot{Q}_{cc_Lf} = G_{cc_Lf} (T_{cc} - T_{Lf})$$

Condensing zone

As discussed above, in this device there is no specific zone of condensation but it occurs somewhere along the lines of vapor and liquid. Along these lines, the " Q_{out} " heat extraction is given by: the steam cooling " Q_{sv} " (sensitive heat), the condensation (change of phase) " Q_{λ} " and the liquid cooling (sensitive heat) " Q_{sub} ".

$$\dot{Q}_{out} = \dot{Q}_{Sv} + \dot{Q}_{\lambda} + \dot{Q}_{sub} \quad (10)$$

Being:

$$\dot{Q}_{\lambda} = \lambda \dot{m}_l; \quad \dot{Q}_{Sv} = C_{P,v} \dot{m}_v (T_{satPv} - T_c); \quad \dot{Q}_{sub} = C_{P,l} \dot{m}_l (T_c - T_{sub})$$

By making an energy balance to the whole LHP device, assuming that it is totally thermally insulated (except the source, and a section of the liquid and vapor line), the heat of the source coming into the evaporator " Q_e " has to be evacuated throughout the condensation " Q_{out} ".

$$\dot{Q}_{out} = \dot{Q}_e \quad (11)$$

Momentum balance:

Liquid, vapour lines.

This law establishes that the sum of forces on the control volume is equal to the variation of momentum. For the particular case of steady state:

$$\sum \vec{F} = \sum \vec{P} \cdot \vec{A} + \left(-\vec{F}_{int} \right) + \vec{G} = \dot{m} (\vec{V}_{salida} - \vec{V}_{entrada})$$

For the particular case that the entrance and exit have the same orientation and pipe is in horizontal position ($|V_{salida}| = |V_{entrada}|$) the momentum conservation along the stream line results in:

$(P \cdot A)_{salida} - (P \cdot A)_{entrada} = -F_{int} = -(F_{fric} + F_{AA'} + F_{Dir})$; "F_{int}" Is the sum of the viscous frictional forces along the tube "F_{fric}", the forces that cause the fluid to change direction "F_{Dir}" and the forces that are generated by passing the fluid through a narrowing or widening, "F_{AA'}". Clearing the cross-sectional area "A" of the above equation results:

$$(P)_{salida} - (P)_{entrada} = -\left(\frac{F_{fric} + F_{AA'} + F_{Dir}}{A} \right) \dots \Delta P = -(\Delta P_{fric} + \Delta P_{AA'} + \Delta P_{Dir})$$

This equation indicates that the total head loss in the duct is the sum of friction head losses and those due to direction and section changes.

$$\Delta P_{fric} = \tau \frac{\pi L D}{A}; \quad \Delta P_{Dir} = \kappa_{Dir} \frac{v^2}{2} \rho; \quad \Delta P_{AA'} = \kappa_{AA'} \frac{v^2}{2} \rho.$$

Being "D" pipe diameter, "A" pipe cross section, "L" pipe length, "τ" shear stresses on the pipe wall, "κ_{Dir}" the dimensionless coefficient of head loss due to flow direction change and "κ_{AA'}" the dimensionless coefficient of head loss due to cross section change.

In the case of friction head losses, by using the dimensionless loss parameter “f”

$f = \frac{8\tau}{\rho v^2}$, the Darcy-Weisbach equation for straight tubes is obtained:

$$\Delta P_{fric} = \frac{1}{2} \rho \frac{L}{D} u^2 \cdot f ;$$

Where “f” is:

For laminar regime: $f = \frac{64}{Re} ;$

For turbulent regime:

$$f = \frac{0.316}{Re^{0.25}} \quad Re < 10^5$$

ó

$$\frac{1}{\sqrt{f}} = -2 \cdot \log \left(\frac{Rug/D}{3.7} + \frac{5.74}{Re_D^{0.9}} \right) \quad (\text{Prabhata}); \text{ being “Rug”}$$

wall roughness

alternatively, the Moody diagram can be used directly
(diagram which is a function of Reynolds number and
roughness).

It follows that the loss of pressure in the duct (liquid and vapor line) is:

$$P_{v,in} - P_{sat,c} = \frac{\rho_v v_v^2}{2} \left(\frac{L_v}{D} f + k_{Dir} + k_{AA'} \right) = \frac{\rho_v v_v^2}{2} \sum k_i \quad (12)$$

$$P_{sat,c} - P_{l,out} = \frac{\rho_l v_l^2}{2} \left(\frac{L_l}{D} f + k_{Dir} + k_{AA'} \right) = \frac{\rho_l v_l^2}{2} \sum k_j \quad (13)$$

Evaporator.

Assuming: one-dimensional flow in radial direction, negligible mass forces and totally saturated wick, the momentum equation (11) is reduced to Darcy's law:

$$P_{v-l,l} - P_{l,out} = -(\Delta P_{fric})_l = -\frac{\mu_l R_w}{K} v_w = -\frac{\mu_l}{K} \frac{\dot{m}_l}{\rho_l 2\pi L_w} \quad (14)$$

Where " v_w " is the forward velocity through the primary wick, " R_w " the outer radius of the primary wick, " P_{interf} " liquid pressure at the meniscus interface, " $P_{l, out}$ " the liquid pressure in the evaporator core (equal to the liquid line inlet pressure) and " K " the wick's permeability [m^2].

On the other hand, the LHP's driving force is the capillary pressure, " ΔP_{cap} " which is generated in the " r_{eff} " meniscus of the primary wick. Pressure that must be greater than or equal to the head loss throughout the LHP circuit, " ΔP_{tot} ". Thus:

$$\Delta P_{tot} = (P_{v-l,v} - P_{v-l,l}) \leq \Delta P_{cap} = \frac{2\sigma}{r_{eff}} \quad (15)$$

$$\text{Being: } P_{v-l,v} = P_{v,in} \quad (16)$$

Condensing zone.

In the condensing zone, there coexist a two-phase fluid **homogeneous** (the velocities of the liquid and the gas are equal, there is no slip between phases) and in **equilibrium** (perfectly mixed having both phases equal temperature and pressure). This approach is almost always suitable for modelling an LHP (most of LHP applications), however, advanced models for two-phase flows can be used [29] in applications (exceptional cases) where the previous simplistic approach gives erroneous predictions. These are applications in which, for example: it is critical to determine the vapor fraction, it is necessary to know the transient movement of the liquid or when considering a non-equilibrium flow.

Momentum in the condensing zone, assuming annular condensation, is divided into three parts: the condensate film on the pipe's wall, the vapour in the pipe core and the interface between them [30, 31]. In the case of the present thesis a simple model is

proposed [32] in which the transition zone from vapor to liquid is not considered. This transition zone is included in the vapor line with the vapour properties for such fluid (in fact would be that of the mixture). However, their inclusion would require an equation of momentum along this transition (condensing) length " L_{cond} " given by:

$$P_{v,out} - P_{l,in} = \frac{1}{2} \frac{1}{A \rho_{mez}} \frac{L_{cond}}{D} \left(\dot{m} \right)^2 \cdot f$$

Where " ρ_{mez} and " \dot{m} " are density and mass flow of the two-phase mixture (liquid and vapor). Density is calculated by weighting the density values of each phase, the so called "title, x".

$$\frac{1}{\rho_{mez}} = \frac{x}{\rho_v} + \frac{(1-x)}{\rho_l};$$

Fluid title is obtained from the energy conservation equation in the condensing zone and that for the heat transfer whose coefficient of condensation is given by the following expression for turbulent flows $Re < 35000$:

$$h_c = 0,5554 \sqrt{\frac{\lambda g \rho_l^2 K_l^3}{\mu_l D (T_c - T_{mez})}}, \text{ being } T_{mez} \text{ the temperature of the mixture as it is}$$

condensing and T_c is the condensing temperature.

Nevertheless, this two-phase approach is left as an open line for future developments in this field.

As stated, transient length is some zone in the vapor line in which condensation interface is anchored at the vapour line outlet, Figure 4.5.

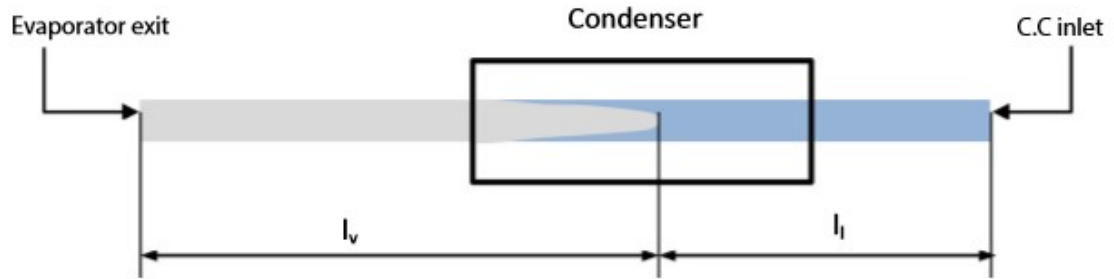


Figure 4.5: Condensing process.

The system of equations above is closed with the incorporation of the state equations as well as the Clausius Clapeyron equation that relates the pressure to temperature in a phase change process for a mono-component system like this. These relationships as well as the rest of the fluid properties (density, viscosity, specific heat, latent heat, etc.) are obtained from the *thermodynamic database* that the Engineering Equation Solver (EES) has got. This tool is also used to solve the system of equations that represents the LHP operation.

As far as the wick's conductivity is concerned, the following exponential equation is considered [33]:

$$K_{eff} = K_l \left(\frac{K_{matriz}}{K_l} \right)^{e^{0.53}}$$

It is also considered that:

$$P_e = P_{v,in} = P_{v-l,v} = P_{sat}(T_{v-l,w1}) \quad (17)$$

Being “ $P_{sat}(T_{v-l,w1})$ ” the saturation pressure corresponding to the temperature at the interface of the meniscus in the primary wick..

Mass balance:

$$\text{As steady state, it turns out that } \dot{m}_v = \dot{m}_l = \dot{m} \quad (18)$$

With all the above a set of equations (18) with its corresponding unknowns (pressures and temperatures) is obtained. As input data are: Q_L , T_F , T_c , LHP geometry, fluid type.

Such set of equations is introduced into the EES solver which runs the calculus following an iterative calculation algorithm, figure 4.6.

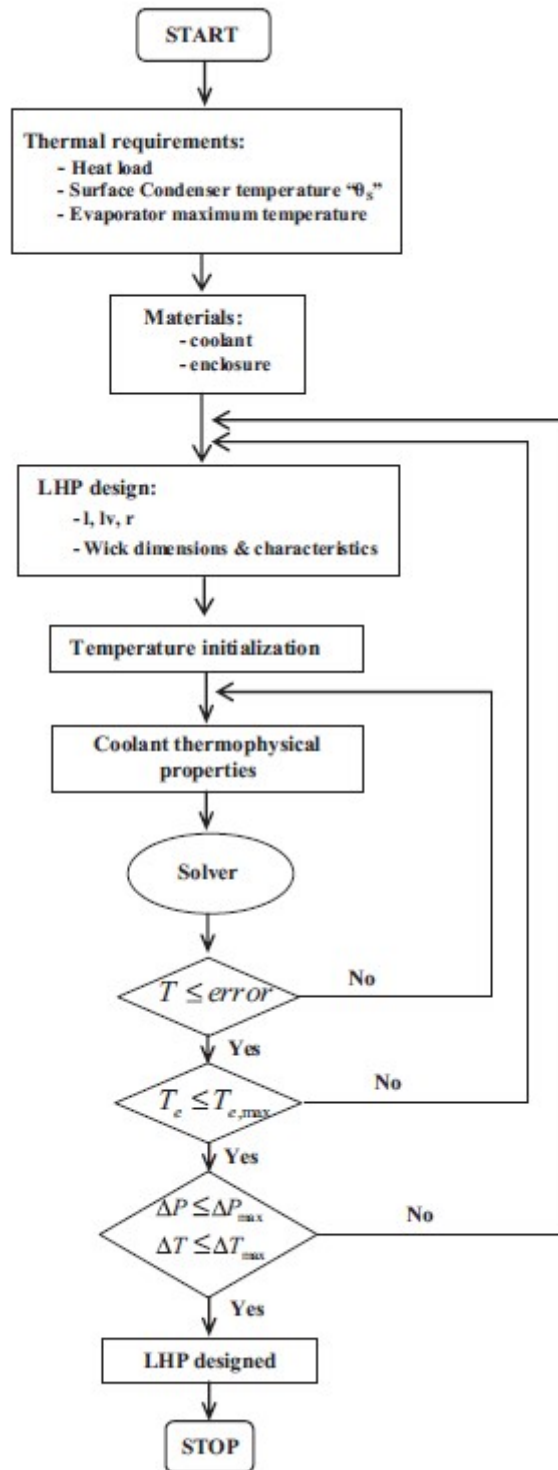


Figure 4.6: Algorithm of calculation.

4.3 Results

4.3.1- Validation.

This mathematical model with its corresponding iterative algorithm is run for a specific application with the following characteristics: 80W luminaire “ $Q_L = 80W$ ”, 70°C maximum temperature in the heat source “ $T_F = 70^\circ C$ ”, those input parameters shown in table 4.1 and the geometric dimensions already introduced to the model.

Table 4.1: Input data

Inputs	
Q (W)	80
T_c (°C)	10, 20, 30
$T_{e, max}$ (°C)	70
k_w (W/mK)	140
k_l (W/mK)	0.6

Validation is done by comparing the results predicted by the model with those obtained experimentally with an LHP whose characteristics are shown in Table 4.2.

Table 4.2: Geometric characteristics of LHP's prototype

Item	Value
Working fluid	Methanol
LHP housing	Copper
Primary wick	Tubular, axially grooved -Stainless steel (90 μm porous) -23 mm length -16 mm external diameter
Secondary wick	Rolled up mesh -Stainless steel mesh -70.5 mm length -7 mm external diameter
Grooves (amount/type)	7/radial
Evaporator (mm)	30 \times 30 \times 20
Compensation chamber (mm)	22 \times 22 \times 20
Pipes diameter (mm)	6

Methanol is the working fluid. The body of the LHP is copper, wick of the stainless steel and with general dimensions shown in figure 4.7.

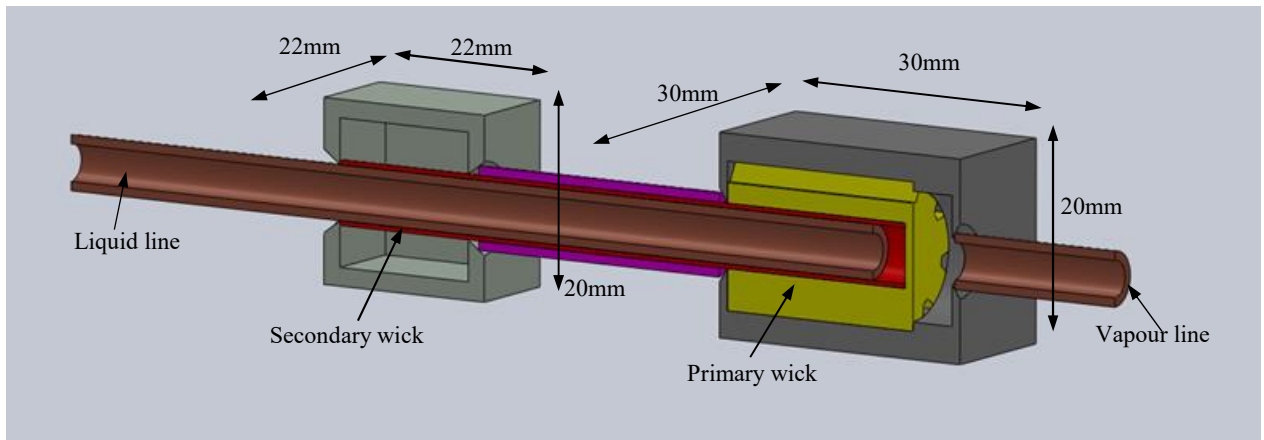


Figura 4.7: Some dimensions of the experimental LHP.

Also, Figure 4.8 shows the LHP test assembly. The source is an LED that is mounted on the evaporator and attached to it by means of screws.

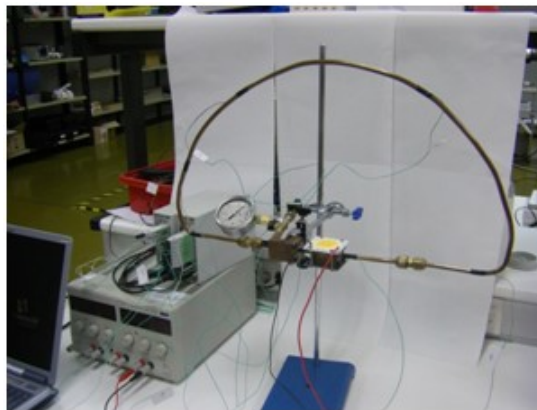


Figure 4.8: Experimental test bench.

Except for the contact surface of the LED with the evaporator, the rest of the evaporator surfaces are thermally insulated.

Validation was carried out with two tests: one with different " Q_L " thermal loads and the other with different " T_c " condensing temperatures. The comparison between the predicted and experimental temperature at the evaporator (operating temperature) for both tests is shown in figure 4.9 and 4.10.

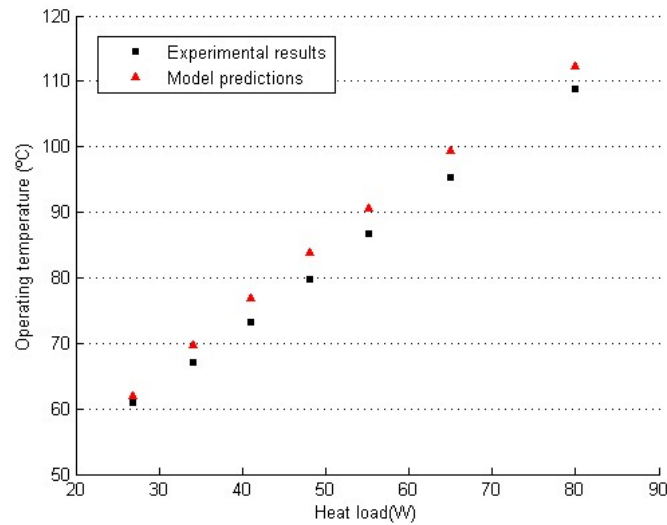


Figure 4.9: Comparison between the predicted and experimental LHP operating temperature as a function of the heat load. 25°C condensing temperature.

As seen from figure 4.9, the predicted values are slightly higher than those measured experimentally, however this deviation is less than 4%.

With respect to the condensation temperature " T_c ", figure 4.10 shows a very good correlation between the predicted value and the experimental value, with a deviation around 3%. It is verified that for values of condensation temperature below 28 ° C, the predicted value is lower than the experimental data while for higher values the situation is reversed.

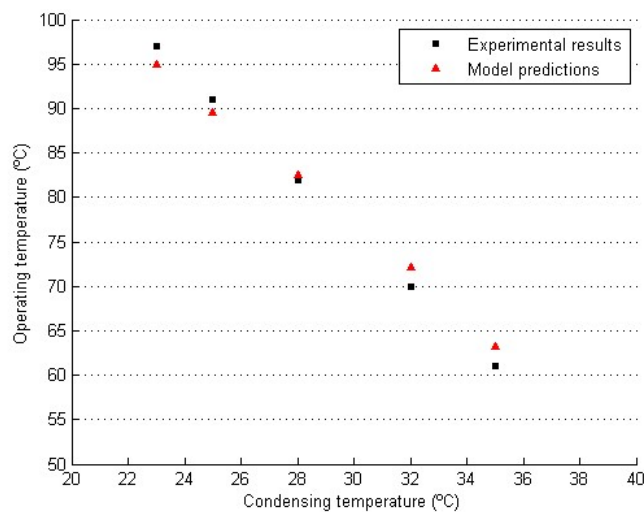


Figure 4.10: Comparison between the predicted and experimental LHP operating temperature as a function of the condensing temperature. 60w heat load

A remarkable issue from the results of figure 4.10 is that the higher the condensing temperature, the lower the operating temperature, contradictory to what the intuition marks. However, it has its reason to be when the thermal load " Q_L " is less than a critical value (depends on the fluid and configuration of the LHP). When this situation occurs, as in figure 4.10, the heat leaking from the evaporator to the compensation chamber increases as the condensation temperature decreases, which causes an increase in the temperature of the compensation chamber and, consequently, in the Operating temperature [34, 35]. When heat load is higher than this critical value, the behavior corresponds to the intuition, the lower the condensing temperature the lower the operating temperature.

In order to quantify the variations between the measured data (exp), and the numerical outcomes (model), the square of the Pearson product moment correlation coefficient was calculated " R^2 ". Coefficient that gives an idea of the linear arrangement between two variables (tmodel and experimental). A value $R^2 = 1$ indicates a linear arrangement between both variables and therefore total coincidence between the values of both variables. This coefficient value is shown in figure 4.11.

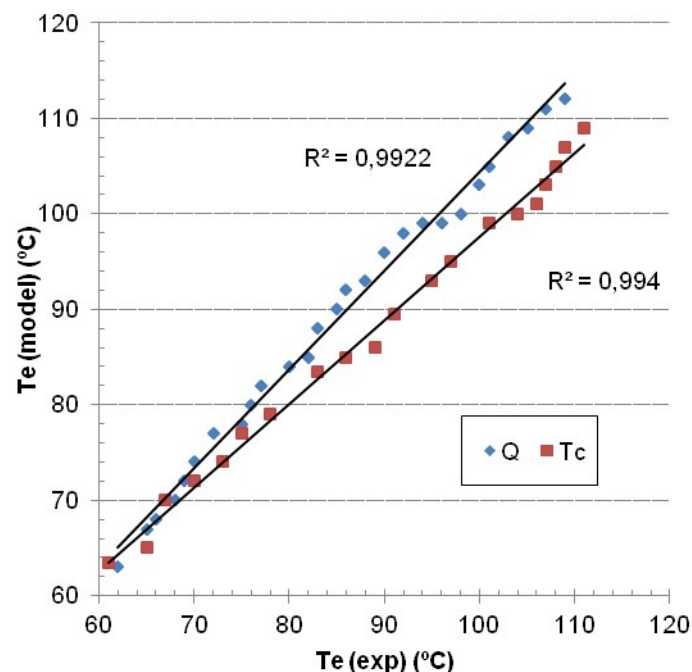


Figure 4.11: Pearson's correlation coefficient squared for both two trials

As can be seen, both tests show a coefficient almost 1, which demonstrates a good prediction and therefore the model validation.

4.3.2- Effect of vapour line length and radius.

Figure 4.12 shows the dependence of the operating temperature with the pipe radius (liquid and vapor line) and the length of the steam line " L_v ". The condensation temperature remains constant and equal to 10°C .

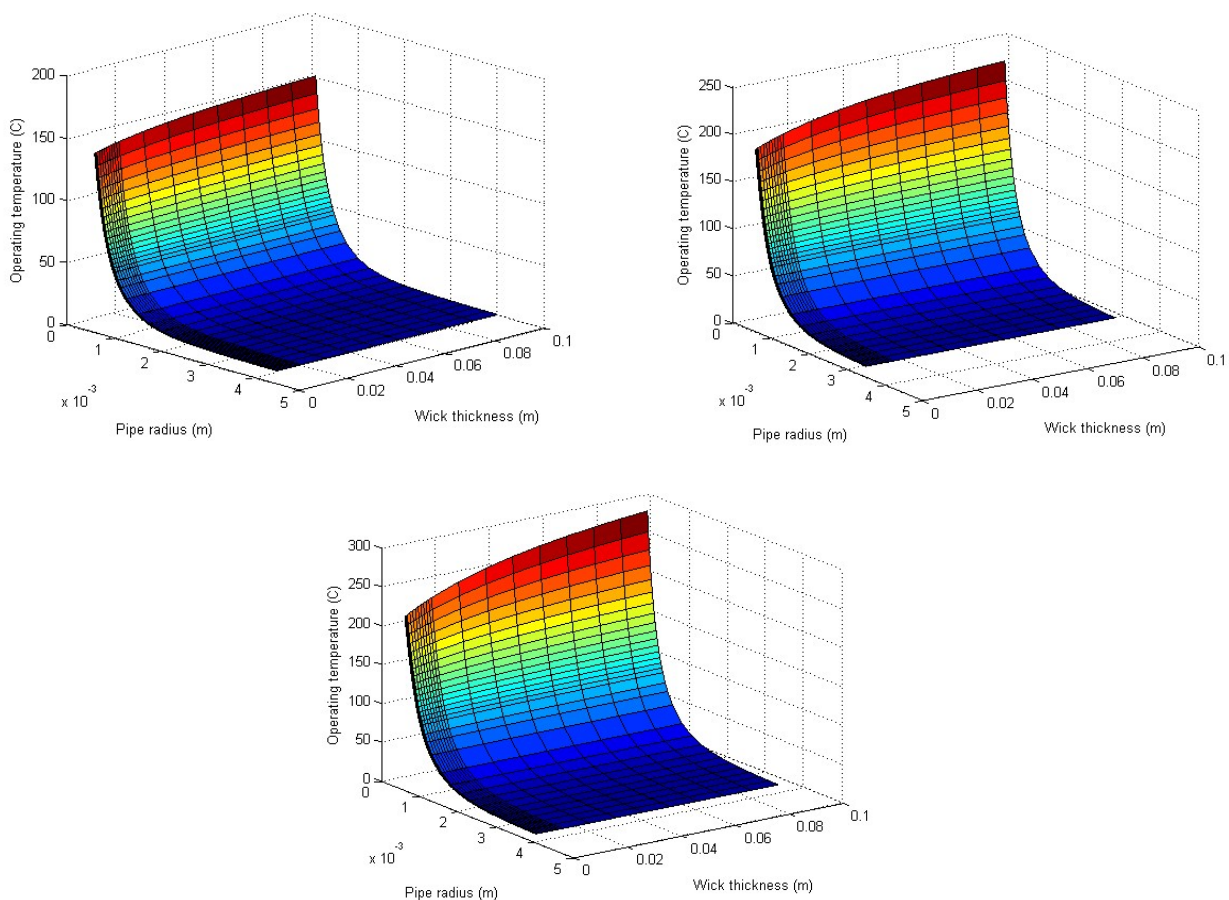


Figure 4.12: Dependence of operating temperature with radius, steam line length and wick thickness

In this figure for a given wick thickness, the greater the length of the vapor line the greater the operating temperature. This is due to fact that the longer pipe the larger the head loss and since the condensing temperature is fixed (saturation Pressure) it results that the evaporator pressure increases and so does its temperature (operating temperature). Regarding pipe radius, as it increases, the operating temperature decreases exponentially (for a given wick thickness). This is because the higher the radius, the

lower the head loss in the vapor line and therefore, for a fixed condensing temperature, the lower the pressure in the evaporator and consequently its temperature (operating temperature). Figure 4.13 shows this behaviour. For a 20°C condensing temperature, the behaviour is identical for any pipe length.

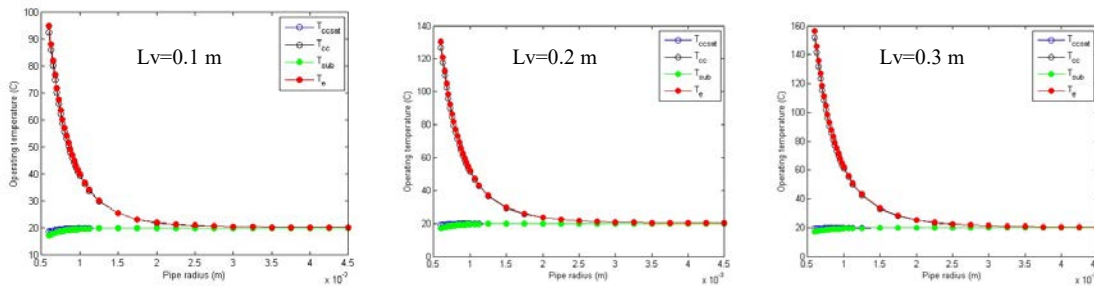


Figure 4.13. Operating temperature vs tube radius for a condensation temperature of $T_c = 20^\circ \text{C}$ for a length of steam pipe of a) $l_v = 0.1 \text{ m}$, b) $l_v = 0.2 \text{ m}$ and c) $l_v = 0.3 \text{ m}$.

From 4.13, it is easily checked that the larger the vapour line length, the higher the evaporation temperature consequence of a greater pressure loss. The existence of a critical radius value is also corroborated. Radius from which the temperatures hardly change whatever the pipe radius or the length are. Numerically, it is observed that an increase of the vapour line length from 0.1m to 0.3m, for a constant $T_c = 20^\circ \text{C}$, results in 80% operating temperature increases for given 1mm pipe radius.

Regarding wick thickness, its effect on the operating temperature is negligible. This indicates that the primary wick capillary pumping (fixed element) "loading curve of chapter 3" is larger than that required to pump through the LHP the required mass flow rate (established by the thermal loads to be evacuated and Type fluid).

4.3.3- Effect of condensing temperature.

Figure 4.14 shows the behaviour of the operating temperature for different condensing temperatures.

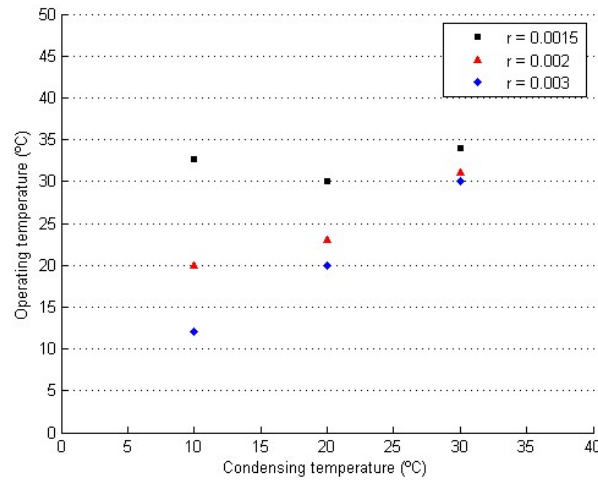


Figure 4.14: Operating temperature vs condensing temperature, $L_v=0.2\text{m}$, $Q_L=60\text{w}$

In general, it is verified that as the condensation temperature rises, so does the operating temperature. It is also observed a peculiar behaviour for a pipe radius of $1.5 \cdot 10^{-3} \text{ m}$. In this case, as the condensation temperature decreases, the operating temperature will also decrease until a critical value (20°C in this case) is reached. From this critical value, a progressive decrease in the condensing temperature causes an increase in temperature of operation, figure 4.15. This type of behaviour occurs for a combination of thermal load, pipe radius and condensing temperature. The question is to find out this combination so that it does not appear during the LHP operation, ie, the allowable operating range has to ensure that the LHP operates in the growing zone of the T-operation vs. T-condensation curve.

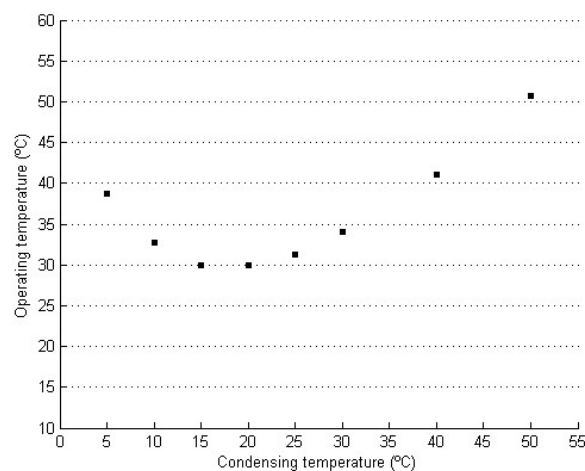


Figure 4.15: Operating temperature vs condensing temperature, critical radius = $1.5 \cdot 10^{-3} \text{ m}$;
 $L_v=0.2\text{m}$,

This decrease in the operating temperature when increasing the condensation temperature, until a minimum value, is the result of the heat leak from the evaporator to the compensation chamber, figure 4.16. When the condensing temperature is low, or below a specific value depending on the LHP design, it turns out that much of the heat from the source is transferred to the compensation chamber through the evaporator casing reducing so the heat used in the evaporation of the refrigerant. By having a smaller amount of heat in the evaporator, it results that the superheating capacity of the steam is reduced and consequently its temperature (operating temperature).

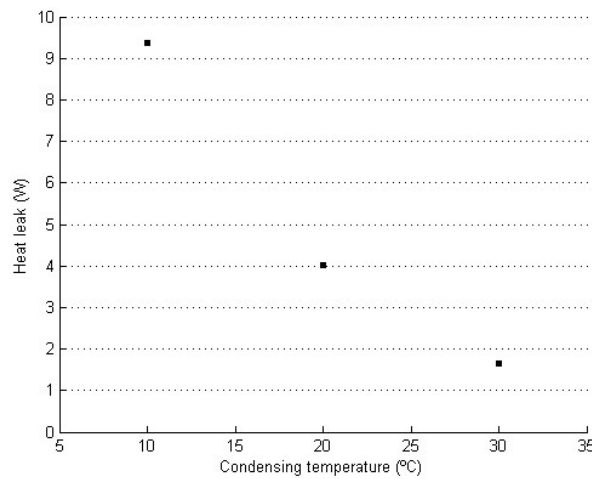


Figure 4.16: Heat leak to the C Chamber vs condensing temperature. Pipe radius = $1.5 \cdot 10^{-3}$ m

The behavior of the operating temperature against the condensing temperature and pipe radius is plotted in figure 4.17. Likewise, there is a critical radius from which the operating temperature remains invariant with the pipe radius whatever the condensing temperature.

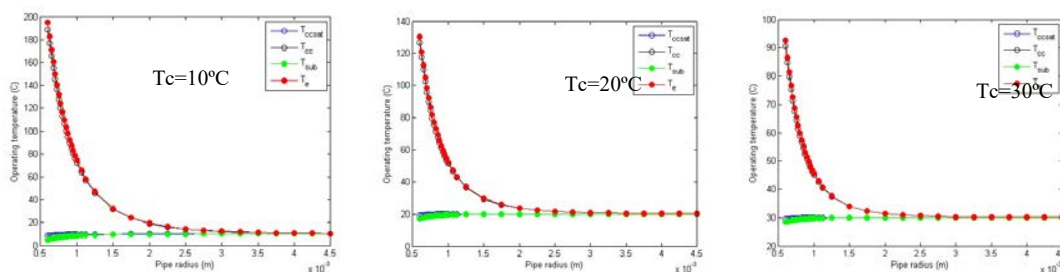


Figure 4.17: Operating temperature vs tube radius for a tube length " $L_v = 0.2$ m" and condensing temperatures: a) $T_c = 10$ °C, b) $T_c = 20$ °C and c) $T_c = 30$ °C.

If 1mm pipe radius is considered, it turns out that as the condensing temperature increases so does the operating temperature. This confirms the behaviour of figure 4.15.

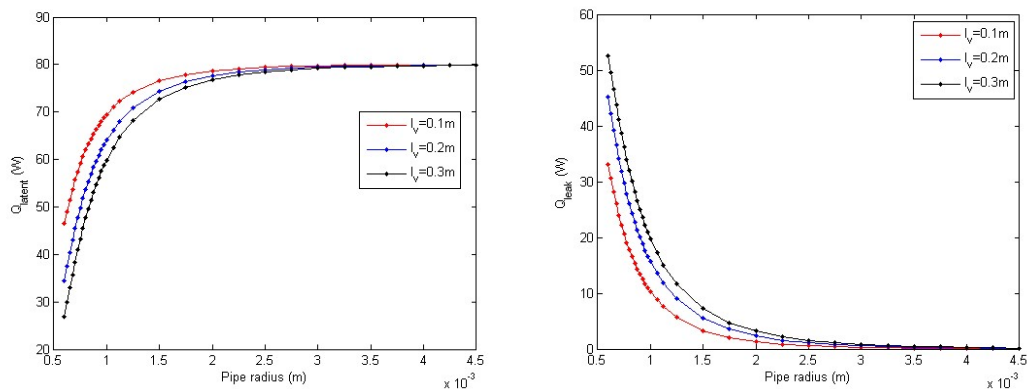
Thus, all parameters are linked together and have their effect on the LHP operation. Table 4.3 lists those combinations of geometric and operating parameters that ensure an operating temperature below the allowed limit value of 70 °C.

Table 4.3. Combination of parameters allowing $T_e < 70$ °C

Parameters combination to satisfy the $T_{e,max}$ constraint.

l_v (m)	T_c (°C)	r (m) $\times 10^{-3}$
0.1	10	>0.875
	20	>0.700
	30	>0.600
0.2	10	>1.063
	20	>0.850
	30	>0.725
0.3	10	>1.125
	20	>0.950
	30	>0.800

Finally, Figure 4.18 shows the behavior predicted by the model as a function of the evaporating latent heat " Q_{latent} " as well as the heat leaked to the " Q_{leak} " compensation chamber, for a given " $Q_L = 80w$ " heat load. Values are all based on the condensing temperature, pipe radius and vapour line length.



a)

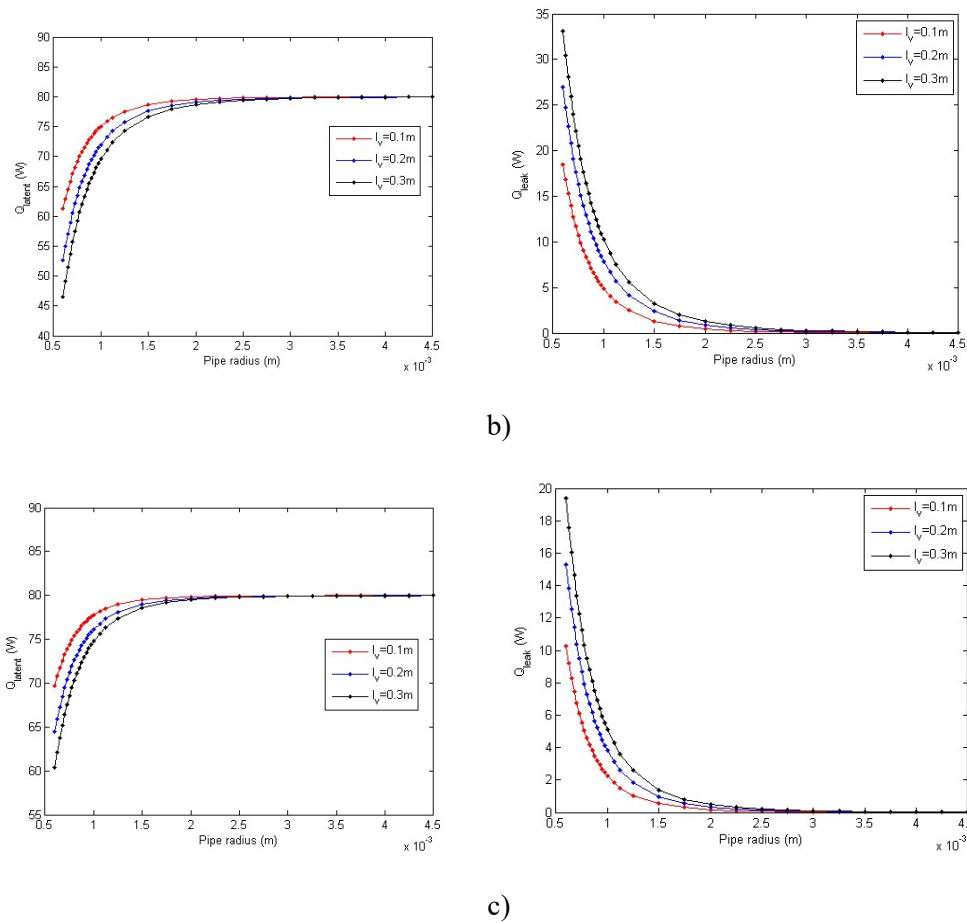


Figure 4.18: Latent heat and leakage heat ($Q_L = 80\text{ w}$) depending on the radius of the tube and the length of the vapor tube for three different condensing temperatures: a) $T_c = 10\text{ °C}$, b) $T_c = 20\text{ °C}$ and c) $T_c = 30\text{ °C}$

Some numbers. For the case of: $T_c = 10\text{ °C}$, 0.3m vapour line length and 1mm pipe radius, it is observed that 75% of the heat is used for evaporation while a 25% is lost by leaks to the compensation chamber. This LHP design should be improved in order to reduce the heat leakage.

4.4 Conclusions

- A stationary numerical model has been developed with a mathematical definition of the heat transfer coefficient towards the compensation chamber. Coefficient that allows to determine, depending on the geometric design and materials, the heat leakage from the evaporator to the compensation chamber

unlike most of the steady state models that consider this as an input parameter what requires a deep knowledge of thermodynamics by the user.

- Model validation shows a very good correspondence with the experimental values (less than 4% of drift) and therefore its appropriateness as a steady state LHP design tool.
- The model allows to check the effect of certain parameters on the operating temperature:
 - ✓ Both condensing temperature and vapour line length affect directly the operating temperature, ie as they increase, so does the operating temperature.
 - ✓ There is a pipe radius below which the operating temperature is inversely proportional to the pipe radius, ie if the radius increases the operating temperature exponentially decreases. However, from this radius, the temperature variation is almost zero.
 - ✓ As regards the condensing temperature, the model detects an atypic behaviour of the LHP when the condensing temperature is below a singular value. Value that depends on the geometric characteristics, materials and operating conditions (thermal load). It turns out that, for values below the singular value, a decrease in the condensing temperature results in an increase in the operating temperature. This, in turn, results in an increase in the percentage of the thermal load leaking from the evaporator to the compensation chamber and thus a decrease in the LHP cooling capacity.

Bibliography

- [1] J. Li, F. Lin, D.Wang, W. Tian, A loop heat pipe heat sink with parallel condensers for high-power integrated LED chips, *Appl. Therm. Eng.* 56 (2013) 18–26.
- [2] L. Yang, S.H. Jang, W.J. Hwang, M.W. Shin, Thermal analysis of high power GaN-based LEDs with ceramic package, *Therm. Acta* 455 (1–2) (2007) 95–99.
- [3] S.L. Chuang, A. Ishibashi, S. Kijima, N. Nakayama, M. Ukita, S. Taniguchi, Kinetic model for degradation of light-emitting diodes, *IEEE J. Quant. Elect.* 33 (6) (1997) 970–979.
- [4] X. Luo, S. Liu, A microjet array cooling system for thermal management of high-brightness LEDs, *IEEE Trans. Adv. Packaging* 30 (3) (2007) 475–484.
- [5] Y. Lai, N. Cordero, F. Barthel, F. Tebbe, J. Kuhn, R. Apfelbeck, et al., Liquid cooling of bright LEDs for automotive applications, *Appl. Therm. Eng.* 29 (5–6) (2009) 1239–1244.
- [6] J.M. Blanco, E. Armendáriz, J. Esarte, A parametric study of heat transfer for the optimization of fin sinks, *J. Adv. Therm. Sci. Res.* 1 (2014) 3–8.
- [7] J. Esarte, C.Wolluschek, J.M. Blanco, D. Prieto, Heat dissipaters; thermoelectrics and its energy harvesting, Chapter 20, in: *Modules, Systems and Applications in Thermoelectrics*, vol. 2, CRC Press, Taylor and Francis Group, 2012, pp. 1–40
- [8] J. Esarte, Gao Min, D.M. Rowe[†] “Modelling heat exchangers for thermoelectric generators”. *Journal of Power Sources*, Vol. 93/1-2; pages 72-76. 2001
- [9] J Amir Faghri. “Heat Pipe Science and Technology”, Taylor & Francys, ISBN 1-56032-383-3.
- [10] J. Esarte, Manuel Dominguez. “Capillary Mechanism for the Heat Dissipation through a Thermoelectric Pellet”. *Applied Thermal Engineering (Elsevier Science)* –Vol. 23, Issue 13. September 2003
- [11] Y.F. Maydanik, Loop heat pipes, *Appl. Therm. Eng.* 25 (5–6) (2005) 635–657.
- [12] L.L. Vasiliev, Heat pipes in modern heat exchangers, *Appl. Therm. Eng.* 25 (1) (2005) 1–19
- [13] B. Siedel, V. Sartre, F. Lefèvre, Literature review: steady-state modeling of loop heat pipes, *Appl. Therm. Eng.* 75 (22) (2015) 709–723.
- [14] M. Furukawa, Model based method of theoretical design analysis of a loop heat pipe, *J. Therm. Heat Transf.* 20 (1) (2006) 111–121.
- [15] V.V. Vlassov, R.R. Riehl, Mathematical model of loop heat pipe with cylindrical evaporator and integrated reservoir, *Appl. Therm. Eng.* 28 (8–9) (2008) 942–954.

- [16] M. Hamdan, F.M. Gerner, H.T. Henderson, Steady state model of a loop heat pipe (LHP) with coherent porous silicon (CPS) wick in the evaporator, *J. Heat Mass Transf.* 35 (2003) 46–53.
- [17] J. Li, D. Wang, G.P. Peterson, Experimental studies on a high performance compact loop heat pipe with a square flat evaporator, *Appl. Therm. Eng.* 30 (6–7) (2010) 741–752.
- [18] Y.F. Maydanik, M.A. Chernysheva, V.G. Pastukhov, Review: loop heat pipes with flat evaporators, *Appl. Therm. Eng.* 67 (1–2) (2014) 294–307.
- [19] B.J. Huang, H.H. Huang, C.W. Chen, M.S. Wu, Development of high-power LED lighting luminaires using loop heat pipe, *J. Light Vis. Env.* 32 (2) (2008) 148–155.
- [20] X.Y. Lu, T.C. Hua, M.J. Liu, Y.X. Cheng, Thermal analysis of loop heat pipe used for high-power LED, *Therm. Acta* 493 (2009) 25–29.
- [21] Brent Cullimore, Jane Baumann, “Steady-state and Transient LHP modelling”. Copyright ©2000 Society of Automotive Engineers, Inc.
- [22] Nasahito Nisikawara, Hosei Nagano, “Transient Thermo-Fluid Modeling of Loop Heat Pipes and Experimental Validation”. 42nd AIAA Thermophysics Conference, 27 - 30 June 2011, Honolulu, Hawaii
- [23] R.R. Riehl, T. Siqueira, Heat transport capability and compensation chamber influence in loop heat pipes performance, *Appl. Therm. Eng.* 26 (11–12) (2006) 1158–1168.
- [24] L.L. Vasiliev, Micro and miniature heat pipes – electronic component coolers, *Appl. Therm. Eng.* 28 (4) (2008) 266–273.
- [25] R. Singh, A. Akbarzadeh, C. Dixon, M. Mochizuki, Theoretical modelling of miniature loop heat pipe, *J. Heat Transf.* 46 (2009) 209–224.
- [26] Z. Wan, J. Deng, B. Li, Y. Xu, X. Wang, Y. Tang, Thermal performance of a miniature loop heat pipe using water–copper nanofluid, *Appl. Therm. Eng.* 78 (5) (2015) 712–719.
- [27] J. Ku. Operating characteristics of loop heat pipes. 29th International Conference on Environmental System, July 12–15, 1999, Denver, Colorado.
- [28] J. Esarte, A. Bernardini, J.M. Blanco, R. Sancibrian. Optimizing the design for a two-phase cooling loop heat pipe Part A: Numerical model, validation and application to a case study, *Appl. Therm. Eng.* 99 (2016) 892–904.
- [29] B.Cullimore, J.Baumann. Steady-State and Transient Loop Heat Pipe Modeling, SAE international, (2007), paper number: 2000-01-2316, DOI: 10.4271/2000-01-2316

- [30] M.C. Page, M.J. Brooks, L.W. Roberts, C. Bemont. Modelling and Experimental Validation of a Loop Heat Pipe, R & D Journal of the South African Institution of Mechanical Engineering 2013, 29, 26-35.
- [31] Valeri V. Vlassov, Roger R. Riehl. Mathematical model of a loop heat pipe with cylindrical evaporator and integrated reservoir of a Loop Heat Pipe, Applied Thermal Engineering, 28 (2008) 942–954
- [32] B. Siedel, V. Sartre, F. Leflèvre. Complete analytical model of a loop heat pipe with a flat evaporator. International Journal of Thermal Sciences, Elsevier, 2015, 89, pp.372-386.
- [33] E.G. Alexander, Structure-property relationships in heat pipe wicking materials (Ph.D. thesis), North Carolina State University, Raleigh, NC, 1972.
- [34] J. Ku, J. Rodriguez. Low frequency high amplitude temperature oscillations in loop heat pipe operation, SAE International July 2003.
- [35] P.H.D. do Santos, R. Mertz, E. Bazzo. Experimental investigation of an acetone loop heat pipe using a ceramic porous wick in the capillary evaporator. 20th International Congress of Mechanical Engineering, November 2009.

Chapter 5. Manufacturing and experimental testing of the LHP.

5.1 Introduction	99
5.2 Primary Wick	99
5.2.1-Permeability, “ κ ”	101
5.2.2- Wettability- Capillary Pumping, “ φ ”	102
5.2.3-Thermal conductivity “ K ”	105
5.3. Secondary Wick	106
5.3.1-Transport capacity “TC”	107
5.4. LHP-Results	110
5.4.1- Starting up	112
5.4.2- Charge of refrigerant.	114
5.4.3- Condensation/ambient temperature.	116
5.5. Conclusions	119
Bibliography	121

5.1 Introduction

Chapter 4 describes the mathematical model developed for LHP design. In chapter 5 a prototype LHP for a specific application is developed. Prior the LHP development / manufacturing, thermal characterizations of the used wicks (primary and secondary) are performed in order to satisfy the thermal-fluidic requirements that any application requires. Finally, the LHP is assembled to proceed with the operating tests.

5.2 Primary Wick

As discussed in Chapter 3, the wick is the key piece in the capability and functionality of a LHPs. The different manufacturing techniques used to create such components determine the future capacity of the device very much. In the present thesis, the manufacturing technology used is the 3D laser printing, "SLM, Selective Laser Melting" technology due to the benefits described and analysed in chapter 3, among them the greater permeability to the refrigerant flow [1 , 2].

In the primary wick manufacturing process by SLM, the first step is to generate the wick's CAD file containing the its geometry (external passages and external channels, type of material). This file is subsequently loaded into the 280 HL printer with a series of manufacturing specifications, Table 5.1.

Table 5.1: Technical specifications for the 280 HL printer

Item	Value
Build Envelope (L x W x H)	280 x 280 x 365 mm ³
3D Optics Configuration	Dual (1x 400 W und 1x 1000 W); IPG fiber laser
Build Rate	up to 55 cm ³ /h
Variable Layer Thickness	20 μm - 75 μm
Min. Feature Size	150 μm
Beam Focus Diameter	80 - 115 μm
Max. Scan Speed	10 m/s
Average Inert Gas Consumption in Process	2,5 l/min (argon)
Average Inert Gas Consumption Purging	70 l/min (argon)
E-Connection / Power Input	400 Volt 3NPE, 32 A, 50/60 Hz, 3,5 - 5,5 kW
Compressed Air Requirement / Consumption	ISO 8573-1:2010 [1:4:1], 50 l/min @ 6 bar

Laser intensity, radius of action, powder supply flow, dust matrix, layer depth, etc. are then adjusted in the printer to begin manufacturing, figure 5.1.

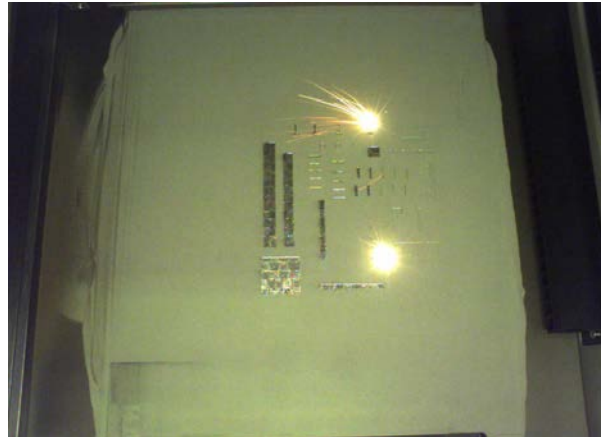


Figure 5.1: SLM 3D additive process. Courtesy of LORTEK

At the end, the desired product is obtained with the external and internal shape of the design to fulfil its function [3], figure 5.2.

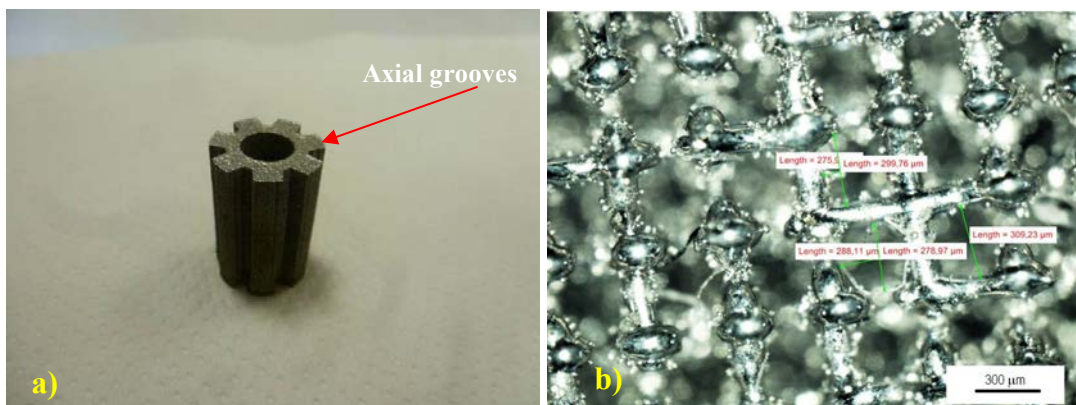


Figure 5.2 a) Primary kick external appearance, b) internal passages

Once fabricated, its fluidic-thermal characterization is carried out. Characterization obtained through 4 tests that allow the determination of parameters such as: permeability, wettability, capillary pumping and thermal conductivity.

5.2.1-Permeability, “ K ”

As described in Chapter 3, the permeability measures the ability of the porous structure to let a liquid flow through it. The experimental determination of this parameter is carried out with a permeability test bench, figure 5.3.

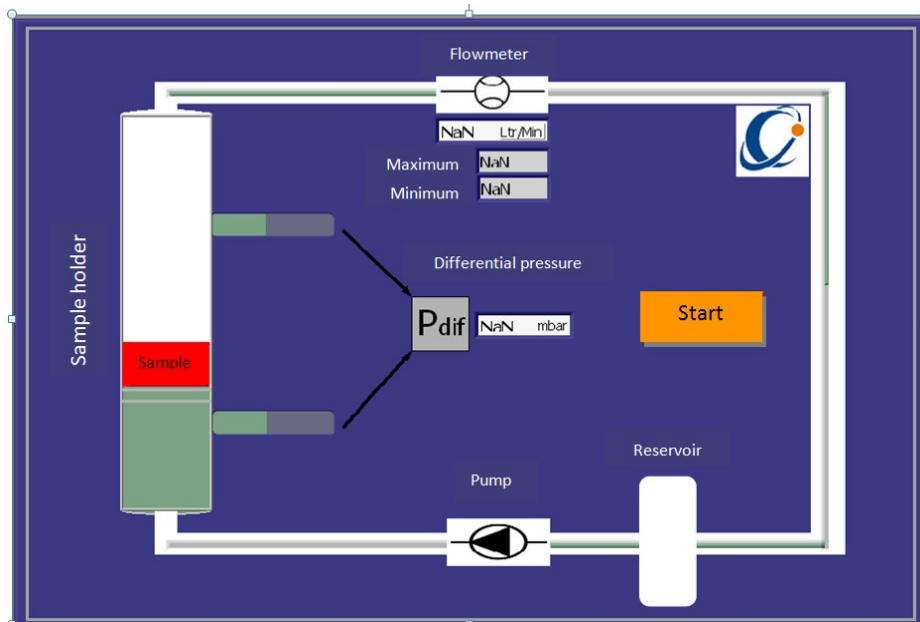
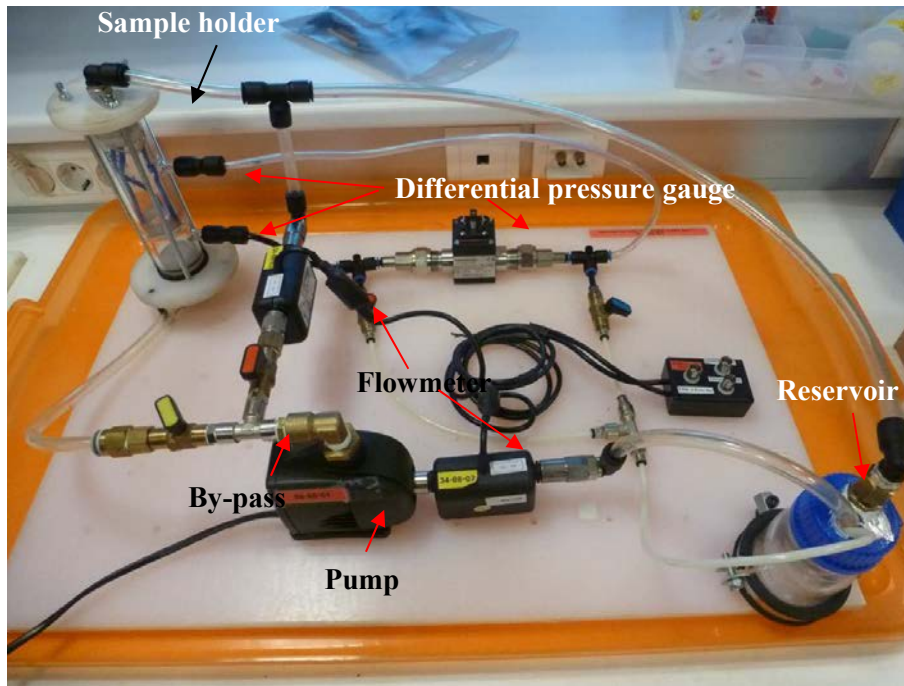


Figure 5.3: Porous media permeability equipment

It is a closed circuit in which the fluid circulates thanks to the capillary action through the sample whose permeability is intended to be determined. The fluid is

discharged and aspirated from a reservoir which acts as a deaerator and pressure damper.

The sample holder has two pressure ports, one before and another just after the sample, where a differential pressure gauge that measures the pressure drop through the sample is connected. The fluid flowing through the sample is measured with a flow meter. In order to have a finer control of the flow, due to pump limitations, the circuit has a bypass that allows to reduce the flow through the sample to levels in which the viscous friction force is predominant versus inertial force. In such a case, Darcy's law that linearly relates pressure drop to the flow rate (velocity) is applicable. The proportional coefficient is the so-called permeability, “ \mathcal{K} (m²)”

$$Q = - \frac{\mathcal{K} A \Delta P}{\mu L} \quad (1)$$

Being: “A”, The wick cross-section, “ ΔP ” the pressure drop along the wick, “ μ ” fluid dynamic viscosity, “L” the wick thickness and “Q” the flow rate. (m³/s) [4].

Thus, obtaining the permeability consists of plotting the curve P/Q (pressure drop/flow rate), figure 5.4. To do this, several tests are carried out in the test bench where pressure drop is recorded for any flow rate flowing through the wick, low Reynold numbers. Then, the wick permeability value is determined. (1.25 10⁻¹² m²).

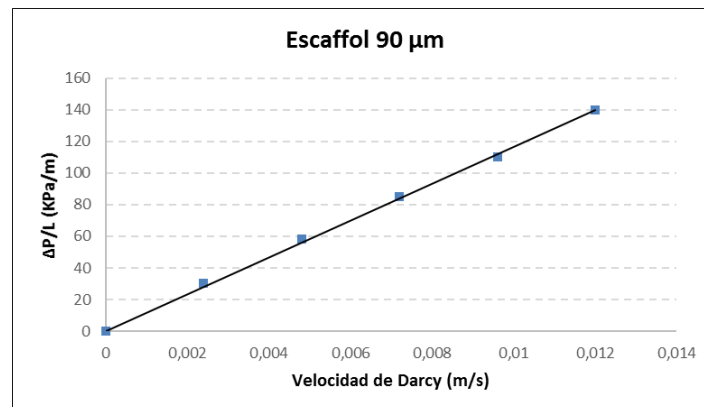


Figure 5.4: Pressure/Velocity curve for the 90µm escafol

5.2.2- Wettability- Capillary Pumping, “ φ ”

Wettability is a surface property by which a surface presents avidity for or repulsion of a liquid (interaction between superficial molecules of the liquid and those of the solid

which comes in contact with it). This is defined by the "contact angle" which is the angle that forms a liquid drop when deposited on the solid's surface. This method is not applicable to porous media because liquid is absorbed, therefore it is indirectly determined by the Washburn method or capillary ascent method (depth of penetration of the liquid in the Wick) [5]. Three different liquids were used: water, acetone and methanol. As a qualitative mode, in order to observe whether drop penetrates into the wick and how fast it does, a drop is poured on the wick, figure 5.5.

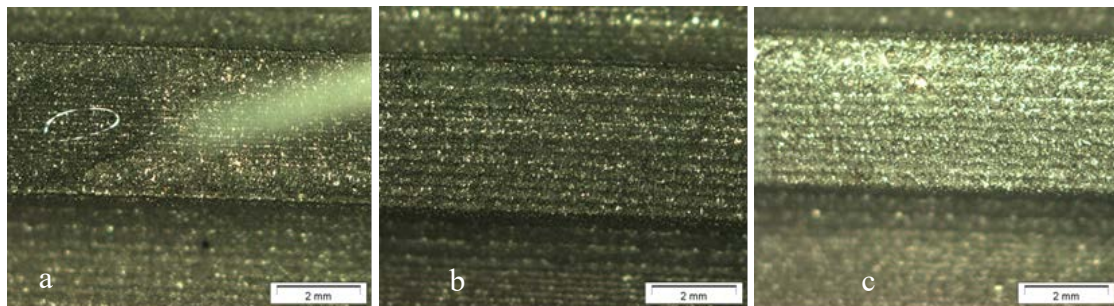


Figure 5.5 Drop evolution. a) drop of water after 1 minute; b) acetone drop after 1 second; c) methanol drop after 1 second

These are photographs taken with an optical microscope at the moment drop begins to penetrate just after its deposition on the wick. In the case of the water drop, it is observed that after 1 minute the drop is still on the wick surface what demonstrates the low wick absorptivity to water, low wettability. The opposite occurs with acetone and methanol, in both cases the drop is absorbed quickly, less than 1 second, showing a high wettability.

This is a quick, simple but qualitative procedure to measure how well or badly a fluid wets the wick. A more quantitative measurement requires of the so-called capillary ascent method (height ascension versus time), Washburn, described in Chapter 3. Figure 5.6 shows images of the experiment for the three tested fluids.

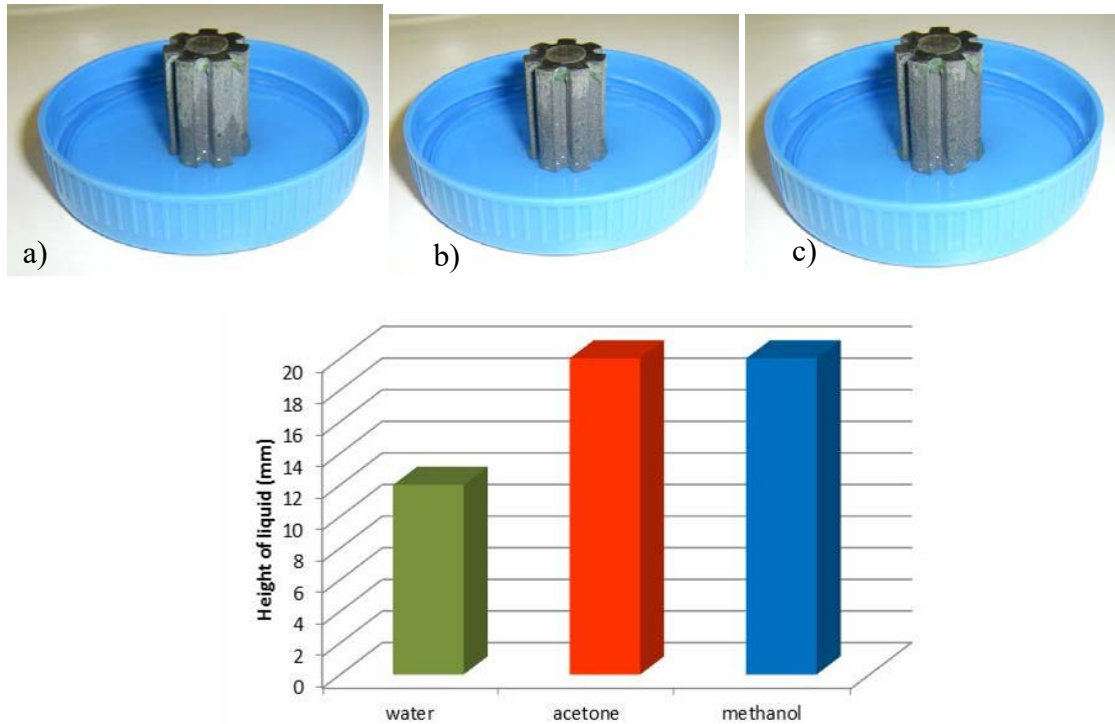


Figure 5.6: A) water rise after 5 minutes) acetone rise after 1 second; C) methanol rise after 1 second

As can be seen from figure 5.6, the water ascension is very slow (low height after 5 minutes), low capillary action, whereas for acetone and methanol this is very fast, high capillary action. By registering the raised height versus time, curve V/t , it can be foreseen the maximum height (asymptote) the wick can pump.

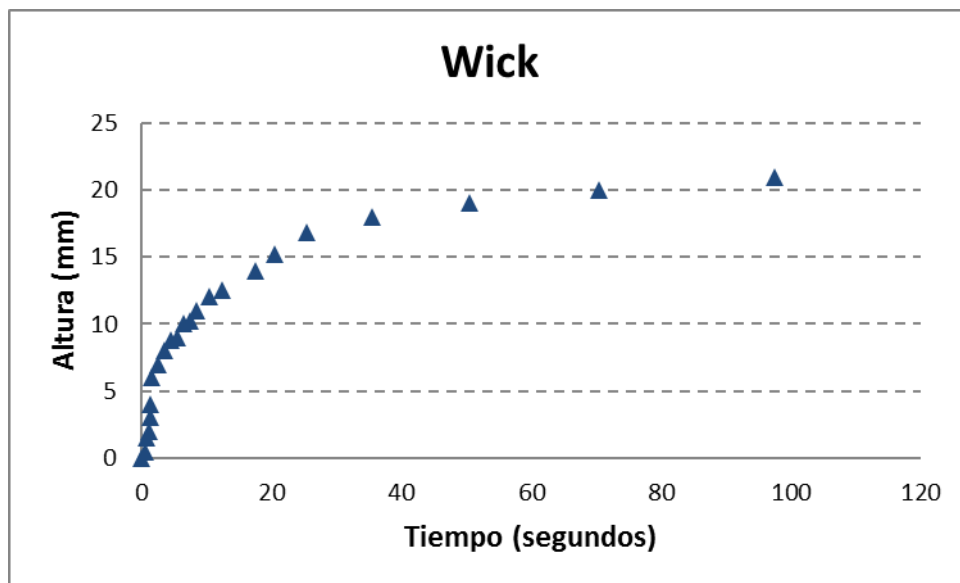


Figure 5.7: Liquid rise curve

With this maximum height value and equation (2) the value of the contact angle " ϕ ", wettability, between wick and fluid is indirectly determined.

$$\frac{2\sigma \cos \phi}{r_{eff} \rho g} = h_{max} \quad (2)$$

Table 5.2 shows the contact angles for the three fluids tested: water, acetone and methanol.

Table 5.2: Wick’s contact angles for three liquids

Fluid	Contact angle
Water	>90°
Methanol	30°
Acetone	30°

For this case, the chosen fluid is methanol due to its chemical compatibility with the Viton joints used as sealants in the evaporator – compensation chamber. Acetone is not compatible with Viton.

5.2.3-Thermal conductivity “K”

Thermal conductivity represents the ability of a solid to conduct heat from the hottest side to the coldest one. In LHPs this parameter is important not only because of its direct impact on the heat transfer to the liquid evaporation but also for its influence on the thermal leakage to the compensation chamber. Various configurations and materials have been employed and characterized in order to find ad-hoc conductivities [6].

In this work, the wick is a single material whose conductivity is measured with the commercial equipment "THB - Transient Hot Bridge" of LINSEIS, figure 5.8. Equipment that allows to measure the conductivity of solids (dense or porous), liquids and powders.



Figure 5.8: Thermal conductivity equipment

Unlike a stationary measuring equipment, THB does not need to reach temperature stability (cold-hot side) to measure the thermal conductivity, it is determined by measuring the slope of the temperature versus time curve at the first instants of the measurement. For the case of the 3D printing wick, the conductivity value turns out to be: **$K = 1.48 \text{ W/m K}$** .

Once the thermal and fluidic characterizations have been completed, next step is the assembly inside the evaporator. One end of the wick is closed to ensure that the liquid flows radially from of the core towards the periphery. The other wick end is left open at the core to allow liquid to enter from the liquid line. It is the wick closed end that is placed on the evaporator's side close to the inlet vapour line.

5.3. Secondary Wick

Secondary wick has two clear functions in the LHP. On the one hand, to supply liquid to the primary wick (evaporator) when liquid coming from the liquid line is not sufficient (transient phenomena) and on the other hand, to absorb any bubbles that are generated into the evaporator core [7, 8].

This secondary wick is created from a 300 μm pitch stainless steel wire mesh, Figure 5.9.

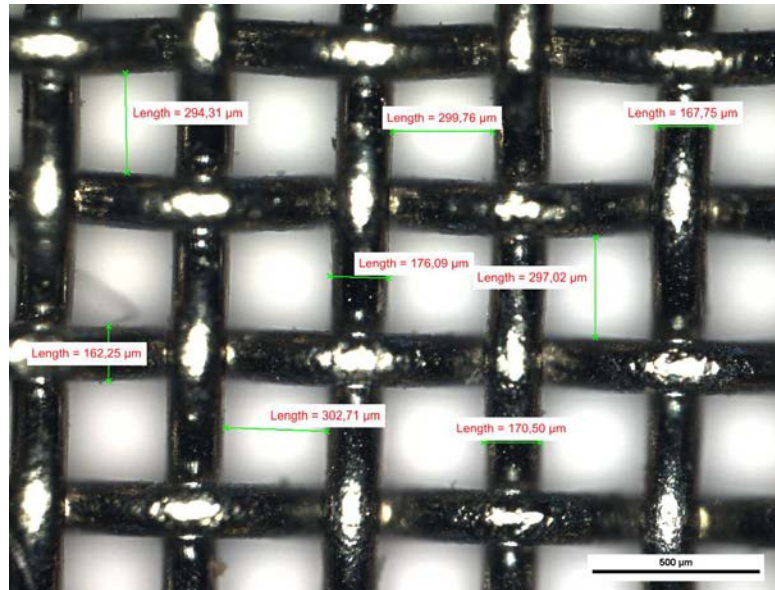


Figure 5.9: Stainless steel mesh image

This mesh is rolled with three turns in order to create a hollow cylinder with a 7mm outer diameter and 0.5mm wall thickness (generated by the three mesh turns). This wick is placed in the core of the primary wick and serves as a hydraulic connection between the compensation chamber and the primary wick. This link must ensure the liquid supply from the compensation chamber to the primary wick to avoid hot spots (areas without liquid) that appear when a decompression between the vapor generated and the liquid returning occurs. In case it happens, the LHP heat transfer capacity is reduced.

5.3.1-Transport capacity "TC"

The liquid transport capacity of the secondary wick is called the **transport capacity** "TC" and is defined as the thermal load per meter that the secondary wick can transfer while keeping the evaporator temperature " T_0 " [9] constant, i.e. the length that the liquid is able to travel through the secondary wick without there being any variation in the evaporator temperature. This length depends on the wick characteristics as well as the thermal load applied to the evaporator. As known, when applying a thermal load to the evaporator a liquid-vapor interface along it is generated. As the heat load increases, the interface is no longer levelled along the primary wick, figure 5.10 a). This decompression causes a temperature increase " $\Delta T = T_1 - T_0$ " at a given point "S" at the interface, figure 5.10 b).

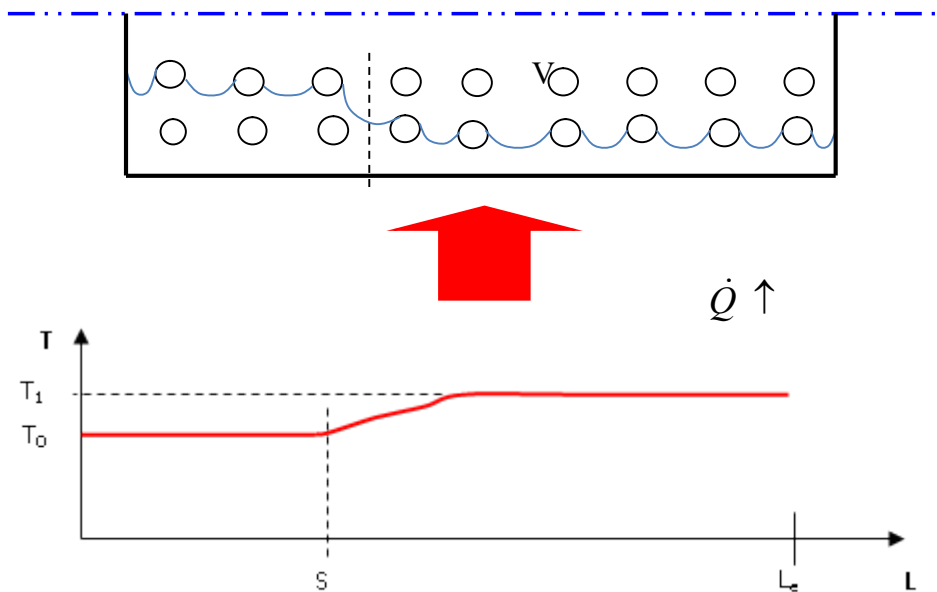
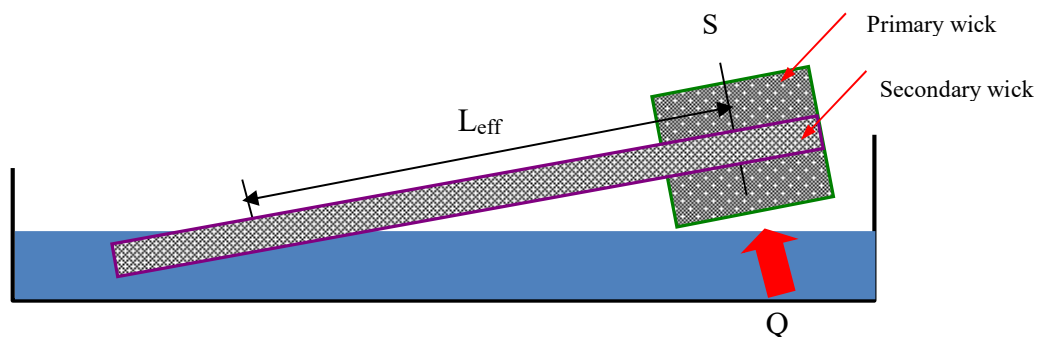


Figure 5.10: Temperature drop in the primary wick because of thermal imbalance.

If the heat load is increasing, then this temperature difference increases to the point of drying off part of the primary wick causing an evaporator overheating (large temperature rise). To avoid this, given a determined heat load for the LHP, a maximum value for this increase " ΔT " (in this case 0.7°C) is established when designing a LHP. All this requires a maximum value of "TC" for the secondary wick.

The "TC" or effective length required to transfer the design thermal load "Q" is obtained by a simple test as shown in Figure 5.11.



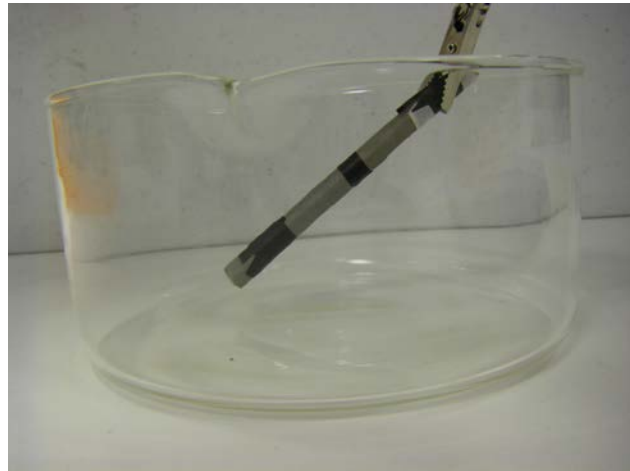


Figure 5.11: “TC” test for the secondary wick.

The secondary wick is placed with one end immersed into a vessel with the liquid to be transported and the other end inserted into a heater where the heat load is applied. Evaporator temperatures are monitored to observe any excessive temperature increase. Heat load is stepwise increased until a temperature rise above the set value is observed. If it happens, then the point of the evaporator "S" where it occurs is recorded and the corresponding distance " L_{eff} " is measured. If this length is greater than or equal to the physical length required to connect the compensation chamber to the evaporator then the secondary wick is correct, otherwise both secondary wick and heat load must be modified. For the case of a 80w heat load, " $L_{eff}=150\text{mm}$ " while the physical length is " $L=70\text{mm}$ ".

$L_{eff} \geq L$, then the secondary wick configuration is valid.

The parameter "TC" is obtained from equation (3)

$$TC = \dot{Q} L_{eff} = 12 [w.m] \quad (3)$$

5.4. LHP-Results

Once all the constituent elements and the operating conditions have been defined, the assembly of all of them, the refrigerant charge and the experimental tests of operation, are performed, figure 5.12.

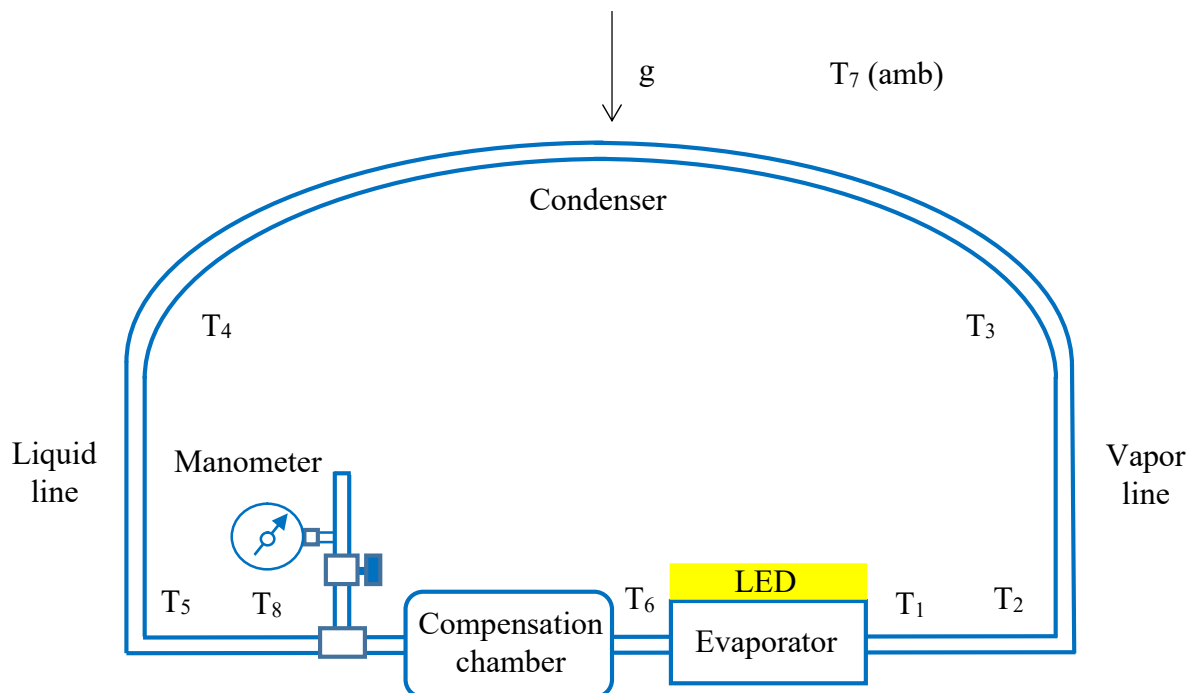
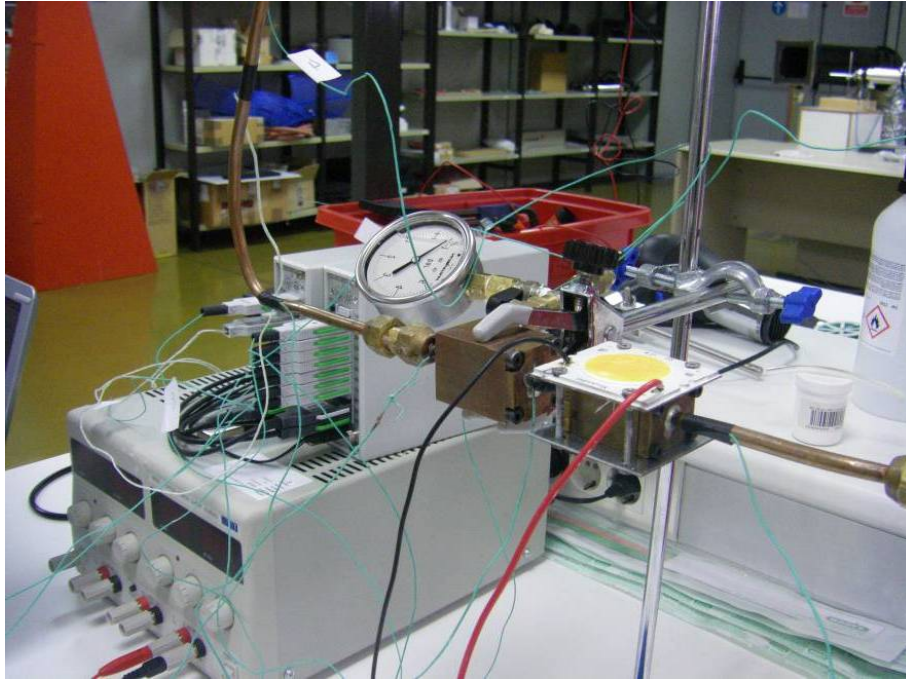


Figure 5.12: LHP test bench.

The heat source is a BRIDGELUX LED (up to 80w), which is placed directly on one side of the evaporator.

The test bench is equipped with 8 temperature probes "K" type (accuracy ± 0.5 ° C at 100 ° C), positioned as shown in figure 5.12. T_1 just after the evaporator, then T_2 , T_3 and T_4 in points of the condensation zone (start and end theoretically). T_5 just before T_8 which is next to the compensation chamber entrance. T_6 is placed between the evaporator and the compensation chamber. The test bench has a manometer and a power supply to power the LED. All this fully controlled and registered. Table 5.3 shows some of the equipment characteristics while table 5.4 does for the LHP's components.

Table 5.3: Characteristics of the equipment

Item	Value
THERMOCOUPLES	
Type	K
Number	8
DATALOGGER	
Model	ALMEMO 5590-2 v5
Operating temperature (°C)	-10 to +120
Humidity of ambient air (%)	10 to 90
MANOMETER	
Type	Bourdon
Accuracy	$\pm 3-2-3\%$ or $\pm 1.6\%$ full scale
Pressure range (bar)	0-10

Table 5.4: Characteristics of the LHP's components

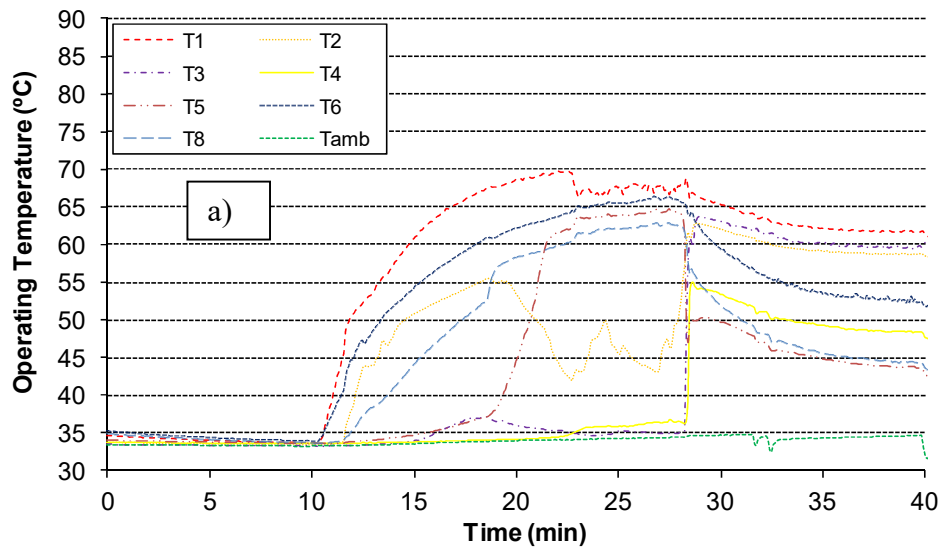
Item	Value
<i>Evaporator</i>	
Volume (mm ³)	2827
Active length(mm)	23.2
Material	Copper
<i>Compensation Chamber</i>	
Volume (mm ³)	961
Active length (mm)	17
Material	Copper
<i>Liquid/Vapor line</i>	
Outer diameter (mm)	6
Inner diameter (mm)	4
Length (mm)	100
Material	Copper
<i>Primary Wick</i>	
Pore radius (μm)	80
Permeability (m ²)	$1.25 \cdot 10^{-12}$
Porosity (%)	17
Thermal conductivity (W/mK)	1.48
Number of grooves	7
Outer diameter (mm)	16
Inner diameter (mm)	7
Length (mm)	23

Material	Stainless steel AISI 316
<i>Secondary Wick</i>	
Pore radius (μm)	300
Outer diameter (mm)	7
Inner diameter (mm)	6
Length (mm)	70.5
Material	Stainless steel mesh

5.4.1- Starting up

The tests were performed under two different ambient conditions: one at 25°C and the other at 35°C. For each of these conditions tests are run for different heat loads. These heat load changes allow a progressive LHP start-up [10] so that the LHP is automatically activated without any external assistance.

At start-up, the evaporator temperature rises rapidly even exceeding the limit value for a brief period until it drops to the steady operating value. This behaviour depends on the initial thermal load, figure 5.13.



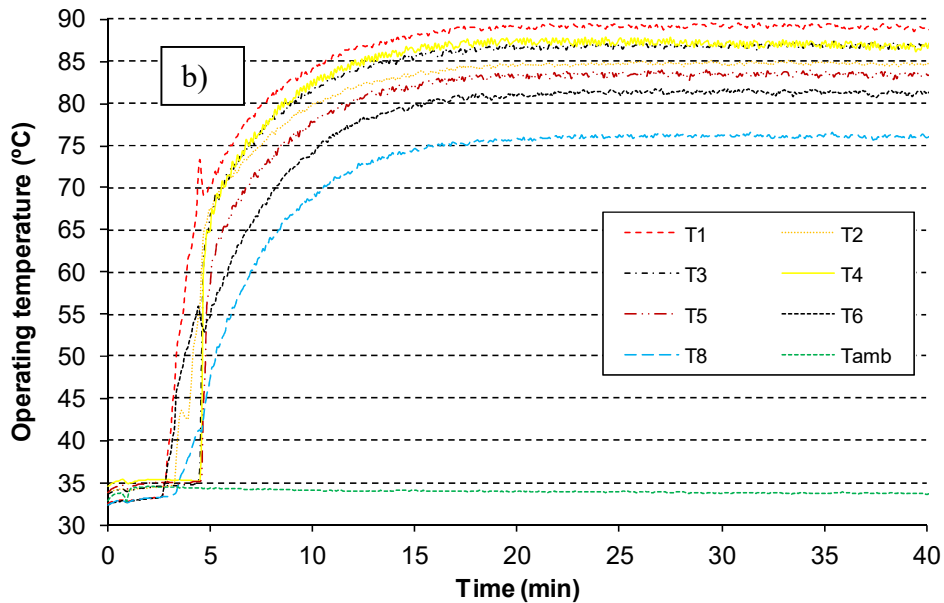


Figure 5.13: Start at 35°C ambient for different thermal loads: a) 57 W; b) 120 W.

As shown in figure 5.13, the LHP device reaches the steady state with a 15°C temperature difference between Evaporator temperature and that of the Compensation Chamber whatever the heat load is (57w and 120w). In both cases, no overheating at all is observed [11]. This shows that the LHP device has at least capacity to work with thermal loads of up to 120w at ambient temperatures of 35°C.

If we look at the start, it is observed that for the case of 57w the temperatures undergo a rise above the steady value that is not observed for the case of 120w. Likewise, the times at which temperatures begin to experience a change are different, unlike the case at 120w in which all experience variation in unison. They are the temperatures closest to the evaporator and C.C that more quickly detect any variation what indicates that the evaporator has not started yet and therefore it is not operating as two-phase system, ie, no capillary force has been generated (pure conduction). When temperatures start to fall (variation of the T3 and T4) the LHP begins to operate, circulation of refrigerant. In the case of 120w, the LHP starts operating as such from the beginning, without overheating as in the case of 57w, resulting in smoother operation. This is because the evaporation takes place from the first moment making the refrigerant flow and thus, avoiding overheating. On the other hand, the start times are different, longer for the case of low load (57w) and shorter and soft for the case of higher load (120w). From this, it is concluded that the LHP presents a more optimal

start-up at 120w heat load, although it is able to operate in an optimal way for both heat loads.

5.4.2- Charge of refrigerant.

As far as the refrigerant charge is concerned, there is a maximum permissible load. This maximum value results from the fulfilment of two LHP constraints [12,13]. Each of these restrictions sets a maximum charge when the LHP operates under certain conditions. The minimum of these maximums will be the maximum refrigerant charge to be introduced into the LHP. One of these restrictions states that when the LHP device is at its maximum temperature in non-operation mode (eg in storage), then the volume of liquid refrigerant must be less than the total volume of the device; " V_i ". The other restriction states that when the LHP is at its maximum operating temperature (corresponding to its maximum thermal capacity and the most unfavorable condensing conditions), the volume of liquid refrigerant must be less than the sum of the volume of the liquid line, evaporator core and the compensation chamber; " V_{ii} ".

$$V_{\max} \leq \text{lower of } V_i, V_{ii}$$

In addition, there is a minimum refrigerant charge, " V_{\min} ", this is one that ensures full flooding of the wicks by the refrigerant when the LHP is in storage or non-operation mode. If the minimum refrigerant charge value exceeds the maximum charge value, then a redesign of the LHP (change in some of its dimensions, usually increasing the volume of the compensation chamber) is required.

If, $V_{\max} < V_{\min} \Rightarrow$ LHP redesign.

In the present case, $V_{\max} = 28\text{gr}$ and $V_{\min} = 16\text{gr}$. Therefore, the amount of refrigerant with which is possible to fill up the LHP is a value between 16 and 28gr.

Once the refrigerant charge restrictions are fulfilled, an analysis of the refrigerant charge effect on the LHP temperatures is carried out. Figure 5.14 shows this effect for two different heat loads: 20gr and 22gr.

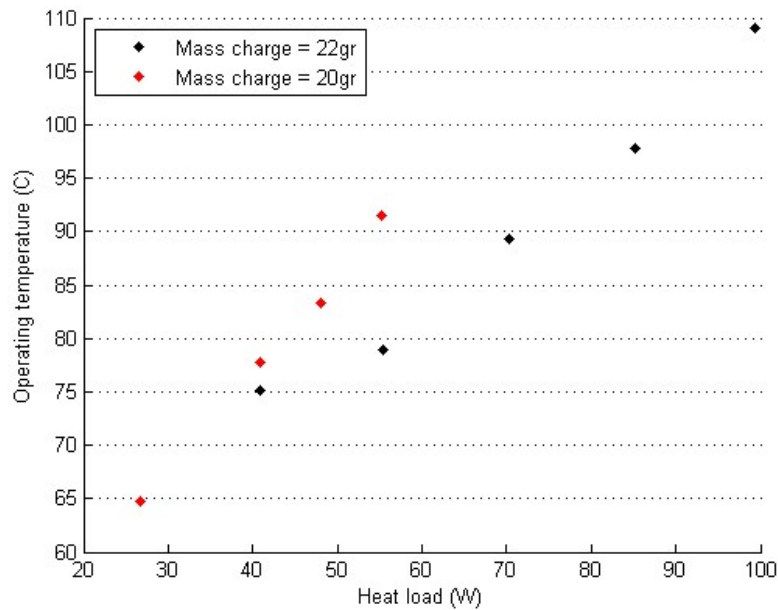


Figure 5.14: Operating temperature as a function of thermal load and the refrigerant charge.

As can be seen, as the heat load increases, the increase in the operating temperature is lower for higher refrigerant charges, ie for high heat loads, higher refrigerant charges are preferable. However, for low heat loads, small refrigerant charges are recommended. This goes to say that: depending on the heat load to be evacuated and the maximum temperature allowed for the heat source, there is a refrigerant charge that makes it operate optimally (any other casuistry, for that given refrigerant charge, will cause it to operate less optimally). For this case, if the heat load is 55w and the maximum permissible operating temperature is less than 80°C, then the optimum refrigerant load is 22gr since a lower load means a higher temperature (92°C). Table 5.5 shows the numerical values of this analysis.

Table 5.5: Effect of the thermal load on the temperature of the LHP operation. Methanol as refrigerant

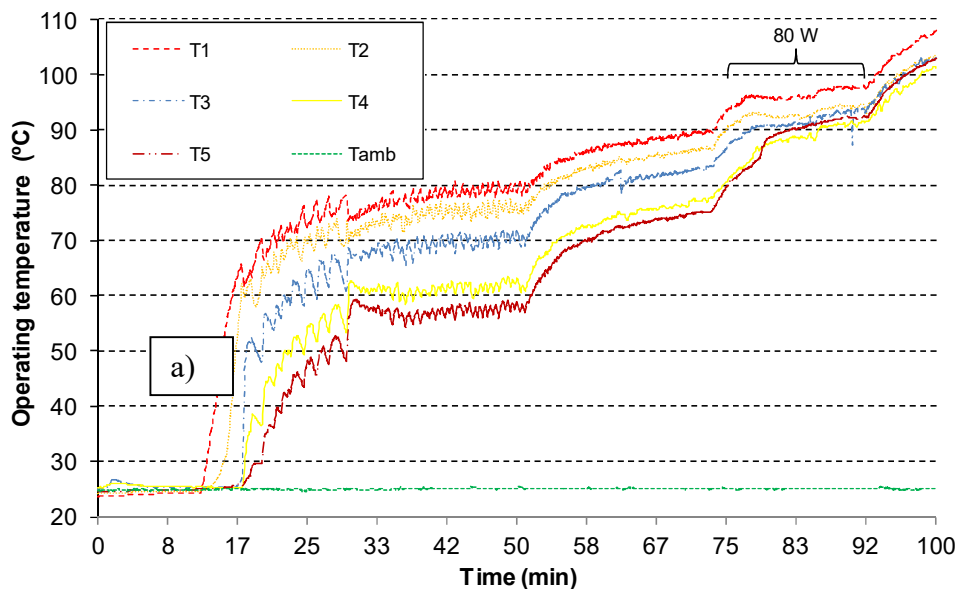
Heat Load (W)	Operating temperature (°C)	
	Fluid charge 20 (gr)	Fluid charge 22(gr)
28	65	
40	77	75
50	84	
55	92	78
70		89
85		97.5

Since our heat load is higher, the mass of refrigerant introduced has been 22gr.

5.4.3- Condensation/ambient temperature.

Figure 5.15 shows the behaviour of the LHP when operates at different heat loads and for two condensing/ambient temperatures of 25°C, 5.15 a) and 35°C 5.15b).

The process carried out in this test is to start with low heat loads and stepwise increase the heat load once the steady state corresponding to the each one is reached. During this process the time evolution of the LHP's temperatures is recorded. As plotted in figure 5.15, although the start-up in one of the two condensing temperature conditions presents a different behavior, as discussed earlier in this chapter, the evolution is similar, an increase in heat load implies an increase in temperature. In the case of 80w heat load, it is observed that the operating temperature is lower for a higher condensing/ambient temperature (explained above in the chapter).



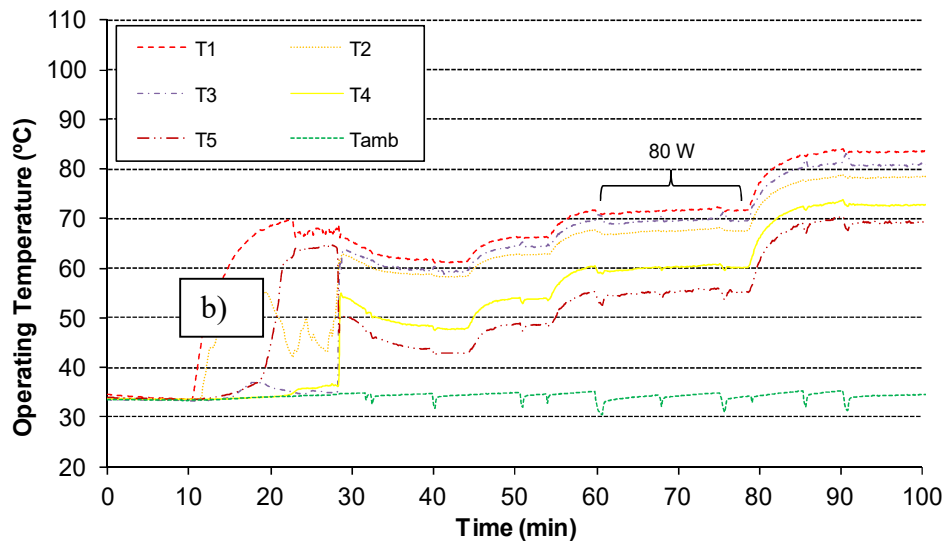


Figure 5.15: Temporal evolution of LHP temperatures; a) 25 ° C; b) 35 ° C.

In any case, the LHP operating temperature is lower at 35°C condensing temperature than it does at 25°C, figure 5.16.

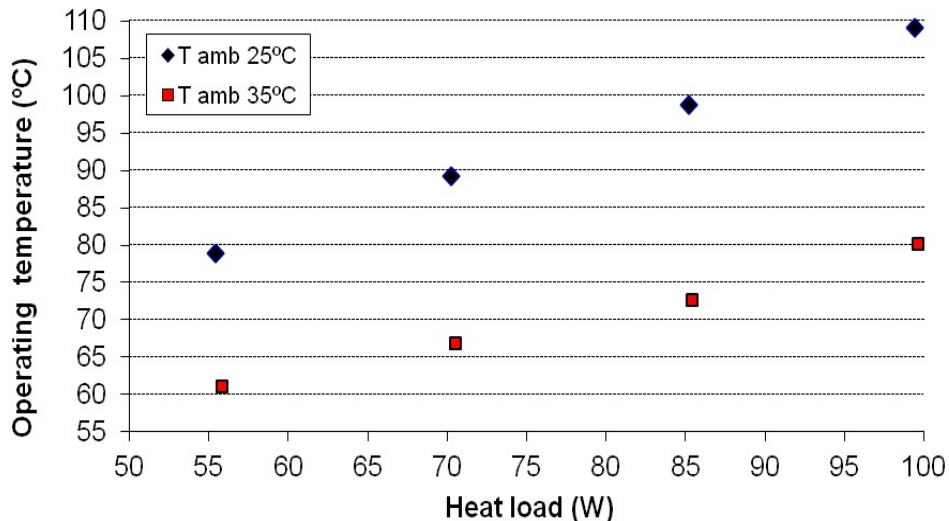


Figure 5.16: Evolution of the LHP operating temperature with the thermal load and the condensing temperature.

From figure 5.16, it is verified that operating temperature increase ratio is 0.66°C per thermal watt, 0.66°C/w, for the case of 25°C condensing temperature whereas it is 0.46°C/w for the case of 35°C condensing temperature. This shows that for high condensing temperatures this ratio is lower than for low condensing temperatures. These low temperatures of condensation cause a greater subcooling of the return liquid to the

compensation chamber. This, in turn, causes a greater thermal leakage of the evaporator towards the compensation chamber resulting in a lower evaporation flow and therefore an increase in the temperature in the evaporator [14].

However, the parameter that best defines the LHP goodness is its thermal resistance "R". This represents the required temperature difference between the subcooling and the operating temperature to extract 1 watt of heat.

$$R = \frac{T_e - T_c}{\dot{Q}}$$

The lower this thermal resistance, the better the LHP performance. These values are plotted in figure 5.17.

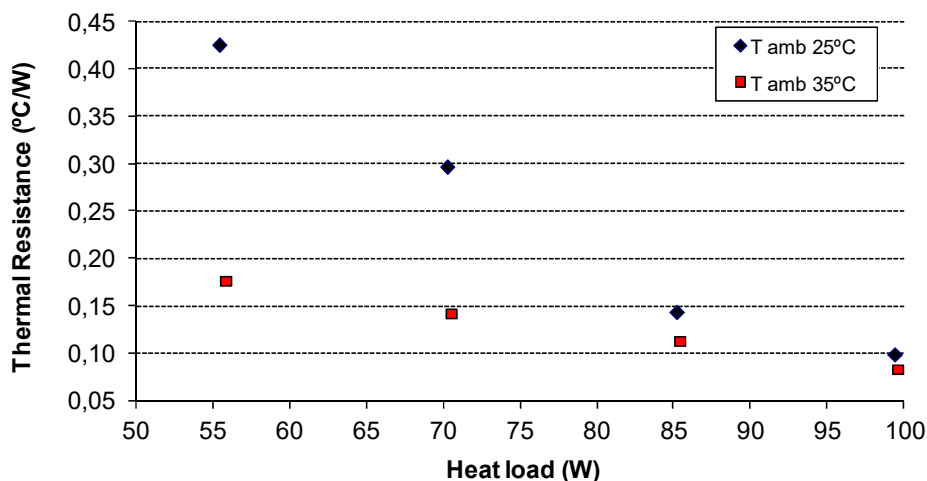


Figura 5.17: LHP thermal resistance as a function of heat load and condensing temperature

It is checked that the thermal resistance decreases as the thermal load increases regardless of the condensing temperature. Likewise, figure 5.17 plots that this thermal resistance is lower at higher condensing temperatures, nevertheless at high heat loads this thermal resistance is almost the same for both condensing temperatures.

5.5. Conclusions

- An LHP has been developed and tested, the primary wick of which has been developed using 3D laser printing technology, "SLM".
- Each of the LHP constituent elements (primary, secondary wick and refrigerant type) have been carefully analysed and tested in order to assess their appropriateness for the intended application (LED luminaire, 80w).
- The primary wick shows a good compatibility (wettability) with methanol as refrigerant, which is the one selected for the LHP. Likewise, the internal structural configuration shows suitable values: thermal conductivity, permeability, capillary pumping (compared to other manufacturing techniques).
- Regarding the secondary wick (wire mesh wound 3 turns), its refrigerant transport capacity and consequently its maximum length are determined. In this case, this length is well above the physical connection length between evaporator and compensation chamber.
- The results show an inverse relation between operating temperature and condensing temperature, the lower the condensing temperature, the higher the operating temperature. This is a consequence of the thermal contact between the evaporator and the C.C (thermal leakage to the compensation chamber); a less heat conductive contact would reduce this effect. Future work: new designs, new materials, ...
- The LHP thermal resistance decreases as the heat load increases, ie the LHP exhibits a better performance at high thermal loads (obviously if the increase in the evaporator temperature does not exceed the source's limit value). The value of this is $0.15^{\circ}\text{C} / \text{w}$.
- As far as the refrigerant charge is concerned, the allowed range of refrigerant charge is set for the LHP. The maximum and minimum load limits are determined according to safety and operating criteria.
- Within the allowable refrigerant charge range, it turns out that when the heat load is high the LHP behaves better with a higher refrigerant charge (lower

operating temperature). Also, when the thermal load is lower, then it is advisable to lower the refrigerant load. The refrigerant charge selected for the application is 22gr of methanol.

- Regarding the condensing temperatures, it turns out that the LHP tested here performs correctly for any of the two condensing temperatures. In both cases LED temperature (100°C) is below its limit temperature (125°C).
- It has been manufactured an LHP able to cool down a 80w LED (temperature below its limit value) working under any ambient temperature (within a range of temperatures) has been obtained. It presents a 10% improvement with respect to a similar LHP but with a powder sintering wick. SLM technology is interesting in terms of improving the LHP's operation (more efficient).

Bibliography

- [1] W. Joung, T. Yu, J. Lee, Experimental study on the loop heat pipe with a planar bifacial wick structure, *Int. J. Heat Mass Transf.* 51 (7–8) (2008) 1573–1581.
- [2] X. Huang, G. Franchi, Design and fabrication of hybrid bimodal wick structure for heat pipe application, *J. Porous Mater.* 15 (2008) 635–664.
- [3] J. Esarte, A. Bernardini, J.M. Blanco, R. Sancibrián, Optimizing the design for a two-phase cooling system Loop Heat Pipe; Part A: numerical model, characterization and validation procedure applied to a case study, *Appl. Therm. Eng.* 99 (2016) 892–904.
- [4] L.F. Berti, P.H.D. Santos, E. Bazzo, R. Janssen, D. Hotza, C.R. Rambo, Evaluation of permeability of ceramic wick structures for two phase heat transfer devices, *Appl. Therm. Eng.* 31 (6–7) (2011) 1076–1081.
- [5] D. Deng, Y. Tang, G. Huang, L. Lu, D. Yuan, Characterization of capillary performance of composite wicks for two-phase heat transfer devices, *Int. J. Heat Mass Transf.* 56 (1–2) (2013) 283–293.
- [6] G. Xin, K. Cui, Y. Zou, L. Cheng, Reduction of effective thermal conductivity for sintered LHP wicks, *Int. J. Heat Mass Transf.* 53 (13–14) (2010) 2932–2934.
- [7] R. Boubaker, V. Platel, Vapor pocket behavior inside the porous wick of a capillary pumped loop for terrestrial application, *Appl. Therm. Eng.* 84 (2015) 420–428.
- [8] F. Lin, B. Liu, C. Huang, Y. Chen, Evaporative heat transfer model of a loop heat pipe with bi-disperse wick structure, *Int. J. Heat Mass Transf.* 54 (21–22) (2011) 4621–4629.
- [9] Peter M. Dussinger, David B. Sarraf, and William G. Anderson, Loop Heat Pipe for TacSat-4 Space, Propulsion & Energy Sciences International Forum: SPESIF-2009. AIP Conference Proceedings, Volume 1103. AIP Conference Proceedings, Volume 1103, Issue 1, p.91-100.
- [10] S.C. Wu, D. Wang, J.H. Gao, Z.Y. Huang, Y.M. Chen, Effect of the number of grooves on a wick’s surface on the heat transfer performance of loop heat pipe, *Appl. Therm. Eng.* 71 (1) (2014) 371–377.
- [11] S. Launay, M. Vallée, State-of-the-art experimental studies on loop heat pipes, *Front. Heat Pipes (FHP)* 2 (2011) 013003.
- [12] B.H. Kim, G.P. Peterson, K.D. Kihm, Analytical and experimental investigation of entrainment in capillary pumped wicking structures, *J. Energy Resour.-ASME* 115 (1993) 278–286.
- [13] C.Y. Weng, T.S. Leu, Two-phase flow pattern based theoretical study of loop heat pipes, *Appl. Therm. Eng.* 98 (2016) 228–237

- [14] S. Wu, T. Gu, D. Wang, Y. Chen, Study of PTFE wick structure applied to loop heat pipe, *Appl. Therm. Eng.* 81 (25) (2015) 51–57.
- [15] C. Petit, B. Siedel, D. Gloriod, V. Sartre, F. Lefèvre, J. Bonjour, Adsorption-based antifreeze system for loop heat pipes, *Appl. Therm. Eng.* 78 (5) (2015) 704–771.

Chapter 6- Conclusions-Future works

6.1-Conclusions.....	124
6.2-Future works	127

6.1-Conclusions

- Nowadays, electronics evolves towards smaller devices and components with greater operation capacity and so with greater heat generation (heat density). This heat increase together with components miniaturization make cooling needs increase and therefore their power consumption. At present, temperature is the limiting factor in the miniaturization of electronic components. That is why thermal management research is going to more efficient and smaller cooling systems able to fulfil current needs of the electronics. As an illustrative example of the weight of cooling system's power consumption over total operating power consumption, the EMERSON's study is shown, **figure C.1.** 38% of power consumption is used by the cooling system.

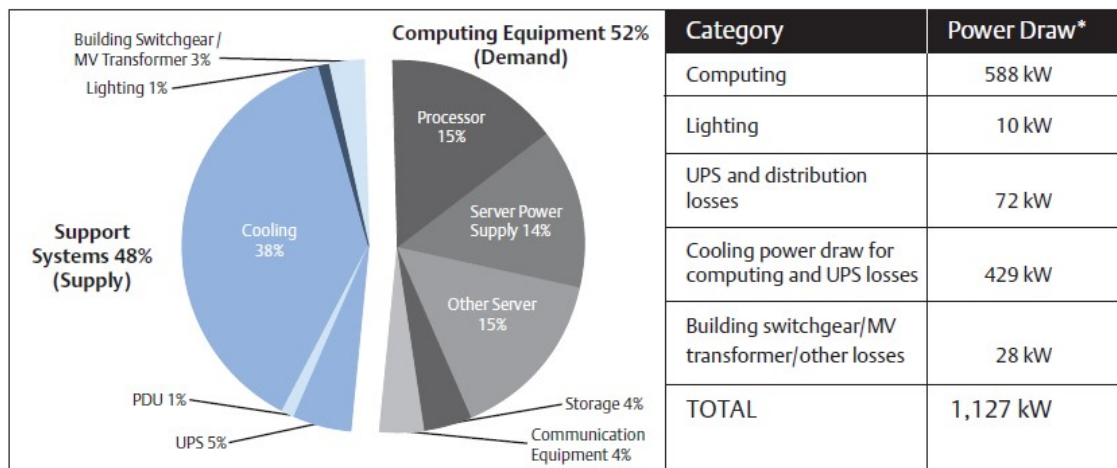


Figure C.1.: Thermal analysis of a 450m2 data centre (Courtesy of EMERSON)

- The same study shows that a reduction of the components electrical consumption by 1W leads to 2.84W reduction in the overall consumption of the high computing centre. However, reducing 1W the component power consumption requires, among other things, the heat extraction to be as efficient as possible in order to keep the component's operating temperature as low as possible. For example, in a thermoelectric module a temperature drop reduction means a conversion power increase; regarding LED lighting it means light quality improvement.
- One of the cooling technologies aligned with the above needs (more efficient and reduced size) are the Loop Heat Pipes "LHP", an evolution of the traditional "HPs", Heat Pipes. These have got a high cooling capacity while presenting a very small

size. Thus, preventing the constriction thermal resistance that appears in conventional cooling systems due to the heat re-routing from the source to the heatsink.

- LHPs are passive elements, whose functionality falls on: a porous element "wick" which pumps the refrigerant at the speed that the application requires (heat evacuation) and a refrigerant (maintains the operating temperature taking advantage of its change of phase), among others, to avoid heat source overheating.
- Wick performance is characterized by: load curve and permeability, basically. Depending on the technology used these porous media structure varies and consequently its functionality. After comparing the results obtained for different manufacturing technologies, it turns out that the manufacturing process by 3D laser printing, "SLM", provides the best wick performance, consequently is the method used to manufacture the LHP primary wick. Pumping capacity is 15%, 20% and 200% higher than that for copper sintering, meshes and foams respectively. As regards permeability and for a constant porosity of 60%, the wick made by SLM presents a permeability 8% higher than that of the foam and well above that of the sinter.
- A LHP's stationary numerical model has been developed together with a mathematical definition of the heat transfer coefficient towards the compensation chamber. Coefficient that allows to determine, depending on the geometric design and materials, the thermal leakage from the evaporator to the compensation chamber unlike most of the static models that consider this parameter a value manually introduced by the user what requires the a deep thermal knowledge by him. The model developed here does not require any knowledge on these subjects by the user, since this is implicitly calculated by the model in function of purely geometric and operational parameters, giving it a greater simplicity of handling.
- Model validation shows a very good correspondence with the experimental values (less than 4% of drift) and therefore its validity to be used in the LHP's stationary state design.

- Thanks to the model, it can be checked the effect of certain parameters on the LHP's operating temperature, in this sense:
 - ✓ Both the condensing temperature and the vapour line length directly affect the operating temperature, ie as they increase, so does the operating temperature.
 - ✓ There is a pipe radius below which the operating temperature is inversely proportional to the pipe radius, ie if the radius increases the operating temperature decreases exponentially. However, from this radius, the temperature variation is almost zero.
 - ✓ Regarding the condensing temperature, the model detects an atypical behavior for condensing temperature values below a specific one. Value that depends on the geometric characteristics, materials and operating conditions (heat load). It turns out that, for values of condensing temperature below the singular one, a decrease in the condensing temperature supposes an increase in the operating temperature. This, in turn, is reflected in an increase in the percentage of the heat load leaking from the evaporator to the compensation chamber and thus a decrease in the cooling capacity.
- An LHP has been developed and tested, the primary wick of which has been developed using 3D laser printing technology, "SLM" (better performance than any other direct technology). Device, intended for the cooling of a LED luminaire (80w and maximum temperature 125°C).
- Regarding the secondary wick (wire mesh wound 3 turns), its refrigerant transport capacity and its maximum length are determined. In this case, this length is well above the connection length between compensation chamber and evaporator.
- The results show an inverse behaviour of the operating temperature with respect to the condensing temperature, the lower the condensing temperature the greater the operating temperature. This is a consequence of the LHP design (thermal

leakage to the compensation chamber); a less thermal conductive contact would reduce this effect. Future work: new designs, new materials, ...

- The LHP thermal resistance decreases as the heat load increases, ie the LHP exhibits a better performance at high heat loads (obviously if the increase in the evaporator temperature does not exceed the limit value of the source). This value is $0.15^{\circ}\text{C}/\text{w}$
- As far as the refrigerant charge is concerned, the allowed range of refrigerant charge is set for the LHP. The maximum and minimum load limits are determined according to safety and operating criteria.
- Within the allowable refrigerant charge range, it turns out that when the heat load is high the LHP works better (lower operating temperature) with a higher refrigerant charge. When heat load is low, then less coolant charge is advisable. The refrigerant charge selected for the application is 22gr of methanol.
- It has been manufactured an LHP able to cool down a 80w LED (temperature below its limit value) working under any ambient temperature (within a range of temperatures) has been obtained. It presents a 10% improvement with respect to a similar LHP but with a powder sintering wick. SLM technology is interesting in terms of improving the LHP's operation (more efficient).

6.2-Future works

- Improve the current steady state model to be able to simulate LHP with multiple-condensers. Increasingly, LHP applications require more than just one condensing zone to fulfil the varying operating conditions the application is subjected to.
- Develop a transient state LHP model from the current steady state model.
- Development and characterization of primary wick with multiple porosity to increase their capillary pumping capacities.

Thesis: Development of a Loop Heat Pipe “LHP”
thermal superconductor device with
multicondensers

UNIVERSIDAD PAIS VASCO
Dpto. INGENIERÍA MINERA Y METALÚRGICA
Y CIENCIA DE LOS MATERIALES

Annex 1-Nomenclature

T_c	Peltier pellet hot side temperature	[K]
T_F	Peltier pellet cold side temperature	[K]
I	Electric current	[Amper]
Q_P	“pn” junction heat	[W]
Q	Peltier pellet heat/cold	[W]
COP	Coefficient of Performance	
l	“p” or “n” semiconductor length	[m]
l_c	“pn” contact thick	[m]
Z	Figure of merit	[K ⁻¹]
P_{opt}	Power conversion of Peltier pellet	[W]
R	Electric resistance of Peltier pellet	[Ω]
r	Thermal conductivity ratio of a Peltier pellet	[W/m K]
n	Electric resistivity ratio of a Peltier pellet	[Ω•m]
ΔT	Temperature difference	[K]
\dot{Q}	Heat power	[W]
A	Heat exchanger base surface	[m ²]
A'	Heat source contact area	[m ²]
T	Temperature	[K]
R	Thermal resistance	[°C/W]
h	Convective heat transfer coefficient	[W/m ² K]
K	Thermal conductivity	[W/mK]
\vec{V}	Fluid velocity	[m/s]
ρ	Fluid density	[Kg/m ³]
C_p	Specific heat	[KJ/KgK]
C_E	Macroscopic inertial coefficient	[m ⁻¹]
\vec{u}	Darcy velocity	[m/s]
\vec{U}_p	Velocity at porous scale	[m/s]
P	Pressure	[Pa]
r	Pore radius	[m]

ΔP_C	Capillary pressure	[Pa]
g	Gravity	[m/s ²]
t	Time	[s]
m_c	Absorbed liquid mass	[Kg]
V	Volume	[m ³]
A_{fs}	Porous media wetted surface	[m ²]
K_K	Kozeny constant	dimensionless
n	Number of tubes	
d	Pore diameter	[m]
K	Permeability	[m ²]
D	Pipe diameter	[m]
LHP	Loop Heat Pipe	
G	Thermal conductance	[W/mK]
f	Friction coefficient	dimensionless
R_{ug}	Rugosity	dimensionless
ϕ	Wettability	
TC	Transport capacity	[W.m]

Greek Symbols

α_{ab}	Seebeck coefficient	[V/K]
π_{ab}	Peltier coefficient	[W/Amp]
λ	Semiconductor 's thermal conductivity	[W/mK]
λ_C	Thermal conductivity of “pn” contact	[W/mK]
ρ	Semiconductor's electric resistivity	[Ohms.m]
ρ_C	Electric resistivity of “pn” contact	[Ohms.m]
ε	Porosity	dimensionless
σ	Liquid surface tension	[N/m]
θ	Contact angle	[°]
τ	Tortuosity	dimensionless
μ	Fluid viscosity	[Pa.s]

Subscript

P	Peltier “pn” junction
F	Cold
amb	Ambient
int	Hot surrounding
frig	Refrigeration
base	Base
superf	Surface
conv	Convection
P	Porous scale
l	Liquid
v	Vapor
eff	Effective
s	Solid
e	Evaporator
mez	Fluid mixture (vapour + liquid)
x	Vapour quality
fric	Friction
c	Condenser
satPv	Saturation condition at Pv
e_cc	Evaporator-C.Chamber
w	Wick
cc	Compensation chamber
can	Grooves
λ	Evaporation at meniscus interface
sub	Sub-cooling
fa	2 nd wick heat leakage
v-l	Vapour-liquid interface
in	Inlet
out	Outlet
perd	Leak
Lf	Liquid line outlet

Annex 2-Figures

Chapter 1

- Figure 1.1: Moore law (page: 2)
- Figure 1.2: More than Moore law (page: 3)
- Figure 1.3: Seebeck effect (page: 4)
- Figure 1.4: Peltier effect (page: 5)
- Figure 1.5: Arrangement of semiconductors junctions type “p-n”. (page: 6)
- Figure 1.6: Effect of ΔT on both COP and cooling capacity of a thermoelectric pellet (page: 8)
- Figure 1.7: Open circuit voltage and maximum power for a typical TEG. (page: 8)
- Figure 1.8 Peltier pellet COP as a function of temperature difference between hot and cold heat dissipaters (page: 9)
- Figure 1.9: LED sketch (page: 10)
- Figure 1.10 Example of LED integration (page: 11)
- Figure 1.11 LED’s luminosity-optics decrease with temperature. (page: 11)

Figure 1.12 Estimated life for a Philips Luxeon K2 LED as a function of the temperature and for different power currents. Courtesy of Philips. (page: 12)

Figure 1.13: Sketch of a LED assembly (page: 13)

Figure 1.14: Thermal analysis of a 450m² data center. (page: 14)

Figure 1.15: Cascade effect of the component’s consumption reduction on the global consumption. (page: 14)

Figure 2.1: Temperature distribution on a “L” width heat sink base surface (page: 21)

Figure 2.2: Effect of eccentricity on the heat source temperature (page: 22)

Figure 2.3: Straight fins radiator drawing (page: 24)

Figure 2.4: Effect of fin spacing on thermal resistance and pressure loss. (page: 25)

Figure 2.5: Effect of fin thickness on thermal resistance and pressure loss. (page: 25)

Figure 2.6: Effect of fin height on thermal resistance and pressure loss. (page: 26)

Figure 2.7: Triangular fin’s dimensions used for analysis (page: 28)

Figure 2.8: Distribution of the temperature along the fin, from the base to the tip being W = 10mm. A) CFD case; B) Finstudy case. (page: 30)

Figure 2.9: Effect of fin width on efficiency. (page: 30)

Figure 2.10: Fin’s surface temperature; A) L = 50 mm; B) L = 70 mm; C) L = 100 mm. (page: 31)

Figure 2.11: Surface temperature distribution; A) rectangular fin, b) triangular fin. (page: 32)

- Figure 3.1: LHP scheme with detail of the location of the wicks or porous media. (page: 37)
- Figure 3.2: Wick performance (page: 38)
- Figure 3.3: Intermolecular forces. (page: 38)
- Figure 3.4: SEM image of an aluminium metallic foam. (page: 39)
- Figure 3.5: Image of stainless steel structures manufactures by SLM. (page: 39)
- Figure 3.6: Pressure variation with height (page: 43)
- Figure 3.7: Capillary pumping measurement equipment. (page: 45)
- Figure 3.8: Pumping curve for nickel powder sintering, 2.5 μ m diameter particles, 59% porosity, distilled water. (page: 46)
- Figure 3.9: Nickel-water adjustment curve. (page: 47)
- Figure 3.10: Porous media permeability equipment (page: 49)
- Figure 3.11: Linear relation of pressure loss with temperature (Darcy law) (page: 50)

Figure 3.12: Differences between the two types of silica gel using two different liquids: water and methanol. (page: 52)

Figure 3.13: a) forward slope " α "; b) forward slope " β "; c) percentage of descent of slope " α " with respect to slope " β ". (page: 54)

Figure 3.14: Detail of 60 μ m mesh, 160 μ m and 300 μ m pitch. (page: 54)

Figure 3.15: Mesh Sample (page: 55)

Figure 3.16: Pumping curve for stainless steel mesh of different pitch: 60, 200 and 300. (page: 55)

Figure 3.17: Drop the absorbed mass to increase pitch size. (page: 56)

Figure 3.18: Pumping curve for copper powder sintering. (page: 57)

Figure 3.19: Drop the absorbed mass to increase pore size (page: 57)

Figure 3.20: a) form of the escaffol; b) fine capillary, 90 μ m; c) thick capillary, 180 μ m.. (page: 58)

Figure 3.21: Pumping curve for scaffold of stainless steel and methanol for two sizes of capillary. (page: 58)

Figure 3.22: SLM compared to sintering for a similar pore size. (page: 59)

Figure 3.23: Darcy law for a 30ppi ceramic foam structure and water. (page: 60)

Figure 3.24: Permeability as function of pore size with water as fluid. (page: 61)

Figure 3.25: Darcy law for a 95 μ m pore size copper sintering. (page: 62)

Figure 3.26: Permeability versus pore size in a copper powder sintering, water as fluid
(page: 62)

Figure 3.27: Darcy law for a SLM escaffol of 90 μ m capillary. (page: 63)

Figure 3.28: Permeability versus capillary size of the Escaffol-SLM, water as fluid.
(page: 63)

Figure 3.29: Comparison of permeabilities for an identical pore size of approximately 90 μ m. (page: 64)

Figure 3.30: Comparison of permeabilities for an identical porosity 60% (page: 65)

Figure 4.1: LHP diagram showing the constituent elements. (page: 71)

Figure 4.2: General heat flux directions (page: 73)

Figure 4.3: Heat flux through the evaporator (page: 74)

Figure 4.4: Thermal conduction scheme. (page: 75)

Figure 4.5: Condensing process (page: 82)

Figure 4.6: Algorithm of calculation. (page: 83)

Figure 4.7: Some dimensions of the experimental LHP (page: 85)

Figure 4.8: Experimental test bench (page: 85)

Figure 4.9: Comparison between the predicted and experimental LHP operating temperature as a function of the heat load. 25°C condensing temperature. (page: 86)

Figure 4.10: Comparison between the predicted and experimental LHP operating temperature as a function of the condensing temperature. 60w heat load. (page: 86)

Figure 4.11: Pearson's correlation coefficient squared for both two trials. (page:87)

Figure 4.12: Dependence of operating temperature with radius, steam line length and wick thickness. (page: 88)

Figure 4.13: Operating temperature vs tube radius for a condensation temperature of $T_c = 20^\circ\text{C}$ for a length of steam pipe of a) $l_v = 0.1\text{m}$, b) $l_v = 0.2\text{m}$ and c) $l_v = 0.3\text{m}$. (page: 89)

Figure 4.14: Operating temperature vs condensing temperature, $L_v=0.2\text{m}$, $Q_L=60\text{w}$ (page: 90)

Figure 4.15: Operating temperature vs condensing temperature, critical radius = $1.5 \cdot 10^{-3}\text{m}$; $L_v=0.2\text{m}$ (page: 90)

Figure 4.16: Heat leak to the C Chamber vs condensing temperature. Pipe radius = $1.5 \cdot 10^{-3}\text{m}$ (page: 91)

Figure 4.17: Operating temperature vs tube radius for a tube length " $L_v = 0.2\text{m}$ " and condensing temperatures: a) $T_c = 10^\circ\text{C}$, b) $T_c = 20^\circ\text{C}$ and c) $T_c = 30^\circ\text{C}$. (page: 91)

Figure 4.18: Latent heat and leakage heat ($Q_L = 80\text{w}$) depending on the radius of the tube and the length of the vapor tube for three different condensing temperatures: a) $T_c = 10^\circ\text{C}$, b) $T_c = 20^\circ\text{C}$ and c) $T_c = 30^\circ\text{C}$ (page: 93)

Figure 5.1: SLM 3D additive process. Courtesy of LORTEK (page: 100)

Figure 5.2: a) Primary kick external appearance, b) internal passages (page: 100)

Figure 5.3: Porous media permeability equipment (page: 101)

Figure 5.4: Pressure/Velocity curve for the 90 μ m escaffol (page: 102)

Figure 5.5: Drop evolution. a) drop of water after 1 minute; b) acetone drop after 1 second; c) methanol drop after 1 second. (page: 103)

Figure 5.6: A) water rise after 5 minutes) acetone rise after 1 second; C) methanol rise after 1 second. (page: 104)

Figure 5.7: Liquid rise curve (page: 104)

Figure 5.8: Thermal conductivity equipment (page: 106)

Figure 5.9: Stainless steel mesh image (page: 107)

Figure 5.10: Temperature drop in the primary wick because of thermal imbalance. (page: 108)

Figure 5.11: “TC” test for the secondary wick (page: 108-109)

Figure 5.12: LHP test bench (page: 110)

Figure 5.13: Start at 35°C ambient for different thermal loads: a) 57 W; b) 120 W.
(page: 112-113)

Figure 5.14: Operating temperature as a function of thermal load and the refrigerant charge.
(page: 115)

Figure 5.15: Temporal evolution of LHP temperatures; a) 25 ° C; b) 35 ° C.
(page: 116-117)

Figure 5.16: Evolution of the LHP operating temperature with the thermal load and the condensing temperature. (page: 117)

Figure 5.17: LHP thermal resistance as a function of heat load and condensing temperature (page: 118)

Annex 3-Tables

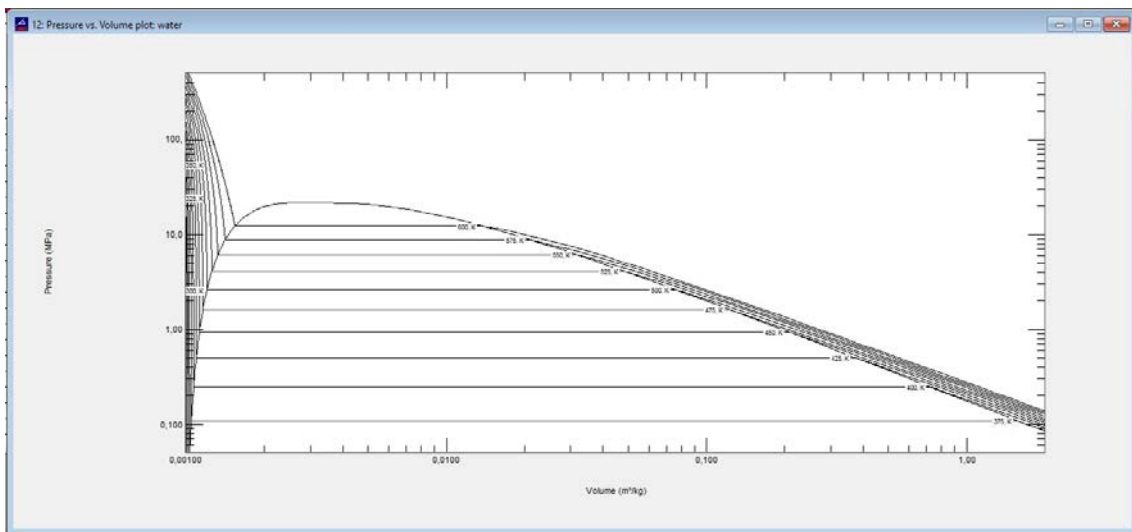
<u>Table 1.1: Physical properties of a commercial Peltier pellet</u>	(page: 8)
<u>Table 2.1: Fin length effect on the heat dissipation</u>	(page: 31)
<u>Table 3.1: Properties of Silica gel sheets.</u>	(page: 51)
<u>Table 3.2: Metallic mesh characteristics.</u>	(page: 54)
<u>Table 3.3: Characteristics of sintered powder copper samples</u>	(page: 56)
<u>Table 3.4: Pore size and porosity of 30, 40, 50 and 80 ppi foams</u>	(page: 60)
<u>Table 4.1: Input data</u>	(page: 84)
<u>Table 4.2: Geometric characteristics of LHP's prototype.</u>	(page: 84)
<u>Table 4.3: Combination of parameters allowing $T_e < 70^\circ \text{C}$.</u>	(page: 92)
<u>Table 5.1: Technical specifications for the 280 HL printer.</u>	(page: 99)
<u>Table 5.2: Wick's contact angles for three liquids.</u>	(page: 105)
<u>Table 5.3: Characteristics of the equipment.</u>	(page: 111)
<u>Table 5.4: Characteristics of the LHP's components.</u>	(page: 111)

Table 5.5: Effect of the thermal load on the temperature of the LHP operation. Methanol
as refrigerant. (page: 115)

Annex 4-Refrigerants properties

A4.1 Thermodynamic properties of Water

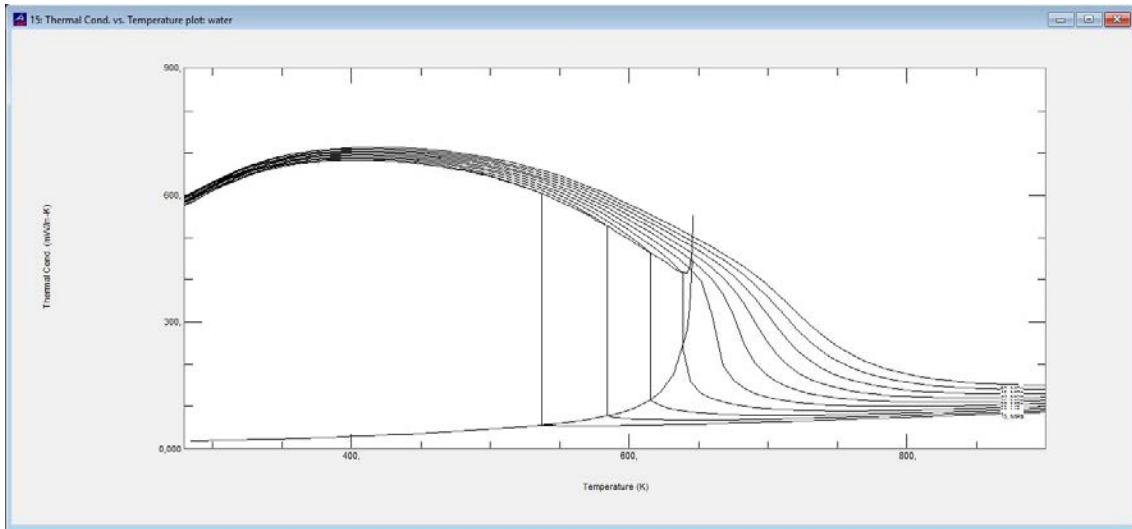
P-V diagram



Saturation properties as a function of temperature

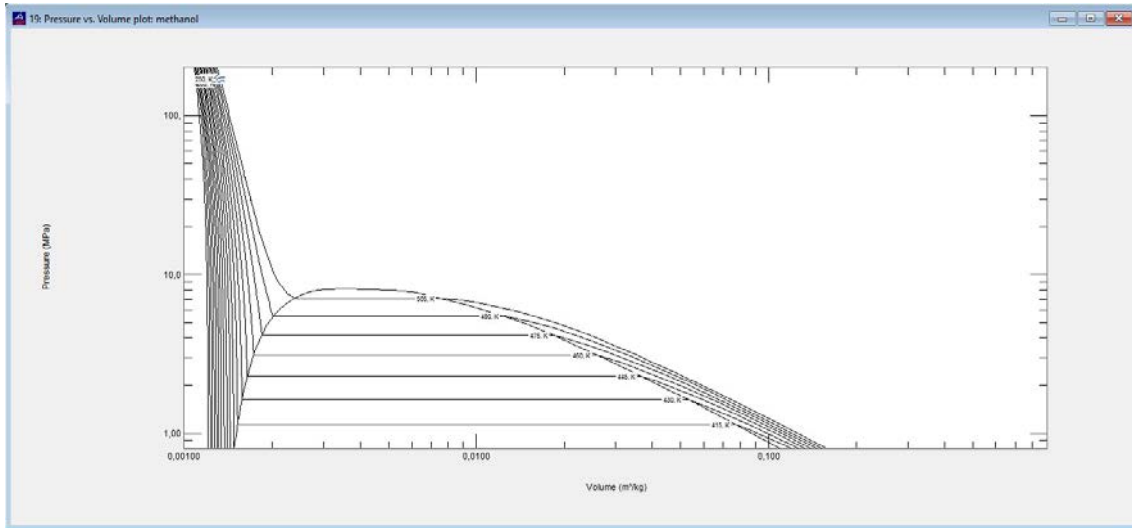
	Temperature (K)	Pressure (MPa)	Liquid Density (kg/m³)	Vapor Density (kg/m³)	Liquid Enthalpy (kJ/kg)	Vapor Enthalpy (kJ/kg)	Liquid Cp (kJ/kg-K)	Vapor Cp (kJ/kg-K)	Liquid Viscosity (μPa-s)	Vapor Viscosity (μPa-s)	Surf. Tension (mN/m)
1	275.00	0.00069845	999.89	0.0055066	7.7597	2504.3	4.2139	1.8862	1682.0	9.2596	75.388
2	280.00	0.00099182	999.86	0.0076812	28.796	2513.4	4.2014	1.8913	1433.7	9.3815	74.677
3	285.00	0.0013890	999.47	0.010571	49.780	2522.6	4.1927	1.8967	1239.3	9.5090	73.951
4	290.00	0.0019200	998.76	0.014363	70.729	2531.7	4.1869	1.9023	1084.0	9.6414	73.210
5	295.00	0.0026212	997.76	0.019281	91.654	2540.8	4.1832	1.9081	957.87	9.7784	72.455
6	300.00	0.0035368	996.51	0.025590	112.56	2549.9	4.1809	1.9141	853.84	9.9195	71.686
7	305.00	0.0047193	995.03	0.033598	133.47	2558.9	4.1798	1.9204	766.95	10.064	70.903
8	310.00	0.0062311	993.34	0.043663	154.37	2567.9	4.1795	1.9270	693.54	10.213	70.106
9	315.00	0.0081451	991.46	0.056195	175.27	2576.8	4.1798	1.9341	630.91	10.364	69.295
10	320.00	0.010546	989.39	0.071662	196.17	2585.7	4.1807	1.9417	577.02	10.518	68.470
11	325.00	0.013531	987.15	0.090590	217.08	2594.6	4.1821	1.9499	530.29	10.675	67.632
12	330.00	0.017213	984.75	0.11357	238.00	2603.3	4.1838	1.9587	489.49	10.833	66.781
13	335.00	0.021718	982.20	0.14127	258.93	2612.1	4.1860	1.9684	453.64	10.994	65.917
14	340.00	0.027188	979.50	0.17440	279.87	2620.7	4.1885	1.9790	421.97	11.157	65.040
15	345.00	0.033783	976.67	0.21378	300.82	2629.3	4.1913	1.9906	393.85	11.321	64.150
16	350.00	0.041682	973.70	0.26029	321.79	2637.7	4.1946	2.0033	368.77	11.487	63.248
17	355.00	0.051080	970.61	0.31487	342.78	2646.1	4.1983	2.0173	346.30	11.654	62.333
18	360.00	0.062194	967.39	0.37858	363.79	2654.4	4.2024	2.0326	326.10	11.823	61.406
19	365.00	0.075260	964.05	0.45253	384.82	2662.5	4.2070	2.0493	307.87	11.992	60.467
20	370.00	0.090535	960.59	0.53792	405.88	2670.6	4.2122	2.0676	291.36	12.162	59.517
21	375.00	0.10830	957.01	0.63605	426.97	2678.5	4.2178	2.0877	276.36	12.332	58.555
22	380.00	0.12885	953.33	0.74830	448.09	2686.2	4.2241	2.1096	262.69	12.504	57.581

Thermal conductivity vs temperature



A4.2 Thermodynamic properties of Methanol

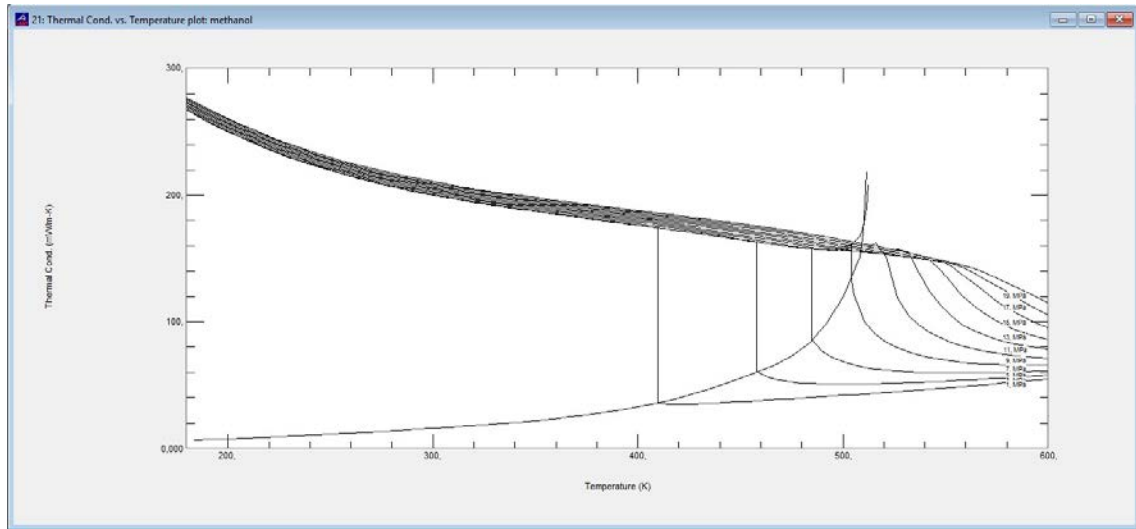
P-V diagram



Saturation properties as a function of temperature

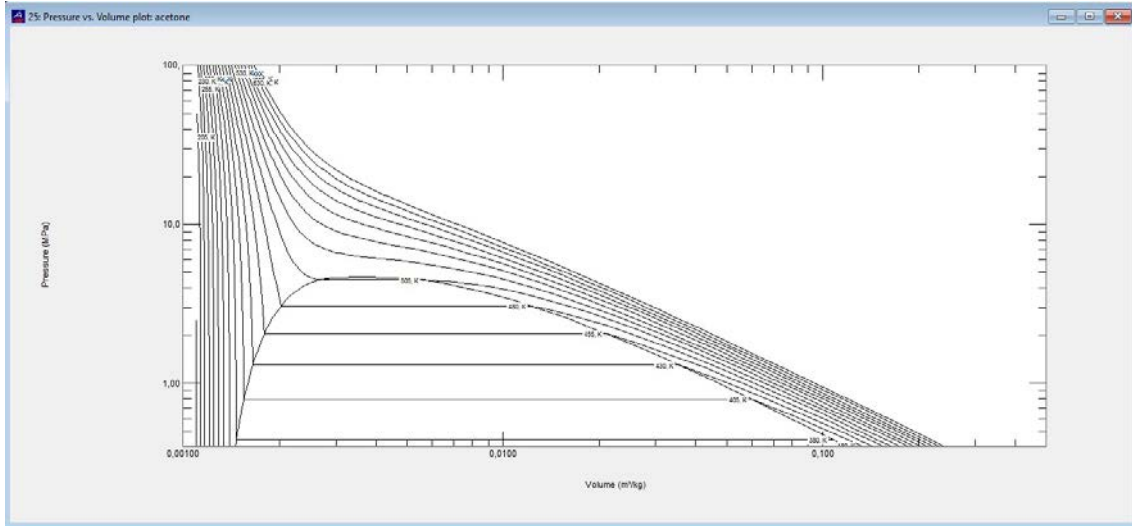
	Temperature (K)	Pressure (MPa)	Liquid Density (kg/m³)	Vapor Density (kg/m³)	Liquid Enthalpy (kJ/kg)	Vapor Enthalpy (kJ/kg)	Liquid Cp (kJ/kg-K)	Vapor Cp (kJ/kg-K)	Liquid Viscosity (μPa-s)	Vapor Viscosity (μPa-s)	Surf. Tension (mN/m)
1	250.00	0.00081030	831.52	0.012577	-221.69	1013.1	2.3121	2.3704	1236.5	8.1123	26.352
2	255.00	0.0011791	826.76	0.017964	-210.09	1018.6	2.3287	2.5009	1120.4	8.2691	25.908
3	260.00	0.0016889	822.03	0.025270	-198.40	1024.0	2.3467	2.6339	1018.8	8.4260	25.471
4	265.00	0.0023834	817.31	0.035039	-186.62	1029.3	2.3661	2.7680	929.37	8.5830	25.038
5	270.00	0.0033166	812.60	0.047933	-174.74	1034.6	2.3871	2.9024	850.48	8.7401	24.611
6	275.00	0.0045545	807.91	0.064742	-162.75	1039.8	2.4096	3.0359	780.59	8.8971	24.188
7	280.00	0.0061769	803.23	0.086401	-150.64	1045.0	2.4336	3.1677	718.46	9.0539	23.768
8	285.00	0.0082787	798.55	0.11401	-138.40	1050.1	2.4593	3.2970	663.07	9.2106	23.350
9	290.00	0.010972	793.87	0.14884	-126.04	1055.2	2.4867	3.4230	613.53	9.3669	22.935
10	295.00	0.014390	789.19	0.19235	-113.53	1060.3	2.5156	3.5454	569.09	9.5227	22.521
11	300.00	0.018682	784.51	0.24623	-100.87	1065.3	2.5461	3.6638	529.12	9.6780	22.107
12	305.00	0.024026	779.81	0.31237	-88.057	1070.2	2.5783	3.7780	493.05	9.8327	21.693
13	310.00	0.030621	775.08	0.39291	-75.077	1075.2	2.6120	3.8880	460.43	9.9865	21.278
14	315.00	0.038692	770.34	0.49025	-61.923	1080.0	2.6472	3.9940	430.83	10.140	20.862
15	320.00	0.048494	765.56	0.60706	-48.588	1084.8	2.6840	4.0962	403.91	10.291	20.443
16	325.00	0.060310	760.74	0.74629	-35.063	1089.5	2.7223	4.1950	379.35	10.442	20.022
17	330.00	0.074453	755.88	0.91122	-21.342	1094.2	2.7621	4.2911	356.89	10.592	19.598
18	335.00	0.091270	750.97	1.1054	-7.4162	1098.7	2.8034	4.3850	336.30	10.740	19.169
19	340.00	0.11114	746.00	1.3329	6.7217	1103.2	2.8462	4.4777	317.37	10.887	18.736
20	345.00	0.13447	740.96	1.5979	21.079	1107.5	2.8904	4.5701	299.91	11.032	18.299
21	350.00	0.16172	735.84	1.9053	35.664	1111.6	2.9362	4.6631	283.78	11.175	17.855
22	355.00	0.19337	730.65	2.2601	50.484	1115.6	2.9835	4.7580	268.84	11.317	17.406
23	360.00	0.22992	725.36	2.6681	65.547	1119.4	3.0324	4.8559	254.95	11.457	16.951
24	365.00	0.27195	719.97	3.1354	80.861	1123.1	3.0829	4.9582	242.03	11.595	16.488
25	370.00	0.32004	714.47	3.6688	96.434	1126.4	3.1351	5.0664	229.96	11.731	16.019
26	375.00	0.37483	708.86	4.2757	112.27	1129.6	3.1891	5.1821	218.66	11.866	15.542
27	380.00	0.43697	703.11	4.9644	128.39	1132.4	3.2450	5.3070	208.06	11.998	15.056
28	385.00	0.50717	697.22	5.7440	144.80	1134.9	3.3030	5.4429	198.10	12.129	14.563
29	390.00	0.58617	691.18	6.6244	161.49	1137.1	3.3632	5.5918	188.71	12.258	14.061
30	395.00	0.67476	684.98	7.6170	178.50	1139.0	3.4258	5.7556	179.84	12.386	13.550
31	400.00	0.77374	678.59	8.7343	195.83	1140.4	3.4912	5.9366	171.43	12.512	13.031
32	405.00	0.88399	672.01	9.9905	213.48	1141.3	3.5595	6.1366	163.46	12.638	12.502
33	410.00	1.0064	665.22	11.401	231.48	1141.8	3.6312	6.3572	155.88	12.763	11.964
34	415.00	1.1419	658.20	12.985	249.84	1141.8	3.7067	6.5991	148.65	12.888	11.417
35	420.00	1.2914	650.93	14.762	268.58	1141.3	3.7865	6.8616	141.75	13.014	10.861

Thermal conductivity vs temperature



A4.3 Thermodynamic properties of Acetone

P-V diagram

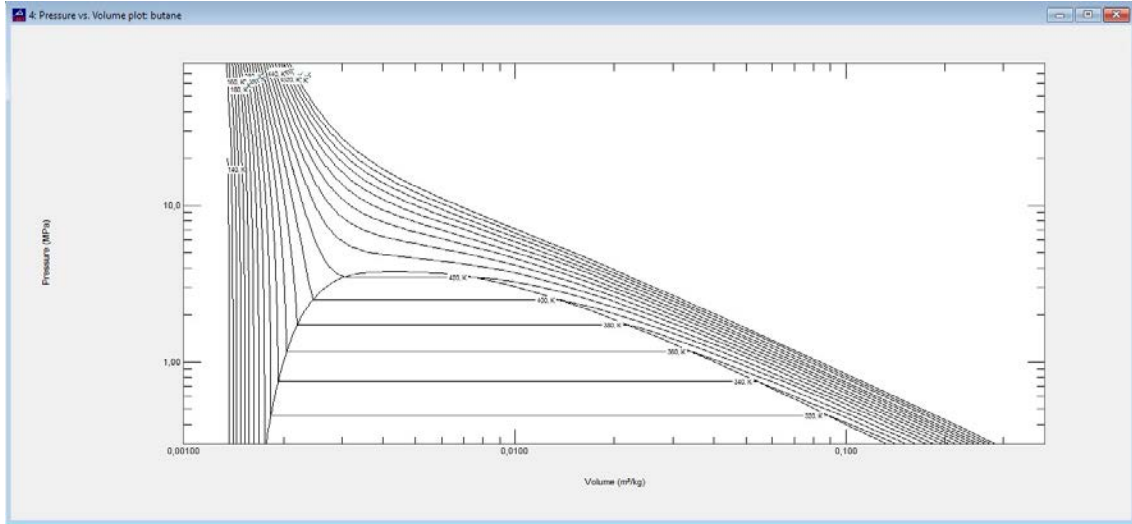


Saturation properties as a function of temperature

	Temperature (K)	Pressure (MPa)	Liquid Density (kg/m³)	Vapor Density (kg/m³)	Liquid Enthalpy (kJ/kg)	Vapor Enthalpy (kJ/kg)	Liquid Cp (kJ/kg-K)	Vapor Cp (kJ/kg-K)	Liquid Viscosity (μPa-s)	Vapor Viscosity (μPa-s)	Surf. Tension (mN/m)
1	250.00	0.0023819	836.94	0.066908	-168.69	412.24	2.0494	1.1833	No equation	No equation	29.816
2	255.00	0.0032765	831.61	0.090341	-158.43	417.78	2.0568	1.2012	No equation	No equation	29.090
3	260.00	0.0044428	826.26	0.12031	-148.12	423.34	2.0648	1.2200	No equation	No equation	28.368
4	265.00	0.0059437	820.90	0.15816	-137.78	428.92	2.0733	1.2397	No equation	No equation	27.650
5	270.00	0.0078514	815.51	0.20541	-127.39	434.52	2.0824	1.2603	No equation	No equation	26.935
6	275.00	0.010249	810.10	0.26379	-116.95	440.13	2.0920	1.2818	No equation	No equation	26.224
7	280.00	0.013230	804.66	0.33518	-106.46	445.76	2.1021	1.3042	No equation	No equation	25.518
8	285.00	0.016899	799.19	0.42167	-95.921	451.39	2.1127	1.3274	No equation	No equation	24.815
9	290.00	0.021373	793.68	0.52556	-85.327	457.04	2.1238	1.3515	No equation	No equation	24.116
10	295.00	0.026779	788.14	0.64931	-74.674	462.69	2.1355	1.3763	No equation	No equation	23.422
11	300.00	0.033259	782.56	0.79564	-63.962	468.35	2.1477	1.4020	No equation	No equation	22.731
12	305.00	0.040964	776.93	0.96744	-53.186	474.02	2.1604	1.4285	No equation	No equation	22.045
13	310.00	0.050059	771.26	1.1678	-42.345	479.68	2.1736	1.4557	No equation	No equation	21.364
14	315.00	0.060720	765.54	1.4001	-31.435	485.34	2.1874	1.4837	No equation	No equation	20.687
15	320.00	0.073136	759.76	1.6678	-20.455	491.00	2.2016	1.5124	No equation	No equation	20.014
16	325.00	0.087505	753.93	1.9748	-9.4002	496.66	2.2164	1.5419	No equation	No equation	19.346
17	330.00	0.10404	748.03	2.3251	1.7307	502.30	2.2318	1.5720	No equation	No equation	18.683
18	335.00	0.12296	742.07	2.7230	12.941	507.93	2.2476	1.6029	No equation	No equation	18.024
19	340.00	0.14450	736.03	3.1730	24.233	513.55	2.2641	1.6346	No equation	No equation	17.371
20	345.00	0.16891	729.92	3.6800	35.610	519.15	2.2811	1.6671	No equation	No equation	16.722
21	350.00	0.19643	723.73	4.2492	47.075	524.72	2.2988	1.7003	No equation	No equation	16.079
22	355.00	0.22733	717.45	4.8862	58.630	530.27	2.3171	1.7345	No equation	No equation	15.441
23	360.00	0.26188	711.08	5.5969	70.280	535.79	2.3360	1.7696	No equation	No equation	14.808
24	365.00	0.30037	704.61	6.3877	82.027	541.27	2.3557	1.8057	No equation	No equation	14.181
25	370.00	0.34308	698.04	7.2655	93.875	546.71	2.3762	1.8429	No equation	No equation	13.560
26	375.00	0.39033	691.35	8.2378	105.83	552.09	2.3975	1.8813	No equation	No equation	12.944
27	380.00	0.44240	684.55	9.3127	117.89	557.43	2.4196	1.9212	No equation	No equation	12.334
28	385.00	0.49964	677.61	10.499	130.06	562.69	2.4428	1.9626	No equation	No equation	11.731
29	390.00	0.56235	670.53	11.807	142.35	567.89	2.4670	2.0058	No equation	No equation	11.134
30	395.00	0.63089	663.31	13.246	154.76	573.01	2.4924	2.0510	No equation	No equation	10.543
31	400.00	0.70559	655.92	14.830	167.30	578.03	2.5191	2.0986	No equation	No equation	9.9592

A4.3 Thermodynamic properties of Butane

P-V diagram

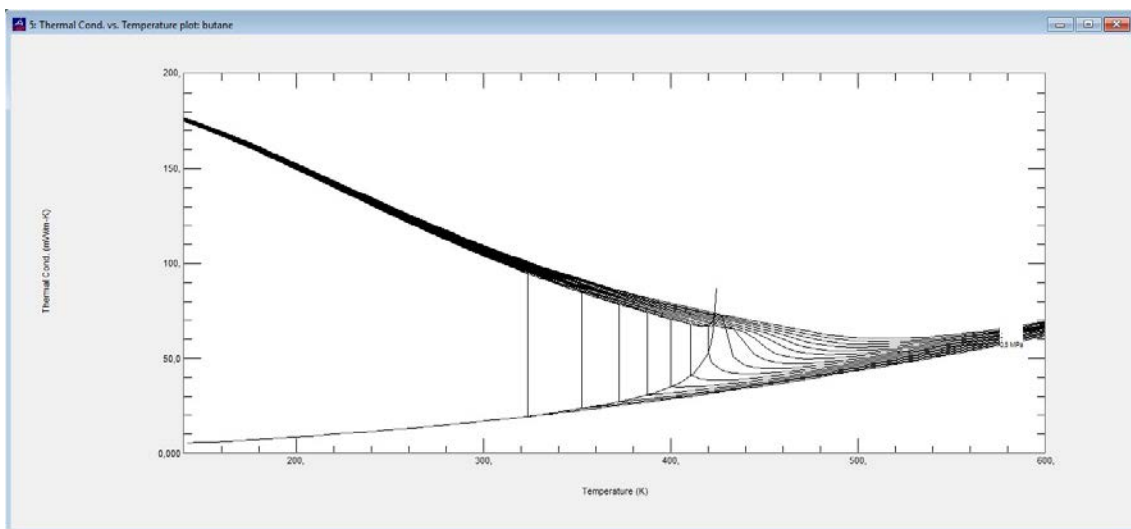


Saturation properties as a function of temperature

2: butane: V/L sat. T=240, to 420, K

	Temperature (K)	Pressure (MPa)	Liquid Density (kg/m ³)	Vapor Density (kg/m ³)	Liquid Enthalpy (kJ/kg)	Vapor Enthalpy (kJ/kg)	Liquid Entropy (kJ/kg-K)	Vapor Entropy (kJ/kg-K)	Liquid Cp (kJ/kg-K)	Vapor Cp (kJ/kg-K)	Liquid Viscosity (μPa-s)	Vapor Viscosity (μPa-s)	Surf. Tension (mN/m)
1	240,00	0,024086	635,06	0,71204	125,64	538,64	0,71046	2,4313	2,1765	1,4760	290,87	5,9664	19,007
2	245,00	0,030885	630,03	0,89706	136,57	545,58	0,75551	2,4249	2,1945	1,4989	274,41	6,0877	18,362
3	250,00	0,039153	624,95	1,1182	147,60	552,57	0,80001	2,4199	2,2133	1,5226	259,26	6,2087	17,723
4	255,00	0,049106	619,83	1,3802	158,72	559,58	0,84400	2,4160	2,2330	1,5472	245,27	6,3295	17,087
5	260,00	0,060978	614,65	1,6880	169,95	566,63	0,88753	2,4132	2,2536	1,5726	232,32	6,4502	16,457
6	265,00	0,075015	609,41	2,0470	181,29	573,70	0,93062	2,4114	2,2750	1,5989	220,31	6,5709	15,832
7	270,00	0,091481	604,11	2,4629	192,73	580,79	0,97330	2,4106	2,2974	1,6262	209,13	6,6919	15,211
8	275,00	0,11065	598,74	2,9416	204,29	587,91	1,0156	2,4106	2,3206	1,6543	198,71	6,8133	14,596
9	280,00	0,13282	593,29	3,4896	215,97	595,03	1,0576	2,4114	2,3447	1,6835	188,97	6,9353	13,986
10	285,00	0,15828	587,77	4,1136	227,78	602,17	1,0992	2,4129	2,3698	1,7137	179,85	7,0583	13,382
11	290,00	0,18734	582,17	4,8208	239,71	609,31	1,1406	2,4150	2,3959	1,7450	171,28	7,1826	12,783
12	295,00	0,22034	576,47	5,6190	251,78	616,44	1,1816	2,4178	2,4230	1,7775	163,23	7,3085	12,190
13	300,00	0,25760	570,68	6,5164	264,00	623,58	1,2225	2,4211	2,4512	1,8111	155,63	7,4364	11,603
14	305,00	0,29946	564,78	7,5218	276,35	630,69	1,2631	2,4248	2,4806	1,8461	148,46	7,5668	11,022
15	310,00	0,34628	558,77	8,6450	288,86	637,79	1,3035	2,4291	2,5112	1,8825	141,67	7,7001	10,447
16	315,00	0,39842	552,63	9,8962	301,52	644,87	1,3437	2,4337	2,5432	1,9205	135,22	7,8371	9,8783
17	320,00	0,45624	546,36	11,287	314,35	651,91	1,3837	2,4386	2,5766	1,9603	129,09	7,9782	9,3166
18	325,00	0,52012	539,95	12,830	327,34	658,90	1,4237	2,4439	2,6116	2,0020	123,25	8,1243	8,7618
19	330,00	0,59045	533,38	14,540	340,52	665,84	1,4635	2,4493	2,6485	2,0459	117,68	8,2761	8,2141
20	335,00	0,66761	526,63	16,431	353,87	672,72	1,5032	2,4550	2,6874	2,0923	112,34	8,4346	7,6738
21	340,00	0,75201	519,69	18,522	367,42	679,53	1,5429	2,4609	2,7287	2,1416	107,22	8,6007	7,1413
22	345,00	0,84406	512,55	20,834	381,18	686,24	1,5825	2,4668	2,7726	2,1941	102,30	8,7757	6,6169
23	350,00	0,94418	505,18	23,389	395,14	692,84	1,6222	2,4727	2,8197	2,2505	97,559	8,9610	6,1009
24	355,00	1,0528	497,55	26,216	409,34	699,32	1,6618	2,4787	2,8705	2,3115	92,76	9,1582	5,5938
25	360,00	1,1704	489,63	29,347	423,77	705,64	1,7015	2,4845	2,9259	2,3786	88,535	9,3692	5,0960
26	365,00	1,2974	481,38	32,822	438,47	711,78	1,7413	2,4901	2,9868	2,4534	84,220	9,5964	4,6081
27	370,00	1,4343	472,76	36,689	453,44	717,69	1,7813	2,4955	3,0548	2,5384	80,014	9,8425	4,1305
28	375,00	1,5816	463,72	41,007	468,72	723,35	1,8215	2,5005	3,1318	2,6372	75,900	10,111	3,6642
29	380,00	1,7399	454,17	45,851	484,33	728,69	1,8619	2,5050	3,2206	2,7544	71,859	10,407	3,2098
30	385,00	1,9098	444,03	51,321	500,32	733,65	1,9027	2,5088	3,3259	2,8969	67,872	10,736	2,7683
31	390,00	2,0918	433,17	57,546	516,74	738,15	1,9440	2,5117	3,4543	3,0753	63,914	11,107	2,3409
32	395,00	2,2868	421,41	64,709	533,67	742,06	1,9860	2,5136	3,6178	3,3069	59,958	11,532	1,9291
33	400,00	2,4954	408,48	73,077	551,22	745,21	2,0289	2,5139	3,8375	3,6228	55,964	12,027	1,5348
34	405,00	2,7187	393,97	83,062	569,58	747,34	2,0731	2,5120	4,1567	4,0855	51,875	12,624	1,1604
35	410,00	2,9578	377,13	95,371	589,06	748,00	2,1194	2,5071	4,6773	4,8403	47,596	13,373	0,80970
36	415,00	3,2142	358,45	111,41	610,32	746,30	2,1692	2,4969	5,7113	6,3233	42,937	14,383	0,48832
37	420,00	3,4897	327,77	135,00	635,19	738,88	2,2269	2,4761	8,8522	10,719	37,394	15,962	0,20707

Thermal conductivity vs temperature



Annex 5-Previous works

A5.1 Porous Media analysis	152
A5.1.1-Effect of wettability on heat conduction in a porous medium.....	152
A5.1.2-Capillary action	155
A5.2 Prototypes of two phase heat transfer devices.....	157
A5.2.1-Dimensions	157
A5.2.2-Real prototypes tests.....	160

A5.1 Porous Media analysis

A5.1.1-Effect of wettability on heat conduction in a porous medium

A previous step to the development of a two-phase heatsink has been the empirical measurement of the effect of having the porous medium wet or not on its temperature.

Two experiments were carried out on porous structures. These are:

- Wet porous media
- Dry porous media

Porous media materials are:

- 20 μ m diameter carbon fibre blanket arranged longitudinally and transversely.
- 20 μ m diameter glass fibre blanket arranged longitudinally and transversely.

Water is the wetting liquid used in the experiments.

In order to carry out such experiments, it was necessary to build a test bench that would allow monitoring of all parameters of interest: heat flow, temperatures, liquid level, etc,

...

Test bench consists of an electrical resistance embedded in a rectangular aluminum plate of dimensions 165x25x200mm and capable of supplying 800w power, figure A5.1.



Figure A5.1: Heat power source for the test bench

Tests methodology

First of all the input and output parameters are defined, table A5.1

Table A5.1: Test parameters

	Definition
Operating conditions	Heat power
	Material
	Water as wetting liquid
Output unknown	Height of liquid rise
	Sample’s Surface temperature
	Heater’s Surface temperature
	Ambient temperature

These tests intend to measure:

- Sample’s thermal resistance variation due to whether it is wetted or not.
- The influence of the liquid level on the sample's thermal resistance.

Test methodology is as follow:

- Placing the material (carbon or glass fiber) on an aluminum foil.
- Placing temperature probes along the sample surface.
- Placing the aluminum foil over the heater.
- Placing the bottom end of the aluminum foil into the liquid.
- Switching on the infrared camera and the heater and start measuring, figure A5.2

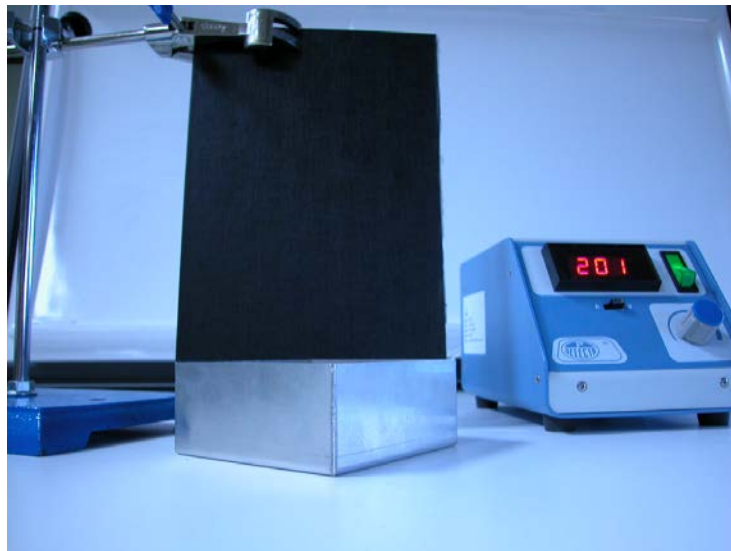


Figure A5.2: Test bench

Results

Wet or dry

For the carbon fibre sample, the result is plotted in figure A5.3.

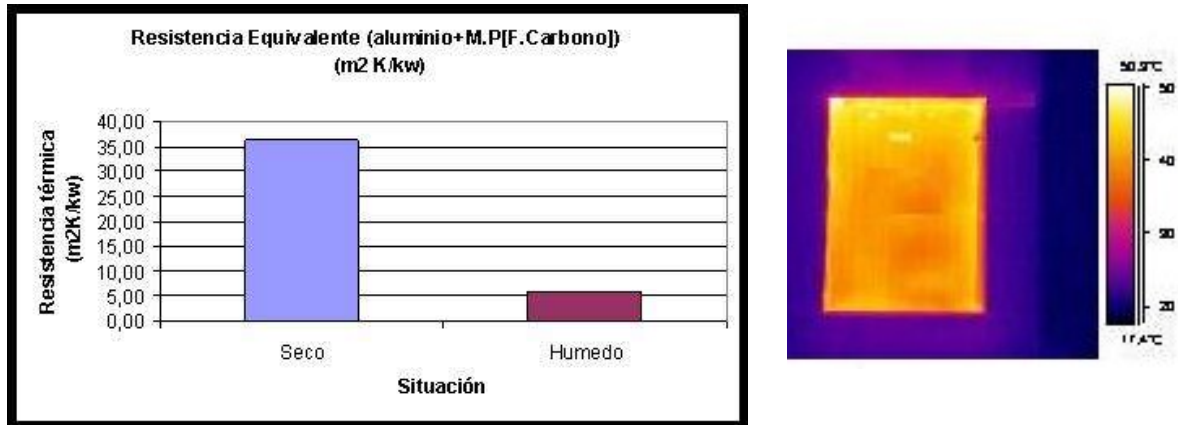


Figure A5.3: Sample thermal resistance and infrared image

For the following test conditions:

Heat power:	0,59 [Kw/m2]
Ambient temperature:	19 [°C]
Sample porosity:	52 [%]
Sample permeability:	5,25E-09 [m2]
Material:	3 layers carbon fibre

As expected (Fig. A5.3), the overall thermal resistance of the medium is considerably reduced (83.8%) compared to dry, which demonstrates its benefit as heat dissipation system.

Wet or dry

Under the same testing conditions, the effect of the height of liquid on the sample thermal resistance is plotted in figure A5.4.

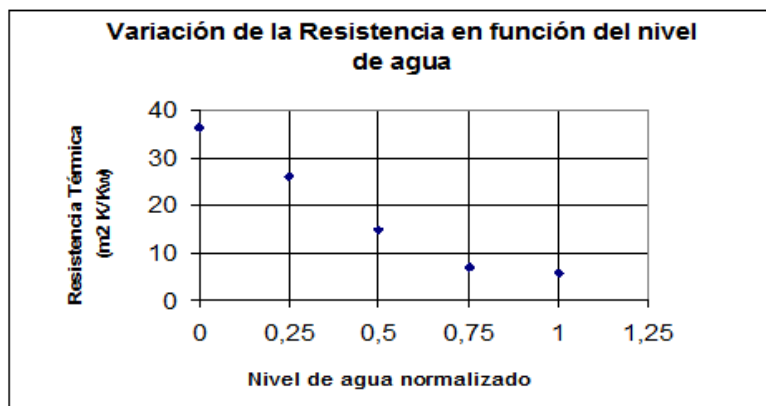


Figure A5.4: Height liquid effect on sample thermal resistance

As the liquid height increases, the sample thermal resistance decreases.

A5.1.2-Capillary action

Table A5.5 shows the maximum water height pumped by different porous media.

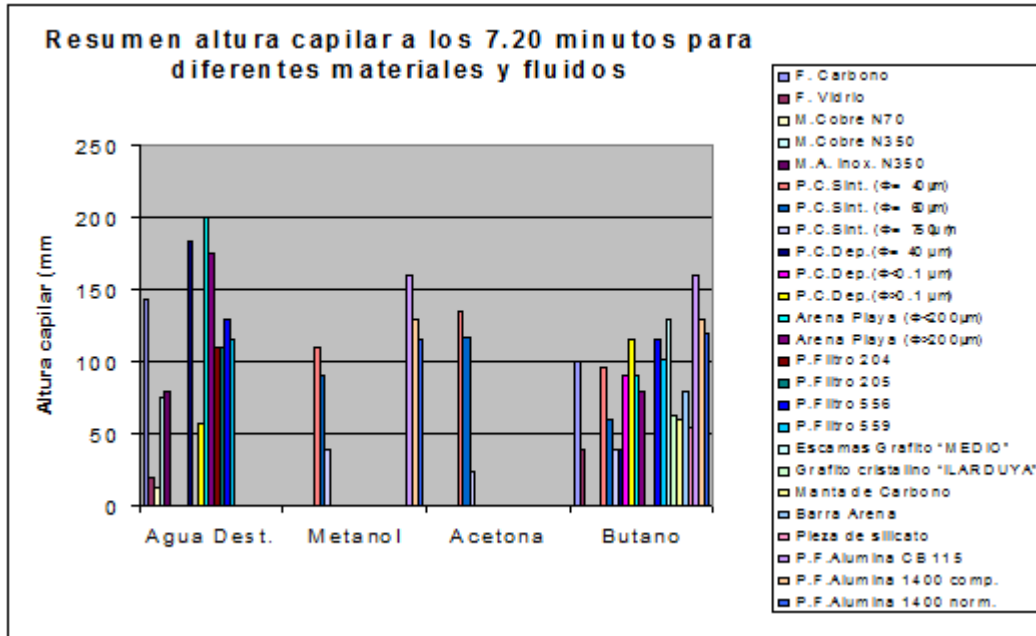


Figure A5.5: Water height for several porous media

The tested liquids area: wter, Methanol, Acetone and Butane. The porous media are:

Material	Characteristics
Carbon fibre (F.Carbono)	52% porosity, 3 layers
Glass fibre (F.Vidrio)	52% porosity, 3 layers
Copper mesh N70 (M.CobreN70)	0.232mm pitch, 41% open area
Copper mesh N350	0.022mm pitch, 25% oper area
Stainless steel mesh N350 (M.AInoxN350)	0.04mm pitch, 28% open area
Copper powder sintered 40 (P.C.Sint.40)	40 μm powder diameter
Copper powder sintered 60 (P.C.Sint.60)	60 μm powder diameter
Copper powder sintered 70 (P.C.Sint.75)	75 μm powder diameter
Copper powder deposeted 40(P.C.Dep.40)	40 μm powder diameter
Copper powder deposeted <0.1 (P.C.Dep.<0.1)	<0.1 μm powder diameter
Copper powder deposeted >0.1(P.C.Dep.>0.1)	>0.1 μm powder diameter
Beach sand <200 (arena de playa<200)	<200 μm powder diameter
Beach sand >200 (arena de playa>200)	>200 μm powder diameter
Filter 204 (P.Filtro204)	

Filter 205 (P.Filtro205)	
Filter 556 (P.Filtro556)	
Filter 559 (P.Filtro559)	
Bed of graphite flakes (Escamas de Grafito MEDIO)	
Crystalline graphite (Grafito cristalino)	
Carbon blanket	
Sand bar (Barra arena)	
Silicone (pieza de silicato)	
Alumina CB115 (P.F.Alumina Cb115)	
Alumina 1400 compound (P.F.Alumina 1400comp)	
Alumina 1400 normal (P.F.Alumina 1400norm)	

According to these results, water+<200µm beach sand is the combination that a higher liquid rise generates. It is also observed how important the combination material+liquid is. There are combinations that are not compatible at all as there is not liquid rise in them (not wetting combination). For the case of Metanol and Butane the Alumina CB115 presents a high liquid rise.

A5.2 Prototypes of two phase heat transfer devices

This prototype of two-phase heat transfer device aims to drive heat from a room to the Peltier pellet cold side, figure A5.6.

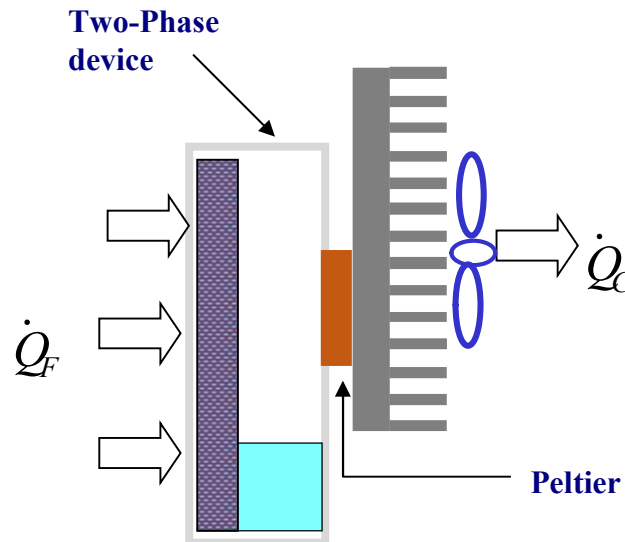


Figure A5.6: Prototype operation

A5.2.1-Dimensions

The following parameters are analysed prior defining the real prototype dimensions:

- **Height.** This data is given by the maximum height the different porous media can provide, section A5.1.2.
- **Width.** Although it could be thought that the wider the device is the greater the heat transfer (lower the thermal resistance) the reality is that this is not so due to the ratio of Peltier surface to the absorbent surface. This ratio generates the denominated resistance of constriction that is greater the smaller this quotient. After a short calculus a suitable width of 160mm is considered.
- **Length (internal gap of the device and wall thickness).** First of all, the wall thickness effect on the thermal resistance was analysed. Figure A5.7 shows temperature along the Peltier surface for three wall thicknesses: 2, 4 and 10mm. Data obtained by means of CFD simulations. It is observed that the thicker the wall the more unifor the temperature along the Peltier surface is. From this data and the temperature difference between absorbent surface and the Peltier surface the thermal resistance is calculated, figure A5.8.

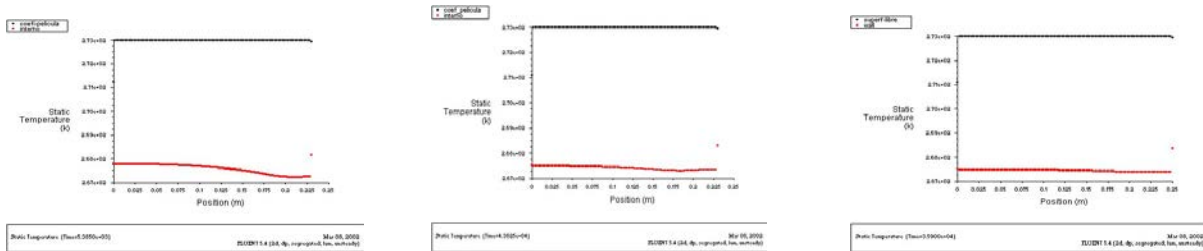


Figure A5.7: Temperature distribution along the Peltier surface, red line

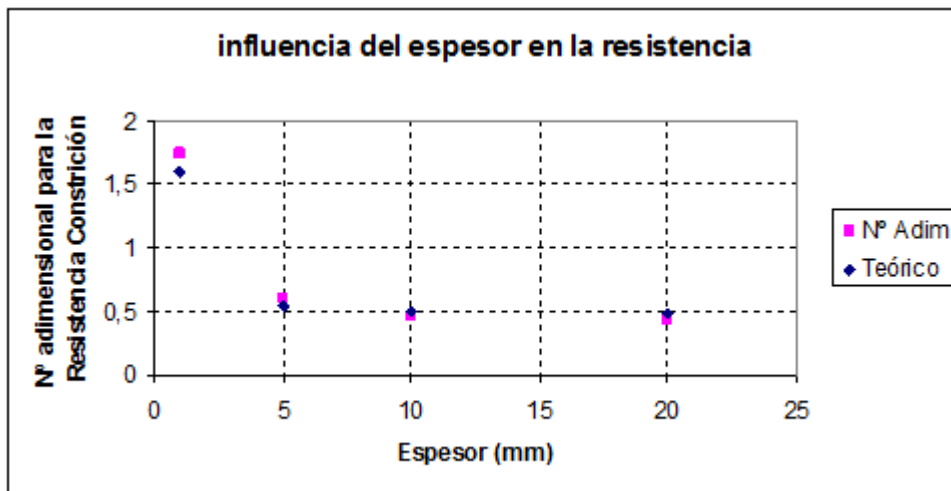


Figure A5.8: Thermal resistance versus wall thickness

From plot A5.8, it is concluded that the optimal value is close to 4-5mm.

Same simulations but varying (6 and 12 mm) the internal gap of the device are run with the results plotted in figure A5.9.

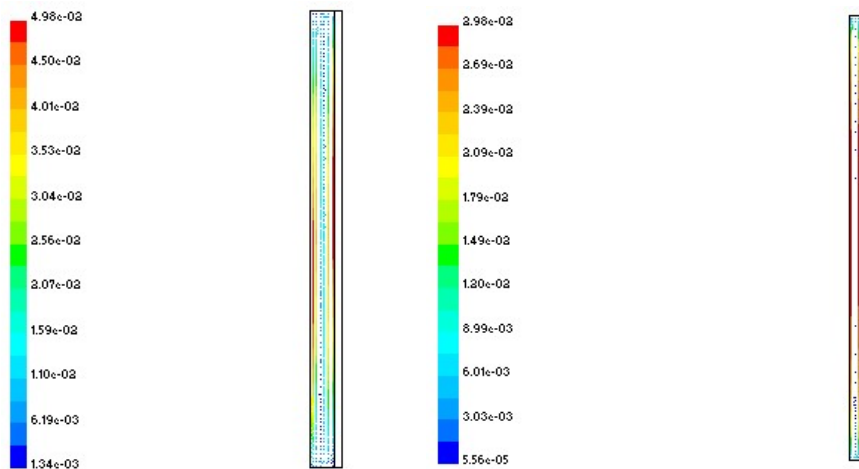


Figure A5.9: Vapour velocity inside the device for 12mm and 6mm gap respectively

Because this higher velocity for the 12mm gap, larger convective heat transfer coefficient, it is concluded that the optimal value for the gap is around 10-12mm

- Peltier position, eccentricity.

Until now, Peltier has been considered to be placed at the top, however is it the best position in terms of heat transfer resistance?. To answer this question a theoretical analysis is done. Upper and centre positions are studied with the results shown in figure A5.10.

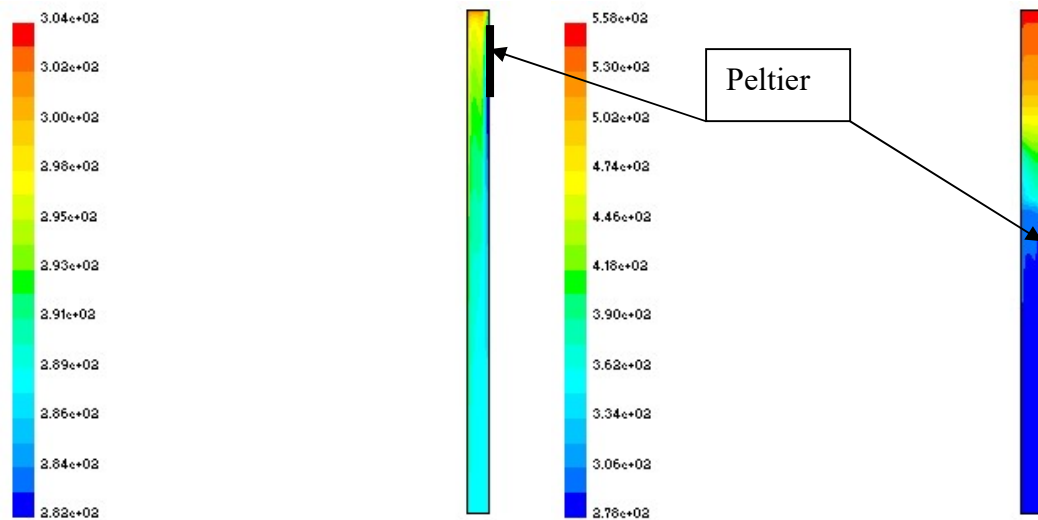


Figure A5.10: Temperature inside the device for the two Peltier positions, upper and centred respectively

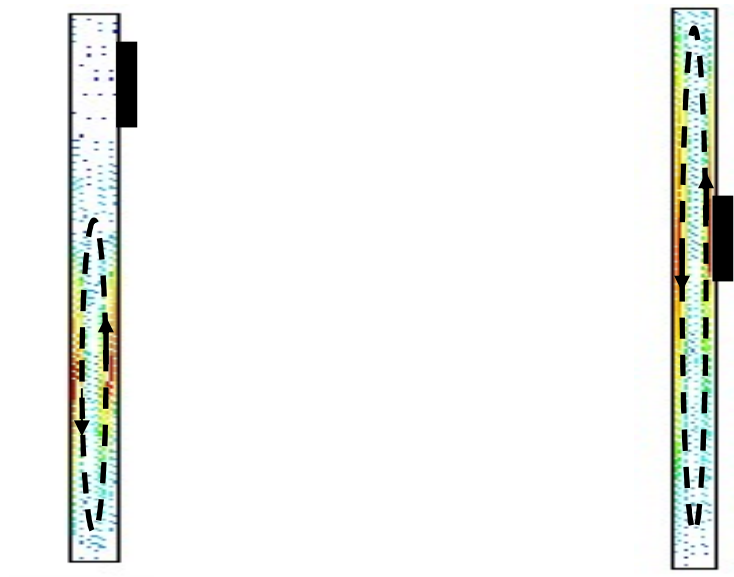


Figure A5.11: Vapour velocity inside the device for the two Peltier positions, upper and centred respectively

As you can see there is a greater circulation path in that configuration with the Peltier in the upper position. This means, a priori, a greater use of the exchange surface (absorption surface) and therefore a lower thermal resistance.

Thus it is concluded that the Peltier is placed on the top of the device.

A5.2.2-Real prototypes tests

- Prototype characteristics.

	Prototype						
	1	2	3	4	5	6	7
External dimensions	250x180x30 mm. $S = 0.042 \text{ m}^2$ $S' = 0.0016 \text{ m}^2$	208x173x22 mm. $S = 0.036 \text{ m}^2$ $S' = 0.0016 \text{ m}^2$	208x173x22 mm. $S = 0.036 \text{ m}^2$; $S' = 0.0016 \text{ m}^2$	250x180x30 mm. $S = 0.042 \text{ m}^2$; $S' = 0.0016 \text{ m}^2$	250x180x30 mm. $S = 0.042 \text{ m}^2$ $S' = 0.0016 \text{ m}^2$	250x180x30 mm. $S = 0.042 \text{ m}^2$ $S' = 0.0016 \text{ m}^2$	120x230x100 mm. $S = 0.036 \text{ m}^2$; $S' = 0.0025 \text{ m}^2$
Internal dimensions	16mm internal gap 10mm Wall thickness;	10mm internal gap 4mm Wall thickness	10mm internal gap 4mm Wall thickness	16mm internal gap 10mm Wall thickness	16mm internal gap 10mm Wall thickness	16mm internal gap 10mm Wall thickness	10mm internal gap 4mm Wall thickness
Material container	Aluminium	Methacrylate and Aluminium	Aluminium with straight fins in the condensing surface	Aluminium	Aluminium	Aluminium	Aluminium
Working liquid	Methanol 16gr, pressure 1atm at room temperature	Butane 16gr pressure 1atm at room temperature	Butane 16gr pressure 1atm at room temperature	Butane 16gr pressure 1atm at room temperature	Butane 16gr pressure 1atm at room temperature	Butane 16gr pressure 1atm at room temperature	Butane 16gr pressure 1atm at room temperature
Porous media	12 μm diameter copper powder; 35% porosity	Silicone fibre BC115	Silicone fibre BC115	Silicone fibre BC115	8 μm diameter copper powder	8 μm diameter copper powder plus internal grooves	Silica gel ALUGRAM Nano-Sil G 20x
Peltier Voltage	9.8 V	10V	10V	10V	10V	10V	10V

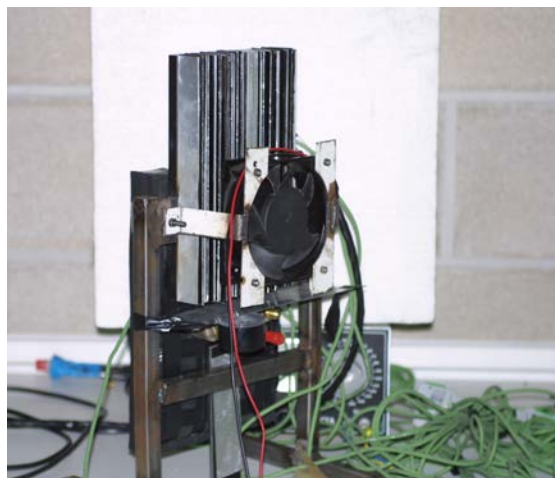


Figure A5.12: Picture of prototype 1

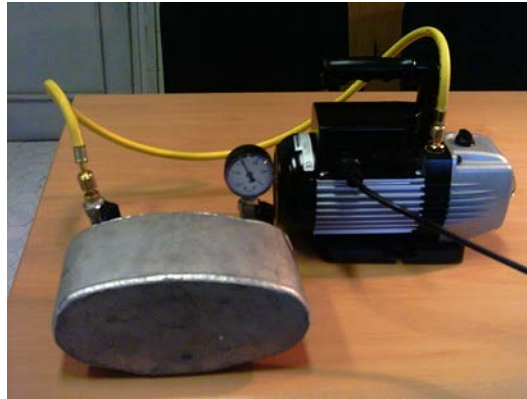


Figure A5.13: Picture of prototype 7

Experimental tests showed that the prototype thermal resistance was improved as new changes were introduced to the first prototype. This trend was so until the last change, prototype 7, when thermal resistance got larger than the previous prototype, figure A514.

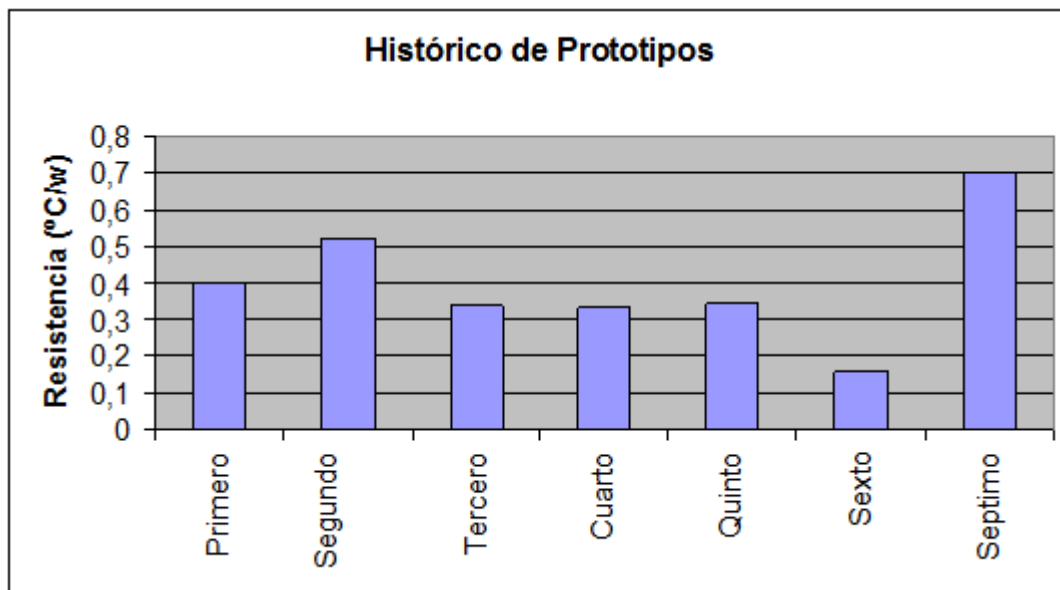


Figure A5.14: Thermal resistance of each prototype

Annex 6 – Short CV: Jesus Esarte

Personal data

Name: Jesús Esarte San Martín

Date of birthday: 24 April 1969

Address: Plz./ Rio Urederra Nº 6 - 1º IZQ, 31200, Estella (Navarra), Spain

Academic Background

-Industrial Engineer by University of Navarra

-PhD by the University of Basque Country UPV/EHU

Career

-Professor Assistant and researcher at the Public University of Navarra. Theoretical lectures of thermodynamics and heat transfer accompanied with laboratory works.

-Researcher at Cardiff University-Thermoelectric Laboratory. Research focused on the study of liquid cooling for thermoelectric generators.

-Currently, researcher at Fundación CETENA-CEMITEC. National-European Project management activity as well as research activities in advanced cooling technologies and heat storage.

Some articles and conferences

- J. Esarte, Gao Min, D.M. Rowe. “Modelling heat exchangers for thermoelectric generators”. *Journal of Power Sources* –Vol. 93/1-2; pages 72-76. Enero 2001
- J. Esarte, Manuel Dominguez. “Capillary Mechanism for the Heat Dissipation through a Thermoelectric Pellet”. *Applied Thermal Engineering* –Vol. 23, Issue 13. September 2003; pp: 1619-1627
- J. Esarte; J.M Blanco, C.Wolluschek, D.Prieto. “Heat dissipaters”, Chapter 20, -book: *Modules, Systems, and Applications in Thermoelectrics and/or the Materials, Preparation, and Characterization in Thermoelectrics Volume 1-2* –2012.
- J. M. Blanco, E. Armendáriz y J. Esarte. “Optimization of fin sinks through a parametric study of heat transfer”. *Journal of Advanced Thermal Science Research* 2014, 1, 3-8
- Xavier Jorda; Jesús Esarte; Xavier Perpiñà; Miquel Vellvehi; Gorka Argandoña; Maite Aresti. “Characterization of Phase Change Material Systems Using a Thermal Test Device”. *Microelectronics Journal*. 2015
- J. Esarte; Angela Bernardini; Jesus Maria Blanco; Ramón Sancibrian. “Optimizing the design for a two-phase cooling Loop Heat Pipe; Part A: numerical model, validation and application to a case study”. *Applied Thermal Engineering* 99 (2016); 892-904
- J. Esarte; J.M. Blanco, A. Bernardini, J.T. San-José. “Optimizing the design of a two-phase cooling system loop heat pipe: Wick manufacturing with the 3D selective laser

melting printing technique and prototype testing”. Applied Thermal Engineering 111 (2017) 407–419

- J Esarte; E.Armendáriz, C.Wolluschek. “Phase change heat dissipater of aluminium container”, THERMINIC2008 Conference, Roma 2008-Italy.
- E.Armendáriz, J.Esarte. “CFD thermal model, key aspects for a good modelling. Application to a specific package”. Microtherm-2009 Conference, Lodz – Poland, July 2009.
- A.Bernardini, J.M. Blanco, J.Esarte. “Optimization of fin heat sinks; Parametric heat transfer study on Matlab platform”. Congress of Numerical Methods in Engineering-CMNE 2011. Coimbra - Portugal June 2011.

Thesis: Development of a Loop Heat Pipe “LHP”
thermal superconductor device with
multicondensers

UNIVERSIDAD PAIS VASCO
Dpto. INGENIERÍA MINERA Y METALÚRGICA
Y CIENCIA DE LOS MATERIALES